Aerodynamic response of a two-dimensional vertical axis wind turbine to turbulence

Raunak Bagde

Technische Universiteit Delft

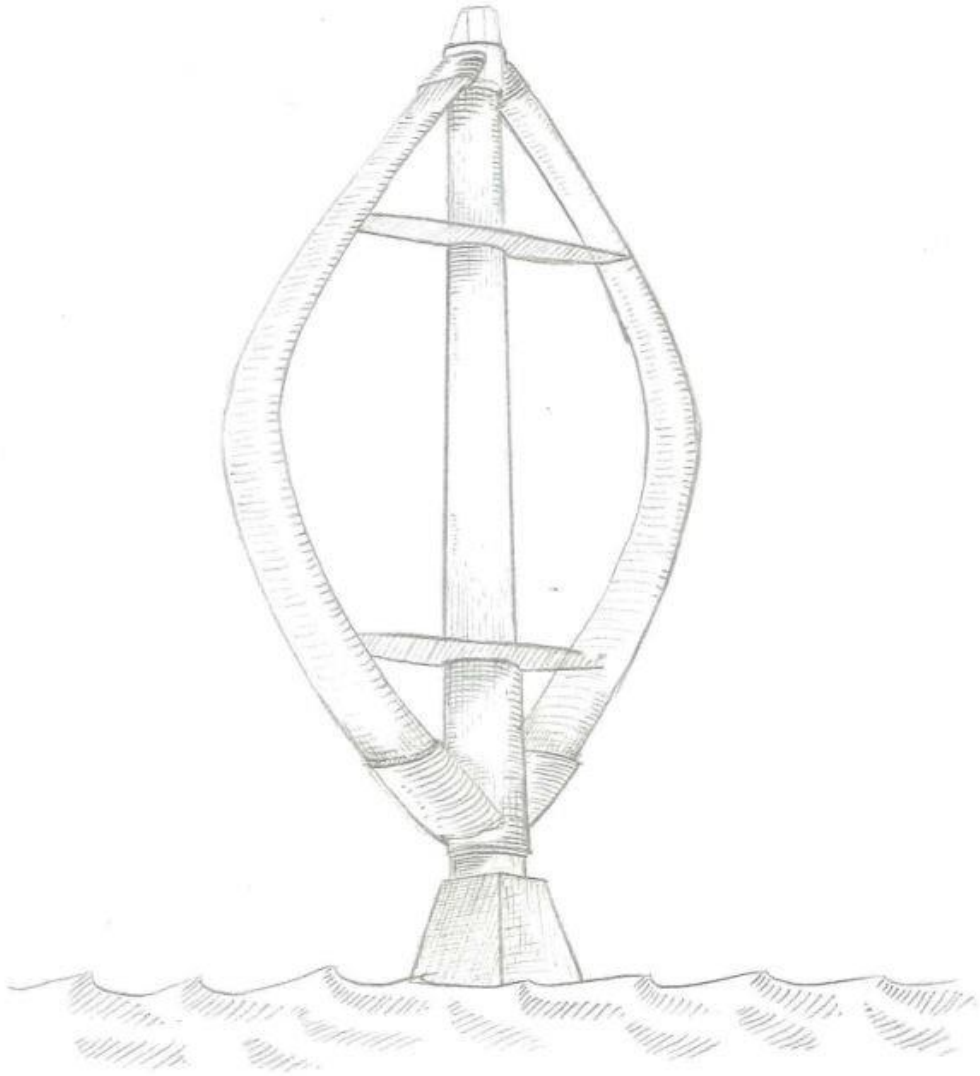

TU Delft Delft University of Technology

Challenge the future

AERODYNAMIC RESPONSE OF A TWO-DIMENSIONAL VERTICAL AXIS WIND TURBINE TO TURBULENCE

by

Raunak Bagde
4412699

in partial fulfillment of the requirements for the degree of

Master of Science
in Sustainable Energy Technology

at the Delft University of Technology,

Supervisor:	Dr. ir. C. S. Ferreira,	Wind Energy, TU Delft
Thesis committee:	Prof. Dr. G. J. W. van Bussel,	Wind Energy, TU Delft
	Dr. ir. C. S. Ferreira,	Wind Energy, TU Delft
	Dr. ir. W. A. A. M. Bierbooms,	Wind Energy, TU Delft
	Dr. ir. J. J. E. Teuwen,	Structural Integrity and Composites, TU Delft

TU Delft Delft University of Technology

ABSTRACT

The increasing global warming and climate change has boosted research on sustainable energy in the last few decades leading to a lot of research being carried out on wind energy. Wind turbines have played a major role in harvesting wind energy with Horizontal Axis Wind Turbines (HAWTs) being the dominant design. However, for urban and offshore applications, Vertical Axis Wind Turbines (VAWTs) have been under consideration for a while. VAWTs have some inherent advantages such as no need for a yawing mechanism, easy operation and maintenance, low noise emission, and better potential performance under skewed and unsteady wind conditions. But due to lack of research on VAWTs, they have not been commercialized on a scale which is equal to that of HAWTs. This study is one of such attempts for a better understanding of VAWTs. The primary aim of this study is to explore and analyse the behaviour of VAWTs under the influence of turbulent wind. This target has been achieved by analysing the loads on the turbine and their effect on its fatigue life under the influence of constant wind and turbulent wind. For this purpose, first one hour turbulent wind fields based on statistical models were generated using the turbulence simulator, 'TURBSIM' and two-dimensional turbulent wind fields were extracted from the generated wind fields. Next, the simulations of a two-dimensional vertical axis wind turbine using the generated turbulent wind fields were done in an aeroelastic code named 'Unsteady Two-Dimensional Vorticity Aerodynamics (U2DiVA) model'. These simulations were done between the cut-in (4 m/s) and cut-out (25 m/s) wind speeds of the turbine at intervals of 1 m/s. The results from these simulations were the streamwise force, cross-streamwise force and the moment about the quarter-chord points of the airfoils of the blades. A post-processing tool was then developed for the processing of these results. Using this tool and the results of the simulations, the equivalent tangential force, the equivalent radial force and the equivalent moment on the airfoils were calculated. All calculations were done for both types of wind. First the equivalent loads at each wind speed were calculated and then the total equivalent loads were calculated. The equivalent loads were calculated for various values of inverse slope (m) of the S-N curve of the material used to manufacture the blades of the turbine. The same procedure was repeated with constant wind. Finally,the changes in total equivalent loads under turbulent wind were calculated with respect to total equivalent loads under the constant wind. The variation in these changes with respect to the change in the value of m was then calculated. Additionally, the effect of phase angle (angle between the blades and the incoming windstream at the beginning of the simulation) on the equivalent loads was also calculated. The value of m used for this case was 10 as recommended in literature and the four phase angles chosen were 0^o, 45^o, 90^o and , 135^o.The equivalent loads at various wind speeds were calculated for the different values of m and various peaks were observed at various wind speeds. It was recommended that the peaks can be avoided using a suitable control scheme to control the rotational speed of the rotor. The changes in total equivalent loads under the influence of turbulent wind were found to be less than 0.2% which indicates that the effect of turbulence on the fatigue life of VAWTs is not so significant. The value of m at which the change was smallest was found to be around 3. Under phase effect, the variation of the radial force and the moment with wind speed seemed to follow Gaussian distribution at phase angles of 45^o, 90^o and 135^o. The total equivalent loads were found out for all the phase angles and the change in these loads were found out with respect to 0^o phase angle. These changes were quite high and indicate that the operation of a VAWT at phase with incoming wind can be detrimental for the fatigue life of the VAWT.

PREFACE

With increasing climate change and global warming, sustainable energy has been the focus of research in the last few decades. This has led to a lot of research being carried out on wind energy. Wind turbines have played a major role in harvesting wind energy with Horizontal Axis Wind Turbines (HAWTs) being the dominant design. However for urban and offshore applications, Vertical Axis Wind Turbines (VAWTs) have been under consideration for a while. But due to lack of research on VAWTs, they have not been commercialized on a scale which is equal to that of HAWTs. This study is one of such attempts for a better understanding of VAWTs. The primary aim of this study is to explore and analyse the behaviour of VAWTs under the influence of turbulent wind.

Chapter 1 gives a brief introduction to the history of wind turbines and the motivations behind this study and the research objectives. Both types of wind turbines are covered in the history of wind turbines. Next the main reason to carry out this study and objectives which had to be achieved to complete this study have been mentioned.

Chapter 2 covers the literature that had to be studied to know the methods of conducting research on them and the current status of VAWTs. Chapter 3 gives a detailed description of the tools and methods used in this study. It gives the details of the turbine model, IEC 61400-1 standard, site conditions for the turbine, the aeroelastic code, and the post processing tools used in this study.

Chapter 4 describes how the turbulence models were simulated and verified and how the simulations were carried out. In addition to this it also describes how the post processing of the results of simulations were done and how the analysis of the results was carried out. Chapter 5 describes the results of the simulations and their analysis. The variation in loads and the changes in them were discussed. The effect of phase angle on the loads has also been discussed.

Chapter 6 describes the conclusions and final results of this study while chapter 7 contains the suggestions which can be followed for further research and can help in a deeper understanding of VAWTs.

Raunak Bagde
Delft University of Technology
January, 12 2017

ACKNOWLEDGEMENTS

This thesis has been a great learning experience and it gives me immense pleasure to express my gratitude towards the people who have helped me in completing this thesis. The first person I would like to thank is my supervisor **Dr.ir. Carlos Simao Ferreira** whose consistent guidance and help has played a key role in the completion of this thesis. His guidance has helped me to overcome most of the difficulties I faced while working on this thesis. Special thanks to **Dr.ir. W.A.A.M. Bierbooms** , **Dr.ir. Michiel Zaaijer** and **Dr.ir. H.F. Veldkamp** for their valuable suggestions without which the completion of this thesis would have been really difficult.

I would also like to thank my colleagues at the TU Delft Wind Energy group who have helped with various aspects of this thesis. Special thanks to my colleague and dear friend **Jorge Tamayo 'Bhai'** for sketching the cover picture of this thesis and help on technical aspects.

I am grateful to my friends in Delft and abroad who have been more like a family throughout my tenure as a student at TU Delft. Finally, I would like to thank my parents and my late maternal grandmother for their constant support and guidance which has helped me throughout my life.

Raunak Bagde
Delft University of Technology
January, 12 2017

CONTENTS

LIST OF FIGURES

List of Tables

1

INTRODUCTION, MOTIVATION AND OBJECTIVES

1.1. INTRODUCTION

The significant increase in global warming in the last century has significantly damaged our environment. According to Copenhagen Accord, in order to prevent the increase in concentration of Greenhouse Gases (GHGs) to the extent that they may lead to dangerous anthropogenic interference with the climate system, we need to restrict the increase in global temperature to 2 °C by the year 2100 (UNFCCC, 2009). To stay within the target of 2 °C, the estimated amount of Carbon Dioxide (CO_2) that can be emitted by the year 2100 is 2900 Gt. About 60% of this budget of (CO_2) has already been spent. With considerable reserves of fossil fuels which can emit the amount of CO_2 which is three times the remaining budget, it is quite difficult for the world to attend this target. The additional potential of unconventional fossil fuels and low-quality resources would further enhance the problem (Pulles, 2015). Hence, there is an urgent need to promote sustainable energy sources. Wind energy being one of the major sustainable energy sources can play a huge role in meeting this target.

Wind energy has been primarily harnessed either using windmills or wind turbines since ancient times. Wind turbines can be broadly classified into two categories based on the alignment of their rotation axis with the incoming wind. These categories are: Horizontal Axis Wind Turbines (HAWTs) and Vertical Axis Wind Turbines (VAWTs). The HAWTs have axis of rotation of the rotor parallel to the wind flow direction while in the VAWTs the axis of rotation of the rotor is perpendicular to the direction of flow of wind. Windmills were the first machines that were used to harness wind power. According to Burton *et al.* (2001), windmills are believed to exist for at least 3000 years. The primary purpose of wind power in the ancient times was to either grind grains or pump water. It was also used to power sailing ships (Burton *et al.*, 2001). The first known reference to windmills was made by Hero of Alexandria who was believed to have lived in either 1^{st} century B.C. or in 1^{st} century A.D. The system defined by him is that of an organ which received air by the means of a windmill. The existence of such a windmill is debated. In 9^{th} century wind mills were used in the region of Seistan which is now in the Eastern Iran (Figure 1.1). This is the next known reference to the wind mills. These wind mills are still in use in the present times (Manwell *et al.*, 2009).

Figure 1.1: Seistan windmills (Manwell *et al.*, 2009)

Windmills are believed to have arrived in northern Europe (England) in either 10^{th} or 11^{th} century but their first recorded appearance dates back to 12^{th} century. It is believed that this concept was introduced in Europe by Vikings who travelled regularly from northern Europe to Middle-East. The northern European windmills had horizontal axes and used lift-force as the driving force. They had four blades and were primarily used for water pumping, grinding grain, sawing wood, and powering tools. The direction of these windmills could be changed to face the direction of wind since they were built on posts. An example of such a wind mill can be seen in figure 1.2 (Manwell *et al.*, 2009).

Figure 1.2: A north European wind mill also known as post mill (Manwell *et al.*, 2009)

With the advent of Industrial Revolution, the European windmills started to recede since wind power was non-dispatchable and non-transportable. By the time they demised, windmills had achieved a lot of sophistication. The blades had acquired a shape which somewhat resembled an airfoil and had some twist as well and in some machines power output could be achieved by an automatic control system. During this period another variant of windmills came into existence which was widely used in the USA. This variant had a large number of blades and its regulation was done by a system which was quite simple and effective and allowed the turbines to remain unattended for long running periods. An example of this type of windmill can be seen in figure 1.3. Its primary use was to pump the water to the ranches used for the cattle and supply the water for the railroad systems (Manwell *et al.*, 2009).

Figure 1.3: An American windmill designed for pumping water (Manwell *et al.*, 2009)

In the modern times, wind energy is harnessed using wind turbines which are primarily used to generate electricity. The second half of the last century has seen some rapid development of the wind turbines. Currently, the HAWT is the dominant design in the wind turbine market due to its high reliability and lower cost of energy when compared to other wind turbine designs. When the total generating capacity of the turbines is considered, then it can be seen that the turbines which contribute to the majority of the capacity are quite large with the size ranging between 1.5-5 MW. These turbines are generally used in large utility grids and were used earlier in the USA and Europe and are now being manufactured and used in China and India as well (Manwell *et al.*, 2009). The first wind turbine was developed by Charles F. Brush in 1888 in Ohio (USA) which could generate a maximum power of 12 kW (Burton *et al.*, 2001, Zaaijer, 2014). During the same period some significant work in this field was done by Poul la Cour in Denmark as well. He developed around 100 turbines that generated electricity in the range of 20-35 kW between the years 1891 and 1918 (Manwell *et al.*, 2009, Burton *et al.*, 2001). After World War II, a 200kW turbine named Gedser turbine (figure 1.4) was constructed by Johannes Juul in Southeastern Denmark. This turbine had three blades and used aerodynamic stall for power control. It also used induction generator as opposed to the synchronous generator which were the conventional generators at that point of time. While stall is a simple method to control power, the induction generators are much easier to connect to the grid. These two concepts led the Danish presence to be strong in the field of wind energy in the 1980s.

Figure 1.4: Gedser wind turbine (TelnosNet web development, 2015)

Another pioneer in this field during the 1950s was Ulrich Hütter whose work was mainly focused on applying the modern aerodynamic principles to wind turbine design (Manwell *et al.*, 2009). In 1941, a large turbine

with a power rating of 1.25 MW was developed in US. This machine was known as Smith-Putnam machine. It had a steel rotor of 53m diameter and a full-span pitch control along with flapping blades to reduce the loads. This turbine failed catastrophically in 1945 but remained the largest wind turbine for the next 40 years (Burton *et al.*, 2001).

The re-emergence of wind energy took place in the late 1960s when people started becoming aware of the environmental consequences of uncontrolled industrial development and use of fossil fuels. The main sources for this awareness were the books *Silent Spring* written by R. Carson in 1962 and *The Limits to Growth* written by D.H. Meadows, D.L. Meadows, J. Randers and W.W. Beherens III in 1972. During the same time period, the dangers of nuclear energy started becoming more known to the people leading to starting of a movement for advocating the cleaner sources of energy (Manwell *et al.*, 2009). Even with this awareness in the late 1960s in US and Europe and the technical advances in wind energy in the first half of 20^{th} century, wind energy did not develop significantly until the oil prices rose significantly in 1973 which lead to people demanding for alternate sources of energy. The main developments took place in US and Denmark during this time. In US, the government provided incentives and made some changes in the utility regulatory structure. The US federal government in 1978 required utilities to allow wind turbines to be connected with the grid and pay the cost that was saved by the producer for each kWh of electricity that was generated and fed into the grid by the turbine. The best incentives were provided by the state of California and it also had regions with good wind regimes leading to the installation of a large number of wind turbines in the state. Many wind farms were installed in California during this time. The Danish manufacturers also had a major presence in the wind energy market of California and their production quality was much better than the turbines manufactured in US. This surge in the wind energy production collapsed in the early 1980s. The main reason for the collapse was the absence of a certifying measure that would certify that the turbines would perform the same way as claimed by the manufacturer. An investment tax credit was provided by the federal government to promote the development and establishment of wind farms but it is not deemed the best for such purposes. Hence these credits were withdrawn by the government in early 1908s. After this collapse, a majority of the US manufacturers went out of business while the Danish manufacturers survived by either restructuring or merging. During the 1990s the main developments took place in Europe, mostly in Denmark and Germany (Manwell *et al.*, 2009, Burton *et al.*, 2001). These developments are still taking place throughout Europe and as of 2015, the installed wind energy capacity in Europe stands at 147.772 GW (EWEA, 2016).

While HAWTs have been dominant in the recent past of the wind energy, the VAWTs have seen some significant development in the 20^{th} century as well. Due to some inherent advantages, the VAWTs are more suitable for severe wind climates. Some of these advantages are (Sutherland *et al.*, 2012, Wekesa *et al.*, 2015):

1. No requirement of a yawing mechanism since the turbine is designed in such a way that blades move perpendicularly to the direction of wind.

2. Easy to maintain since the gearbox and the generator are located at the base of the turbine.

3. Low noise emission since the operational speeds of the turbines are pretty low.

4. Potential for better performance under skewed and unsteady wind conditions.

5. For offshore conditions, the generator and the gearbox can be placed at or below the water level. This leads to the turbine being more stable and reduces the capital costs without any reduction in the performance of the turbine.

6. Under skewed conditions, the VAWTs generate more power than non-skewed conditions. This is true only for a certain range of skew angles. This is due to the fact that the downwind part of the turbine is exposed to both incoming wind and the wake of the upwind part of the turbine (Ferreira *et al.*, 2006).

Even with the such advantages the VAWTs are not as commercially dominant as the HAWTs since the quantity of available research on the aerodynamics of VAWTs is little (Wekesa *et al.*, 2015). Additionally, it hasn't been proved yet that the HAWTs have a better aerodynamic efficiency than VAWTs (Durrani *et al.*, 2011).

VAWTs can further be classified into two main categories namely, Lift driven VAWTs and Drag driven VAWTs.The drag driven VAWTs use momentum transfer for power generation while the lift driven VAWTs use aerodynamic forces for power generation. Furthermore, the dominant configurations for these two types of VAWTs are the Savonius configuration for Drag driven VAWTs and the Darriues configuration for Lift driven VAWTs. Some of the other configurations along with the Darrieus configuration for lift driven VAWTs can be seen in figure 1.5.

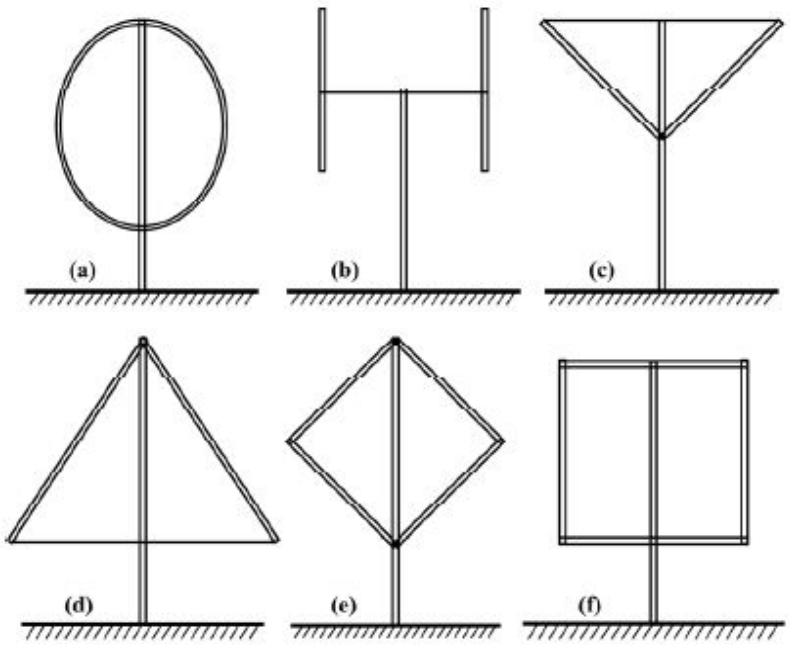

Figure 1.5: Different types of lift driven VAWTs: (a) Darrieus (b) H (c) V (d) Delta (e) Diamond (f) Giromill (Sutherland *et al.*, 2012)

The H-rotor was developed into several different configurations such as articulating, tilted and helical rotors. These rotors had a high specific cost of energy (COE) and thus their production was stopped (Tjiu *et al.*, 2015a).

The Savonius rotor (figure 1.6) was proposed by Sigurd Johannes Savonius in 1922. Even though the concept for this rotor was proposed in 1922, it was not applied for many years. The rotor of this turbine has a 'bucket' design. Apart from the advantages mentioned earlier, the other advantages of this design are high starting torque, compact size and simple and cheap construction. These advantages make the Savonius turbines suitable for residential applications. The main disadvantages of this turbine are its relatively low efficiency (maximum practical efficiency is 60 %) and low rotational velocity (Kacprzak *et al.*, 2013).

Figure 1.6: A savonius wind turbine (Netzero guide, 2013)

Even though the Savonius turbine is said to be drag driven, it was observed by Modi and Fernando (1989)

that at smaller small angle of attacks, the rotor behaves like a slender body which leads to the lift force contributing to the power.

The Darrieus rotor (figure 1.7) was designed and patented by a French Engineer named George Marie Jean Darrieus in 1925 in France (Sutherland *et al.*, 2012). This configuration had two curved blades and the whole rotor was designed into the shape of a troposkien (also known as 'eggbeater' shape). A more detailed schematic of this rotor can be seen in figure 1.8.

Figure 1.7: A Darrieus wind turbine (Makcan Resources Corporation, 2015)

Though the Darrieus rotor was invented in 1925, it was not put in use until 1968, when it was reinvented by South and Rangi of the National Research Council of Canada. After this a lot of research on the Darrieus VAWT was carried out by many researchers leading to the development of various dynamic analysis models such as blade momentum, vortex and finite-difference models. The troposkien shape of the rotor was initially praised since it could endure high centrifugal forces. Due to this reason the blades of the rotor could be made slender and light with low cost. However the performance of the rotor depended on the blade curvature (Tjiu *et al.*, 2015a).

Although Darrieus VAWTs have some major advantages over the HAWTs, they have some drawbacks as well. Some of these drawbacks are (Sutherland *et al.*, 2012, Tjiu *et al.*, 2015a):

1. The blades of a full-Darrieus VAWT are twice as long as that of a HAWT with equivalent rotor swept area. This increases its capital costs. This problem can be solved by using constant chord blades for the turbine with a small reduction in the aerodynamic performance of the turbine.

2. The blades of a Darrieus VAWT are lighter which leads to large flexures. This problem is solved by reinforcing the blades using struts which introduces an aerodynamic drag at the blade to strut joints which might lead to a significant reduction in the performance of the rotor.

3. To sustain the torque produced by the blades which is cyclic in nature and the loads due to the guy wires, the column of the tower should be large leading to more turbulent wake of the column. This would interfere with the blades when they are in the downwind half of the rotor leading to unnecessary vibrations on the blades and support structures.

4. The rotor of a Darrieus VAWT may or may not be self-starting which depends on the wind conditions. In order to ensure that the VAWT starts when desired, a starting system must be installed in the turbine.

This system has a simple build connecting the motor to the generator to rotate the rotor till the turbine reaches the desired rotational speed. This simple system requires the gearbox to be bidirectional increasing the capital costs of the turbine.

5. The torque on a VAWT due to its blades varies throughout the rotation since it is positive when a blade crosses the wind, while it is almost zero when the blade is parallel to wind leading to two pulses in every rotation. In a two bladed Darrieus VAWT, the torque pulses due to both the blades align which leads to sinusoidal torque variation with a non-zero mean. This problem can solved by adding compliance (in torque) to the drive train.

6. Due to the blades own weight, the troposkien shape tends to deform. This due to the presence of a static force applied by the gravity. This problem is present with larger rotors where the blades are longer in length. When the rotor starts rotating, this static force becomes dynamic and oscillates in accordance with centrifugal force depending on the rotor speed.

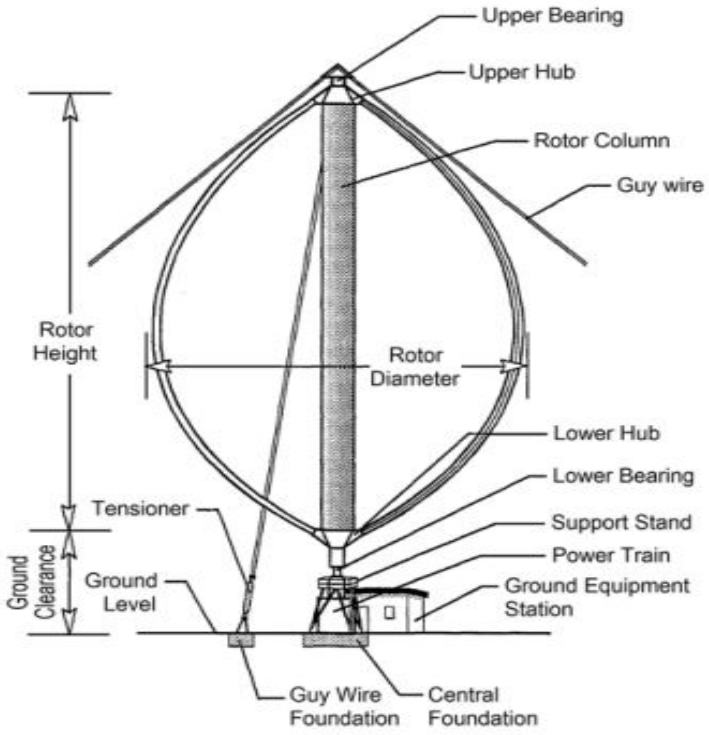

Figure 1.8: A schematic depicting various components of the testbed (Tjiu *et al.*, 2015a)

7. In order to stabilize the top of the rotor, the VAWTs use guy cables as it is a cost effective method for this purpose. This requires the bearing at the bottom of the turbine to be designed for the additional loads on the turbine top due to the guy wires along with a thrust bearing at the top of the rotor so that the rotor can rotate beneath the cables. Additionally, this can be detrimental for a farming country since the guy cables and their anchors give the turbine a large footprint.

8. The variable pitch blades and aerodynamic brakes are difficult to implement on the VAWTs when the conventional airplane type airfoils are used. This might lead to the turbine becoming uncontrollable leading to self destruction of the turbine. This can be avoided by using the airfoils optimized for VAWTs which shed loads at high speeds and also limit the power output at high wind speeds by lowering the rotational speed of the rotor.

9. To get the equatorial section (the section with the maximum diameter) on higher heights, a higher height-to-diameter ratio is required. When the rotor is situated on the ground and the terrain roughness is high, the wind velocity along the rotor height would be uneven leading to higher lift forces

produced at higher heights when compared to lower heights. This leads to instability across the rotor leading to a shorter fatigue life.

While the VAWTs do have some major disadvantages, most of them can be reduced with some simple solutions and small compromises in the performance of the rotor.

When the research into the Darrieus VAWTs gained momentum, a number of problems started to occur starting with problems in drivetrain, control systems and brakes. During this period the largest rotor was developed by Sandia National Laboratories (SNL) called 'test bed' which had a rotor diameter of 34m and and was operational in 1988. It was also the last rotor in this research phase (Tjiu *et al.*, 2015a).

Very little research has been carried out to study the behaviour of VAWTs under the influence of unsteady winds. Some effects of unsteady winds were studied and the optimization of the power output of the VAWTs was carried out by McIntosh *et al.* (2007, 2008). The major portion of research that has been carried out on VAWTs has was carried out under steady wind conditions since there are available detailed and well established analyses for blade loading and rotor performance under these conditions (Danao *et al.*, 2013). While the research on VAWTs came to an effective halt around mid 1990s (Sutherland *et al.*, 2012), the interest in VAWTs has recently reemerged due to the emerging interest in wind energy in built environment (Edwards *et al.*, 2012).

1.2. MOTIVATION BEHIND THIS THESIS

Vertical axis wind machines have been in existence for a long period of time but since the emergence of wind turbines, the VAWTs have not been commercialized successfully despite some great advantages over the Horizontal Axis Wind Turbines (HAWTs). Turbulence has a huge effect over the life of wind turbines. Since the behaviour of VAWTs under the effect of turbulence has not been studied much, not much information about the effect of turbulence on the life of wind turbines is available. This information is very crucial for the development of VAWTs and will also help in understanding the functioning of VAWTs in realtime operation. Currently, there are existing standards for the design of HAWTs while there are no specific standards for VAWTs. Hence for the successful commercialization of VAWTs, there is an urgent need of a standard for VAWTs. One of the ways in which this can be done is to use the existing standards to test the VAWTs and on the basis of results of these tests, the existing standards can be tailored for VAWTs. This study is an attempt to use the turbulence models specified in the existing standard 'IEC 61400-1' in order to know what would be the effect of these wind models on the airfoils of a two-dimensional VAWT for offshore applications.

1.3. RESEARCH OBJECTIVES

The main research objective of this study is to know the effects of turbulence on VAWTs. This objective can be achieved as follows:

1. To develop the tools to simulate the Normal Turbulence Model (NTM) wind specified in the standard 'IEC 61400-1' for a two-dimensional VAWT and carry out these simulations.

2. To understand the response of a VAWT to NTM wind by analysing the forces and moments on the airfoils.

3. To develop the tools required to analyse the forces and moments on the airfoils and process them for further calculations.

4. To determine the change in equivalent loads on the VAWT airfoils under the influence of turbulence models specified in the standard.

5. To determine the sensitivity of the change in equivalent loads on the airfoils with respect to the inverse slope of the material of the airfoil.

6. To determine the effect of phase angle on the loads on the turbine.

2

LITERATURE REVIEW

A lot of research on VAWTs has already been carried out by researchers across the globe. Commonly used basic research methods in this field are Computational Aerodynamics, Computational Fluid Dynamics (CFD) and experimental methods. The main focus of the current research on VAWTs is on aerodynamics of the VAWTs (Jin *et al.*, 2015).

2.1. NUMERICAL METHODS FOR VAWTS

Numerical methods have played a key role in the development and analysis of VAWTs. The two major numerical methods that are used for this purpose are the Computational Aerodynamics and Computational Fluid Dynamics.

2.1.1. COMPUTATIONAL AERODYNAMICS FOR VAWTS

Commonly used computational aerodynamics models are (as cited in Jin *et al.* (2015) and Islam *et al.* (2008)):

1. Momentum model: This model assumes a streamwise flow around the rotor and the flow velocities are computed by equating the aerodynamic forces along the stream with the rate of change of momentum of the air. The value of force obtained from this model is equal to the average pressure difference across the rotor. Bernoulli's equation is used for the calculations in each streamtube. This model is further classified into three types. These models become invalid for large tip-speed ratios and higher rotor solidities since the momentum equations are inadequate for these cases. The three types of this model are:

    1.1. Single streamtube model: This model was proposed by R. J . Templin in 1974 and is the most simple model amongst all the available models for the calculation of performance characteristics of Darrieus-type VAWTs (Figure 2.1a). This model has the entire rotor enclosed in a single streamtube and the actuator disc is considered as the surface of the imaginary body which is revolving around the same axis as that of the turbine. Constant velocity is also assumed throughout the upstream and downstream side of the volume swept by the rotor. The velocity through the rotor is constant as well which is the average of the upstream and downstream velocities across the volume. The streamwise drag is equated with the change in axial momentum in order to find the value of this velocity.

    1.2. Multiple streamtube model: To overcome the drawbacks of the single streamtube model, R. E. Wilson and P. B. S. Lissaman introduced the multiple streamtube model in 1974. In this model the volume swept by the rotor was divided into a series of multiple adjacent, aerodynamically independent parallel streamtubes as shown in figure 2.1b. The blade element and momentum theories were applied for each of the streamtubes. Only lift force could be calculated using this model. This was due to the reason that the flow was assumed to be incompressible and inviscid for the calculation of induced velocity through the streamtube. The coefficient of lift is given by the expression for the coefficient of lift for a flat plate. An improved multiple streamtube model was proposed by J. H. Strickland in 1976 which included computation of drag force as well. This model could

be used only for fast running lightly loaded wind turbines. Both Wilson's and Strickland's models could include the effects of atmospheric wind shear. Strickland's model took more computation time when compared to Wilson's model due to additional calculations for drag forces.

Another multiple streamtube model was proposed by R. J. Muraca, M. V. Stephens, and J. R. Dagenhart in 1975 which considered the effects of airfoil geometry, support structure, blade aspect ratio, blade solidity and blade interference. In 1977 D. J. Sharpe presented another multiple streamtube model which incorporated the effects of Reynolds number in the calculations. An improved version of this model was presented by S. Read and D. J. Sharpe in 1980 which did not use the concept of parallel streamtubes and included the expansion of streamtube. Overall, all the versions of the multiple streamtube models predicted lower values of power when compared to the experimental results.

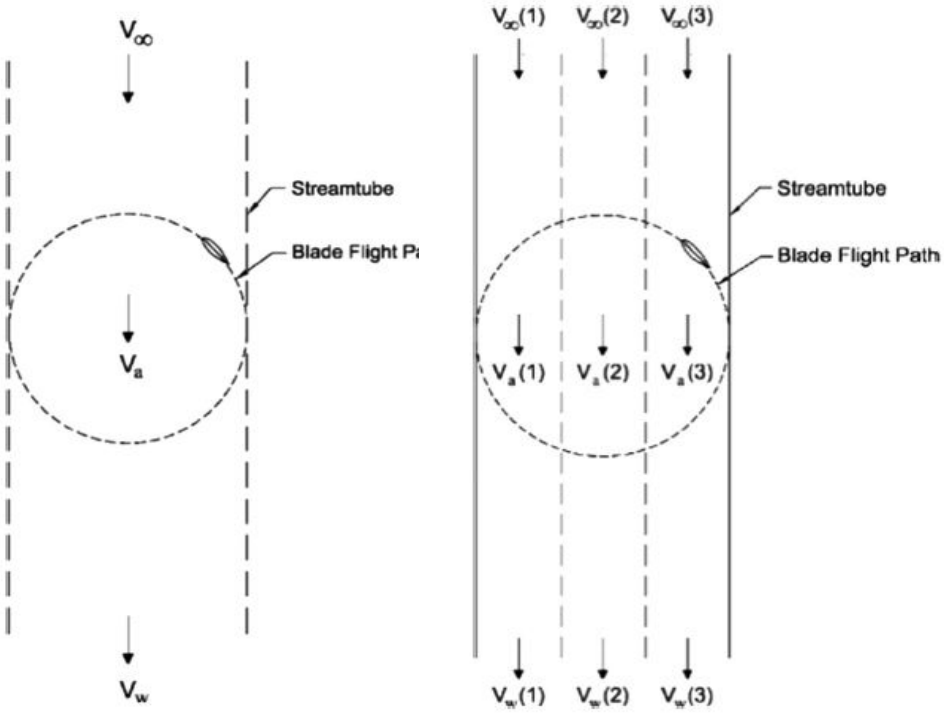

(a) Single streamtube model (b) Multiple streamtube model

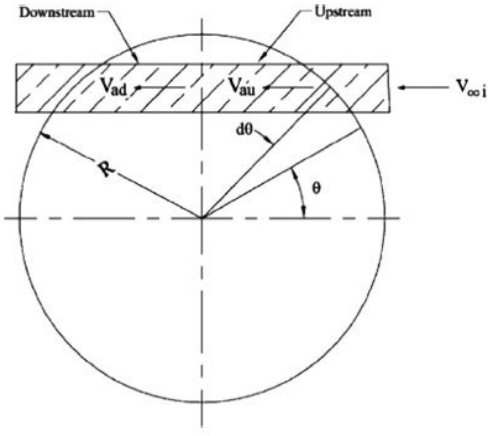

(c) Double-multiple streamtube model

Figure 2.1: Types of momentum models (Jin *et al.*, 2015, Islam *et al.*, 2008)

1.3. Double-mutiple streamtube model: In 1981 I. Paraschivoiu introduced this model based on the

multiple streamtube model for VAWTs. This model uses the concept of two actuator discs in tandem and the volume swept by the rotor is divided into upstream and downstream halves. These halves are further divided into upper and lower streamtubes (Figure 2.1c). The concept of two actuator discs in tandem was originally proposed by E.E. Lapin in 1975. Using this concept the induced velocities are obtained in all the layers of upstream and downstream halves. The vertical variation of velocity is considered in this model while the horizontal variation is not considered for this case. The main advantage of this model is that it gives better correlation between the calculation and experimental results. This correlation is quite good for the local aerodynamic blade forces with the multiple streamtube models. Additionally this model has significantly improved the simulation of dynamic stall effect. For a rotor of high solidity and tip-speed ratios, the model is not very precise and needs further improvement.

2. Vortex model: In vortex models, the calculation of the velocity field is done about the turbine using the influence of vorticity in the wake of the blades. These models are potential flow models. Bound or lifting-line vortices are used to represent the turbine blades. The strength of these vortices are determined using airfoil datasets and calculated flow velocity and angle of attack. The root and the tip vortices are shred by the blade (Figure 2.2). Due to Helmholtz's theorem, the strength of the bound vortex and each of the trailing vortices have equal strengths. The strengths of the shed vortices change on several occasions. When the strengths of the shed vortices change, a spanwise vortex is shed and its strength is equal to the change in the strength of the bound vortex. This change is dictated by Kelvin's theorem. For a given point in the flow field, the fluid velocity at that point is given by the sum of undisturbed wind stream velocity and the velocity induced by each of the vortex filaments in the flow field. At a given point in the flow field, the velocity induced by a vortex filament can be calculated using Biot-Savart law which relates the induced velocity to the vortex filament strength. For the closure of the model, a relationship between the bound vortex strength and the velocity induced at a blade segment is required. The Kutta-Jukowski law gives the relation between the strength of the bound vortex and the lift per unit span on a blade segment. The lift force is also defined using the coefficient of lift. Equating the expressions for lift force from the Kutta-Jukowski Law and the coefficient of lift relation, the relationship between the bound vortex strength and the velocity induced at a blade segment can be found out. The determination of the induced velocity distribution makes it easier to find the performance characteristics of a VAWT.

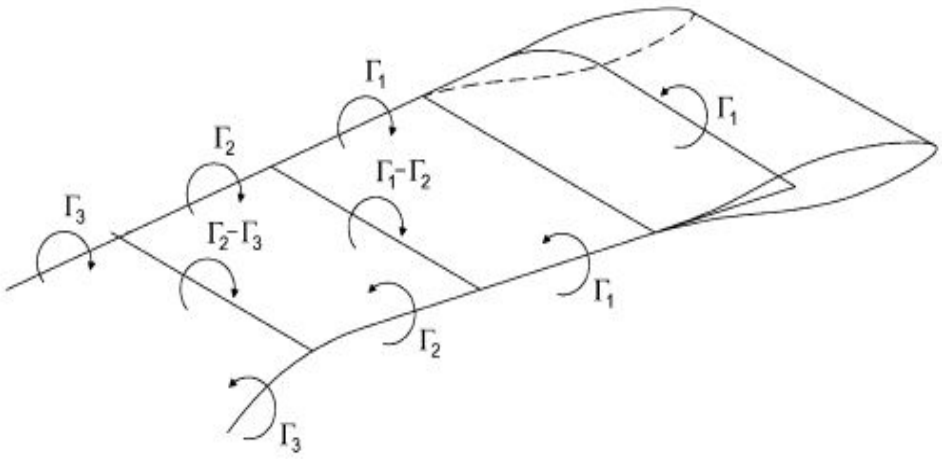

Figure 2.2: Vortex model (Islam *et al.*, 2008)

The first idea of a vortex model was introduced by H. C. Larsen in 1975. This vortex system was defined for a single blade element of a VAWT. The angle of attack in his model was assumed to be small and hence the stall effect was neglected. Another model was proposed by Fanucci and Walter (1976), which was a two-dimensional model and could be applied on a straight-bladed VAWT. In 1976, O.A. Holme adopted the vortex model for the simulation of a VAWT operating at a high speed but it could be ap-

plied only to the lightly loaded rotor. Strickland *et al.* (1979) proposed a three dimensional quasi-steady vortex model which considered the aerodynamic stall as well. Subsequently they adopted the dynamic effect in the model making a three dimensional dynamic vortex model. The main advantage of this model is high precision in the prediction. The major disadvantages of this model are high computation time and great dependency of the computational accuracy on the potential flow model used for computation.

3. Cascade model: This model is commonly used for turbomachinaries and was first proposed by H. Hirsch and A. C. Mandal in 1987 for analysis of VAWTs. The airfoils of the blades are assumed to be in a plane surface and this arrangement is termed as a cascade (Figure 2.3). The space between the blades in the plane is equal to the circumference of the turbine divided by the number of blades in the turbine. The wake velocity and the free stream velocity are related to each other by Bernoulli's equation while the induced velocity and the wake velocity are related to each other through a particular semiempirical expression. The aerodynamic characteristics of each element of the blade are calculated separately for the upwind and downwind halves of the rotor in this model. The local Reynolds number and the local angle of attack are considered for these calculations. The local relative flow velocity and the angle of attack are determined and subsequently the VAWT is developed into a cascade configuration as shown in figure 2.3. The plane of the cascade is considered normal to the plane of the turbine axis. One of the blades is considered to be the reference blade and the flow conditions on the remaining blades are assumed to be equal to that of the reference blades. With a small angular step, this process is continued for a whole revolution of the reference blade.

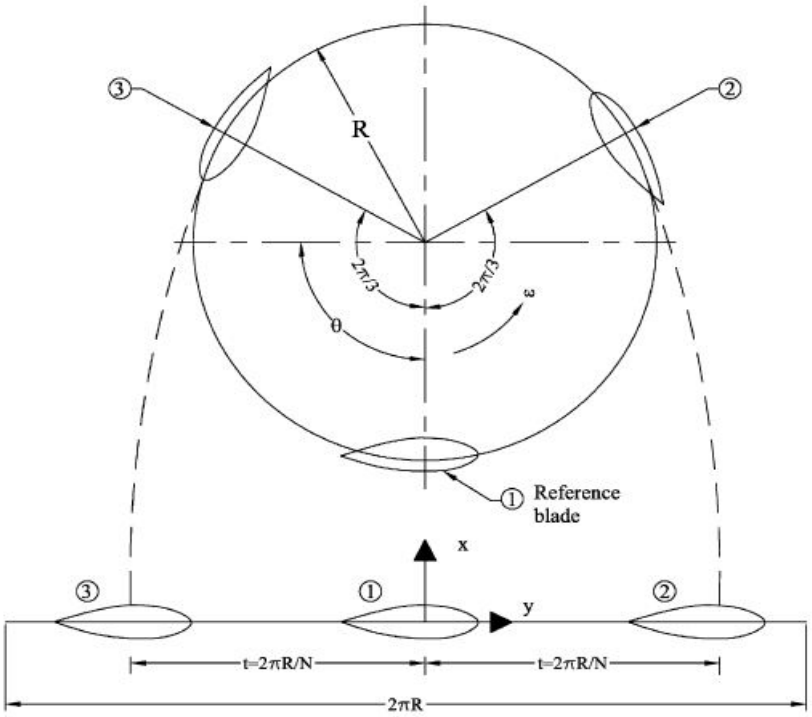

Figure 2.3: Cascade model (Islam *et al.*, 2008)

The main advantage of the cascade model is that it can predict the overall values of both low and high solidity turbines quite well. Additionally, it does have any convergence problems even at high tip-speed ratios and solidities. When comapred to the conventional momentum models, the instantaneous blade forces obtained from this model show improved correlation. The effects of local Reynolds number variation at different azimuth angles, finite aspect ratios, zero-lift-drag coefficients and the flow curvature effect were also incorporated in this theory during the calculation process. In 1994, J.D. Burton and A.C. Mandal included the effects of the dynamic stall and flow curvature with blade pitching in order to improve the analytical capability of this model. After these modifications were made, the values of

the wake velocities calculated became comparable to the values obtained from the complex dynamic vortex model.

2.1.2. COMPUTATIONAL FLUID DYNAMICS FOR VAWTS

The next basic research method that has been used to study the behaviour of VAWT is the Computational Fluid Dynamics (CFD) method. This method has been attracting more attention in the recent years as the most promising method in the recent years. CFD requires no additional complex control or testing system at a low cost for a systematic analysis. Additionally, fluid fields can be simulated in detail with this method. Several numerical solutions have been developed from this method which differ from each other only on the basis of discretization of the governing equations. On the basis of discrete principle, general classification of CFD can be done into three branches namely, Finite Difference Method (FDM), Finite Element Method (FEM) and Finite Volume Method (FVM) (Jin *et al.*, 2015).

1. Finite Difference Method (FDM): This method is the earliest method in terms of application and is the most classical method. The continuous domain is substituted with finite mesh nodes and this is done by dividing the solution domain into difference meshes. FDM are numerical methods in which finite difference equations are used to approximate derivatives in order to find approximate solutions for the differential equations. The differential problems are directly turned into algebraic problems for obtaining an approximate solution in this method. Since this method was developed quite early when compared to other methods, this method is relatively mature. This method requires definition of complex boundary conditions and therefore is not as convenient as Finite Element Method (FEM) or Finite Volume Method (FVM). T. Kawamura and Y. Sato (Kawamura and Sato, 2002) used FDM to study flow around a wind rotor.

2. Finite Element Method (FEM): This method was first used in 1980s to find the approximate solutions to boundary value problems for differential equations. Due to more required computation time when compared to FDM and FVM, this method is not used widely. It was used in COSMOS by U. K. Saha, M. J. Rajkumar, and D. Maity in 2005 and in ADINA by O. B. Yaakob, K. B. Tawi, and D. T. S. Sunanto in 2010 for finding the solutions of fluid flow problems around a VAWT.

3. Finite Volume Method (FVM): FVM is a method used to represent and evaluate partial differential equations in the form of algebraic equations. Around each point on a mesh is a surrounding small volume which is referred as finite volume. Using divergence theorem, volume integrals in a partial differential equation which contains a divergence term are converted to surface integrals in this method. It is most used CFD method presently and requires lesser computation when compared to other CFD methods.

Proper selection of turbulence models is required for VAWTs since they operate in a turbulent environment. For aerodynamic computations, incompressible Navier-Stokes equations can be used since the flow velocity is less than 0.3 times the Mach number. Due to vortex separation and flow unsteadiness, static or dynamic stall may occur during the rotation of a VAWT and hence an unsteady fluid solver is required to solve these flow problems. The results of the computation are largely directed by the choice of turbulence models. Reynolds Average Navier-Stokes (RANS) turbulence models are applied widely due to their reasonable precision and efficiency. Menter's Shear Stress Transport (SST) model is a type of RANS model which has a combination of k-ω and k-ε models based on zonal blending functions. In order to simulate great adverse pressure gradients and air flow separation, SST model is considered as the most promising method. Large Eddy Simulation (LES) models are another type of turbulence models which when compared to RANS models require more computing resource. The reason for this is that larger boundary-independent eddies can be solved directly by using governing equations and sub-grid models are used to consider smaller and more homogeneous eddies. In general, LES models can be used for a wider range of turbulent flows when compared to RANS models. Smagorinsky-Lilly model is the best known LES model since it does not have the limitations of the original model (Jin *et al.*, 2015). It has been used by Cummings *et al.* (2003), Gao *et al.* (2008) and Islam *et al.* (2010) to prove that LES models are more effective in simulating unsteady separated flows.

CFD models have been applied on the Darrieus VAWTs in the form of 2D, 2.5D and 3D models (Jin *et al.*, 2015).

1. 2D CFD models: The 2D CFD models highlighted the presence of a complex vortices system in the VAWTs. Additionally, their ability to predict the effect of dynamic stall on the flow field was better than

that of the BEM models. 2D CFD models have also been used to investigate power efficiency improvement. Mohamed (2014) used Unsteady Reynolds Averaged Navier Stokes (URANS) equations to analyze the aerodynamic noise as well as the impact of blade shape, tip-speed ratio, solidity and distance on the aerodynamic noise. Another 2D simulation of dynamic stall on a VAWT was done by Ferreira *et al.* (2007) which was verified and validated with Particle Image Velocimetry (PIV) measurements. The results indicated that a single turbulence model scheme for the numerical simulation of a 2D Darrieus VAWT at low tip-speed ratios is not suitable. A 2D computational research on the dynamic stall associated with unsteady flow around an NACA0012 airfoil was done by Wang *et al.* (2010) at a low Reynolds number which showed that the vortex-shredding predominated flow structure was well captured by the CFD prediction. Some research has been carried out on the discretization of CFD as well. Four meshing methods were studied by Almohammadi *et al.* (2013), i.e. mesh refinement, General Richardson Extrapolation (GRE), Grid Convergence Index (GCI), and fitting method using the URANS equations. Out of these methods, the fitting method was proved to be most promising in CFD meshing. In order to study the unsteadiness of augmented wind turbines, Nobile *et al.* (2014) used 2D CFD and proved that while the time step used in the simulation had a really small impact on the results, the forces generated on the blades of an open rotor depended highly on mesh resolution and model used for turbulence fields. The accuracy of the prediction is highly dependent on the turbulence model used and hence some of the research in the field of 2D CFD modelling is focused on different turbulence models for VAWTs. Two different models were used by each McNaughton *et al.* (2014) and Lanzafame *et al.* (2014) to predict the performance of a VAWT using 2D CFD models. McNaughton *et al.* (2014) used k-ω-SST models in standard forms and with correction for low-Reynolds number effects and observed that the power coefficients obtained from their study were greater than the experimental results. Lanzafame *et al.* (2014) used ANSYS fluent for their study. They used the RANS turbulence and Transition SST turbulence models and found that the SST turbulence models were better for the simulations of Darrieus VAWTs and the results obtained using this model were closer to the results obtained from experimental methods (figure 2.4).

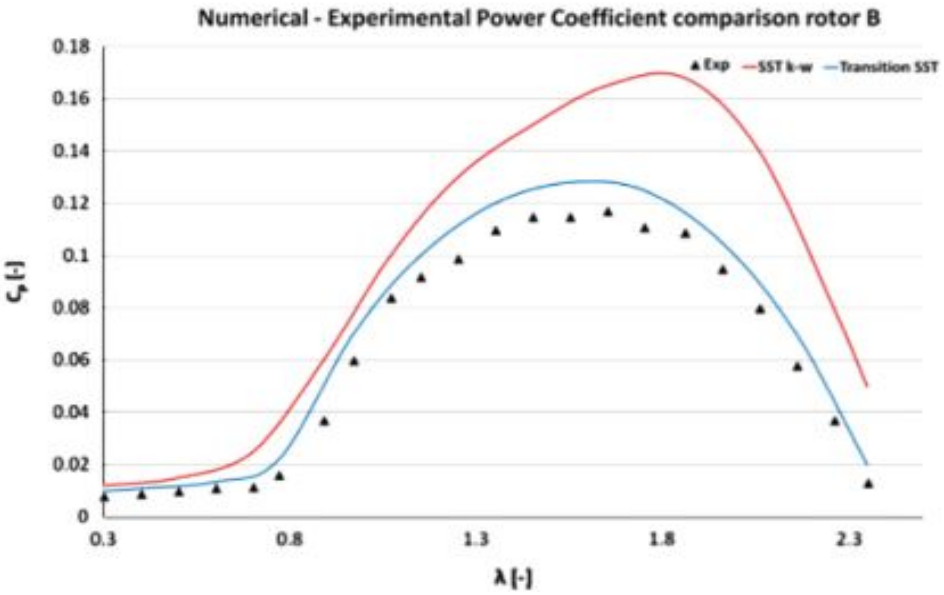

Figure 2.4: Comparison of variation of power coefficient obtained from SST models and experimental methods Lanzafame *et al.* (2014).

2. 2.5D CFD models: 2D CFD approach has been used in the aerodynamic analysis of Darrieus VAWTs by most researchers since there are limited computational resources. When compared with the experimental results, the results of 2D CFD analyses overestimate the power coefficients. Li *et al.* (2013) studied the 2D URANS, 2.5D URANS and 2.5D LES models. A short segment of the blade was chosen to be modelled in 2.5D model. This segment was in the span wise direction. This segment can be seen in figure 2.5. It was found from the study that the lift and drag forces along with the post-stall

angles of attack (AOAs) were over predicted by the 2D URANS models. Although the results predicted by 2.5D URANS models were slightly better, but due to the limited capability of the URANS model, the improvement in these results was restricted. Additionally, the results predicted by the 2.5D LES model were much closer to the experimental results.

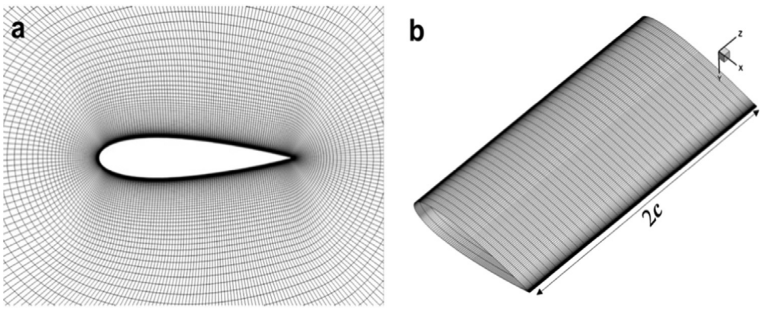

Figure 2.5: 2.5D CFD model scheme (a) Mesh distribution near an airfoil (b) Mesh distribution on the blade segment (Li *et al.*, 2013)

3. 3D CFD models: With improving computer technology, 3D CFD simulations of Darrieus VAWTs has emerged. Even though it requires most computational resources, this model provides the most accurate results amongst the CFD models and can be used to investigate aerodynamic mechanisms in detail. Due to the bad self-starting performance of the Darrieus VAWTs, 3D CFD has emerged as the best way to analyze this problem. Using 3D CFD models, Castelli *et al.* (2011) developed a model to evaluate the aerodynamic and inertial contributions to a VAWT blade's deformation (Castelli *et al.*, 2013). A full RANS unsteady calculation of a three-bladed rotor architecture was conducted by them for the development of this model. To study the self-starting performances of Darrieus VAWTs Rossetti and Pavesi (2013) used 3D CFD methods and compared the results with those of BEM theory and 2D CFD. In order to study the aerodynamic characteristics of VAWTs, Howell *et al.* (2010) combined the computational analysis with experimental research and investigated the accuracy of 3D CFD.

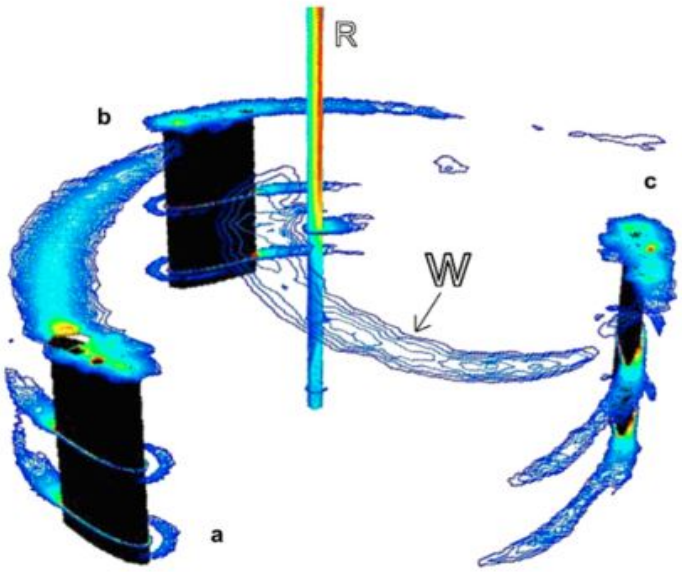

Figure 2.6: Contours of vortices for 3D CFD model used by Howell *et al.* (2010).

The results of this study were compared to those of 2D CFD and experiments. It was found that the results of 3D CFD were close to the results of the experiments (figure 2.7).

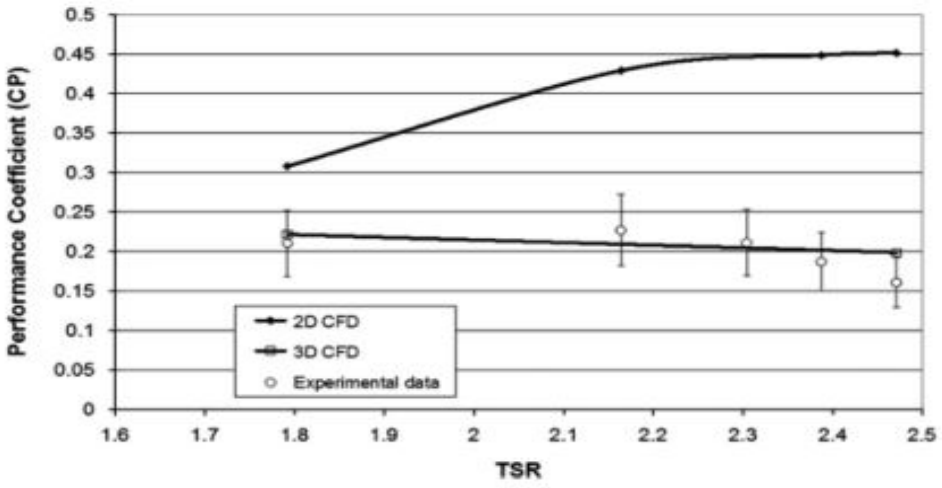

Figure 2.7: Comparison of coefficient of power obtained at various tip-speed ratios for 2D CFD, 3D CFD and experiments Howell *et al.* (2010).

Some research has also been conducted on the configurations of multiple-VAWT systems. Two types of multiple VAWT configuration were studied by Durrani *et al.* (2011) in their 2D numerical analysis of a VAWT wind farm for finding a suitable configuration for urban rooftops. CFD analysis of the configurations was done using the software 'Fluent'. The first configuration that was simulated was the 'I-type' (figure 2.8) configuration in which two turbines were collinear with the oncoming free air stream and were separated by a distance which was equal to two times the diameter (edge to edge) of an individual turbine while in the second case the distance between the turbines was four times the diameter (again edge to edge) of an individual turbine and the turbines were placed in a 'T-type' configuration (figure 2.9). Two turbines were placed at a distance of two times the diameter of an individual turbine lateral to the free air stream. The third turbine was placed at a horizontal distance of four times the diameter of an individual turbine behind the two turbines. This turbine was placed exactly at half the distance between the turbines at the front. The coefficient of power was measured along with the change in the tip-speed ratios of the turbines.

It was concluded that the 'I-type' configuration was the worst while the best performance was observed in the |'T-type' configuration with the horizontal distance between the turbines equal to two times the diameter of an individual turbine. The performance of the downwind turbine was higher than an individual turbine due to the suction effects occurring due to the two upstream turbines. The performance improvement decreased with increase in the horizontal distance between the upstream and downstream turbines. It was recommended that a single bigger turbine with a higher rated power should be used instead of 'I-type' configurations in places with spacial constraints.

Figure 2.8: Two VAWTs placed in line with a horizontal distance of 4 times the diameter (I-type)

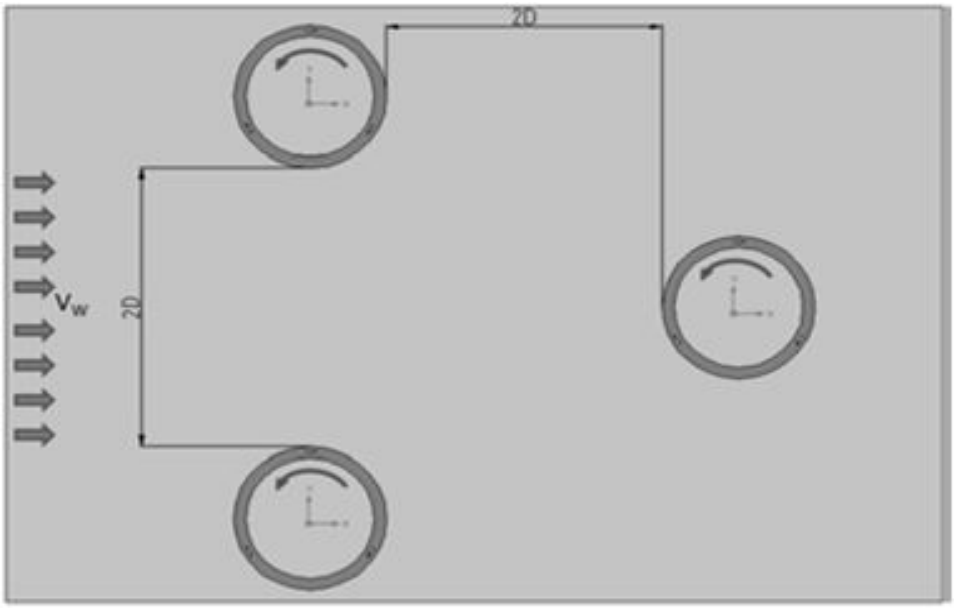

Figure 2.9: Three VAWTs, with the horizontal and lateral distance of 2 times the diameter (T-type)

2.2. EXPERIMENTAL METHODS

Experimental methods are another type of basic research methods that are used to analyse the behaviour of VAWTs. Most of the experiments in this method are carried out in wind tunnels under controlled conditions. Wind tunnel tests are primarily aimed at obtaining the characteristic curves as the basis of design. Some of the experimental methods are coupled with numerical simulations in order to validate the models used for the simulations. The impact of motion of the structure on the aerodynamic mechanism is also studied through experimental methods. Some Particle Image Velocimetry (PIV) measurements have also been performed to study the aerodynamic performances of VAWTs (Jin *et al.*, 2015).

Li *et al.* (2015) evaluated the aerodynamic forces on a straight bladed VAWT by changing the number of blades in the turbine. The number of blades ranged from 2 to 5 in this experiment. The airfoil used to produce the blades was NACA 0021. The schematic of the experimental apparatus and the wind tunnel used for the experiments can be seen in figures 2.10 and 2.11. The pressure distribution on the surface of the rotor blades was measured during the experiments and with the help of this distribution the coefficients of tangential force, normal force, lift force and drag force were found out. Further, the coefficients of torque and power of the turbine were found out as a function of the azimuthal position of a single blade. These parameters were investigated for different number of blades. It was concluded that the power absorbed by the turbine from the wind depended on the azimuthal angle of the turbine in the upstream region. The values of the power coefficient for an individual blade decreased from 0.410 at 2 blades to 0.326 at 5 blades. The two bladed turbine was found to have a higher annual generating capacity at areas with higher wind velocity while the five bladed turbine had a higher annual generating capacity at low wind velocity areas.

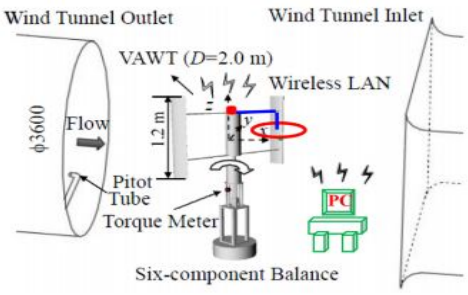

Figure 2.10: Schematic diagram of the apparatus used for the experiment (Li *et al.*, 2015)

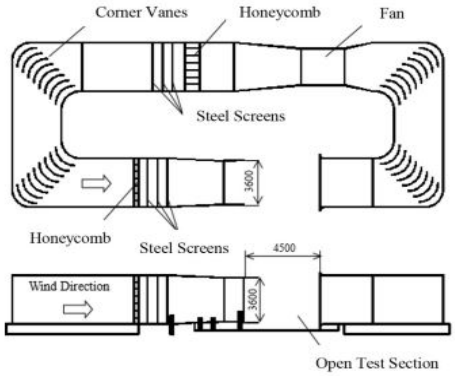

Figure 2.11: Schematic diagram of the apparatus used for the experiment (Li *et al.*, 2015)

Burlando *et al.* (2015) studied the flow fields in the wind tunnel using experimental tests on a Savonius VAWT and then used the results from the experimental tests to validate a CFD model. In the end it was shown how the results obtained from the experimental tests could be extended to more general conditions by studying the numerical model. A grid turbulence generator was used by Ahmadi-Baloutaki *et al.* (2015) to study the effect of extrnal free-stream turbulence. The turbulence was generated upstream of the turbine. A schematic of the experimental setup can be seen in figure 2.12. The intensities of the turbulence used were 5%, 7.5% and 10%. The generated turbulence had uniform mean flow profiles with no wind shear effects. The turbulent flows increased the output power of the turbine when compared to the smooth flow case which had a turbulence intensity of 0.5%. For the tip-speed ratio range studied in this experiment, it was observed that the increase in the coefficient of power due to the turbulence generated by the grid was small. An improvement in the self starting behaviour of the turbine was also observed in the presence of free stream turbulence.

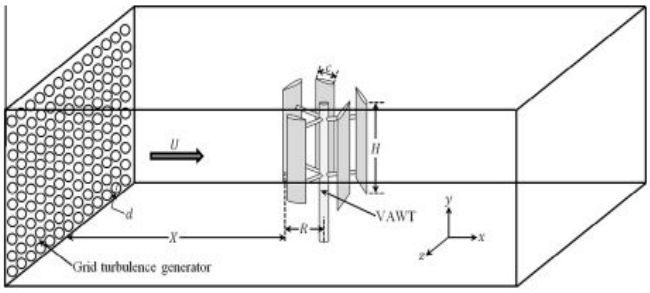

Figure 2.12: Schematic illustration of the grid turbulence generator and VAWT (Ahmadi-Baloutaki *et al.*, 2015).

Fujisawa and Takeuchi (1999) studied the flow field around a Darrieus rotor in dynamic stall using flow visualization and Particle Image Velocimetry (PIV). Dye injection technique was used to carry out the flow visualization and PIV combined with a conditional imaging technique was used to measure the phase averaged velocity distributions around the blade in this experiment. The flow field was studied for three different tip-speed ratios of 1, 2 and 3. Flow field around the rotor rotating at a tip-speed ratio of 3 at an azimuth angle of 0^o is shown in figure 2.13.

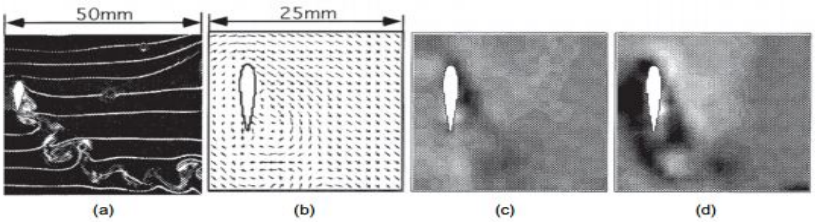

Figure 2.13: Flow field around rotor at an azimuth angle of 0^o for a tip-speed ratio of 3 (a) Flow visualization (b) Velocity vectors (c) Vorticity (d) Velocity magnitude (Fujisawa and Takeuchi, 1999).

The results indicated that the flow pattern varied in and around the rotor along with variation in formation of stall vortices. Two pairs of mushroom type vortices were produced due to flow separation over the suction surface of the blade and the corresponding roll up motion of the flow over the outer surface of the blades. One cycle of rotation lead to the formation of these stall vortices and the stall vortices due to the second rotation strongly modified the flow field near the downstream side of the blade which indicated the presence of a blade vortex interaction. It was concluded that this interaction may affect the aerodynamic performance of the rotor at low tip-speed ratios.

Ferreira *et al.* (2009) studied the effect of dynamic stall on a VAWT at low speed ratios by means of 2D PIV. The development of flow on the suction side of the airfoil of a small urban VAWT was visualized for two different reference Reynolds numbers and three different tip-speed ratios. The main parameter used to describe the flow over the rotation of the blade is shed vorticity. For a tip-speed ratio of 2, the circulation of the leading edge vortex was was quantified. The development of circulation of the leading edge separated vortex at various azimuthal angles can be seen in figure 2.14. The results identified the two phase locked and random components of the flow field. The largest angles of attack and shedding of largest amounts of vorticity were observed at the tip-speed ratio of 2. The results of the experiment were found to be useful for validating the numerical models. The results gave a reasonable description of part of the development of the dynamic stall process while presenting a useful estimate of the strength of the shed vorticity.

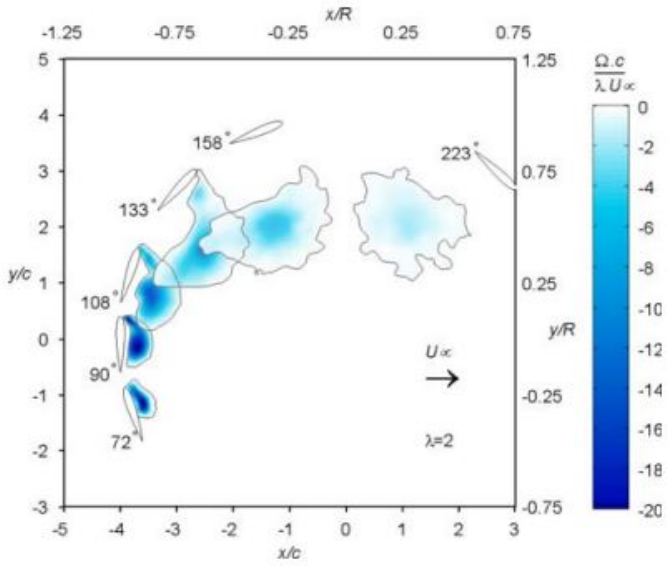

Figure 2.14: Evolution of the circulation of leading edge separated vortex for tip-speed ratio of 2 at azimuthal angles of 90^o, 108^o, 133^o and 158^o (Ferreira *et al.*, 2009).

Tescione *et al.* (2014) used standard PIV and stereoscopic PIV to study the evolution of near wake of a H-rotor VAWT. The wake dynamics were studied in this experiment at the turbine mid span horizontal plane. Additionally, the 3D wake geometry and the evolution of blade tip vortices were studied at several vertical planes. These planes were aligned with the free stream. The geometry of the wake in the mid span horizontal plane and in the vertical planes can be seen in figures 2.15 and 2.16 respectively. Standard PIV was used to study the wake evolution in the mid span horizontal plane while the stereoscopic PIV was used to study the wake evolution in the vertical planes at the cross stream locations. In the mid span horizontal plane, an asymmetric behaviour was observed. The velocity profile was skewed with the expansion more pronounced at the windward side. The blades released a non-constant vorticity sheet in the first part of the wake which is defined as the distance that is three times the radius of the turbine from the centre of the turbine in the streamwise direction. Significant vertical contraction was observed in the middle part of the turbine when the measurements at the cross stream vertical planes were analyzed. The expansion of the wake was asymmetric at the edges and had a more pronounced divergence at the windward side. For a distance greater than this, the contra-rotating vortices at the edges of the stream were the only relevant structures and the wake appeared as a smooth induction field in the mid span horizontal. The blade wakes were not detectable at this distance. The same observations were found for the cross stream vertical planes.

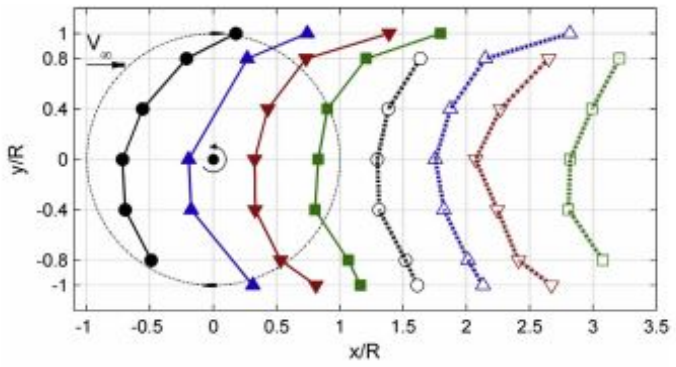

Figure 2.15: Geometry of wake in the mid span horizontal plane (Tescione *et al.*, 2014)

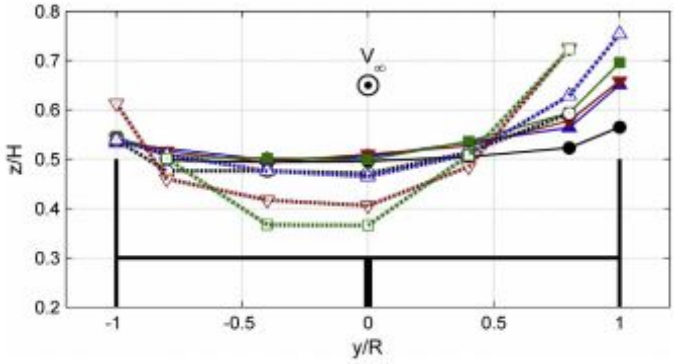

Figure 2.16: Geometry of wake in the vertical planes (Tescione *et al.*, 2014)

Surface roughness is another factor that affects the power generated by a VAWT. Howell *et al.* (2010) found out that the performance of a turbine was enhanced when the surface of the blades of a straight bladed VAWT was roughened but only upto a Reynolds number of 30,000. Beyond this Reynolds number, the coefficient of the performance of the turbine decreased. The effect of attachments on the blades of VAWTs has also been analyzed in some studies. Li *et al.* (2010) simulated the conditioning of rime-type icing on the leading edges surface of a straight bladed VAWT. The effect of mass of the attachments on the blades of the turbine can be seen in figure 2.17.

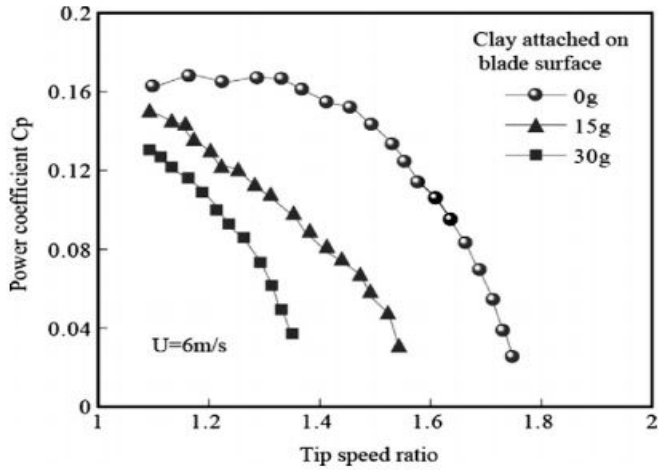

Figure 2.17: Effect of mass of attachments on the performance of the turbine (Li *et al.*, 2010)

A reduction in the rotation and power performance of the turbine with the increase in the mass was observed in this study. The increase in the mass of the attachments and the wind speed, increased the rates of reduction of the turbines. This reduction was attributed to the imbalance of the rotor weight caused by the attachments and the change in the airfoil geometry which led to a variation in the aerodynamic characteristics of the blade.

2.3. COMBINED SOURCE AND DOUBLET PANEL METHOD

For this study, the aerodynamic model used for simulation of VAWT was the combined source and doublet panel method. Using this model the aeroelastic code U2DiVA was developed by Ferreira (2009). This aeroelastic code has been discussed further in section 3.5. In this model surface of the airfoil is divided into a number of panels where each panel has a constant local source and doublet strength of its own.

The source is the origin of a type of two-dimensional incompressible flow known as source flow from which all the streamlines emanate in the shape of straight lines. When the streamlines are directed towards the origin the flow is called the sink flow. Both these flows can be seen in figure 2.18. The velocity along the streamlines (V_r) varies inversely with the distance (r) from the origin O in both these cases. No tangential velocity exists in both of these flows.

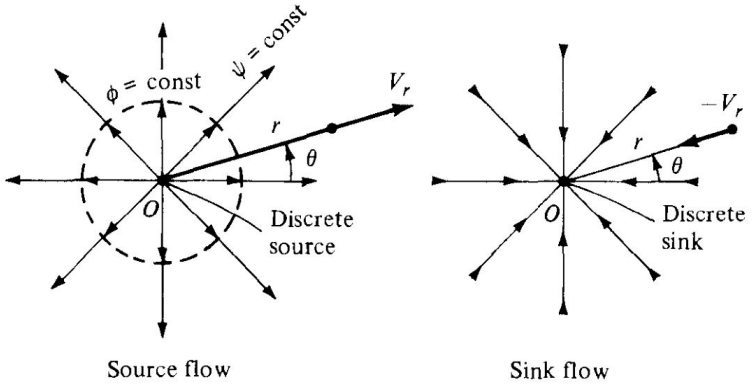

Figure 2.18: Source and sink flows (Anderson,Jr., 2001)

The radial velocity for a source flow is given by the following equation:

$$V_r = \frac{\Lambda}{2\pi r} \tag{2.1}$$

For a sink flow, the radial velocity is given by:

$$V_r = -\frac{\Lambda}{2\pi r} \tag{2.2}$$

In the above equations, Λ is the strength of the source (or sink) which is physically the rate of volume flow from the source, per unit depth perpendicular to the page and has the units square meters per second (m^2/s). The equations for the streamlines for any irrotational flow can obtained by equating a function called stream function (ψ) to a constant. The velocity for any irrotational flow is obtained by the gradient of a scalar function called potential function (ϕ). Cylindrical co-ordinates are used to define the governing equations of this flow. The stream function for the source flow is as follows:

$$\psi = \frac{\Lambda}{2\pi}\theta \tag{2.3}$$

For the sink flow the stream function is as follows:

$$\psi = -\frac{\Lambda}{2\pi}\theta \tag{2.4}$$

The potential function for the source flow is as follows:

$$\phi = \frac{\Lambda}{2\pi}\ln r \tag{2.5}$$

Following is the potential function for the sink flow:

$$\phi = -\frac{\Lambda}{2\pi} \ln r \tag{2.6}$$

The doublet flow is another type of flow that consists of a source-sink pair. Both, the source and the sink have equal (Λ) but opposite strengths and are separated by a distance l. l approaches zero while the absolute magnitudes of the strengths of source and sink increase in such a manner that their product $l\Lambda$ remains constant (figure 2.19). The strength of the doublet is defined by this product and is denoted by κ (figure 2.20).

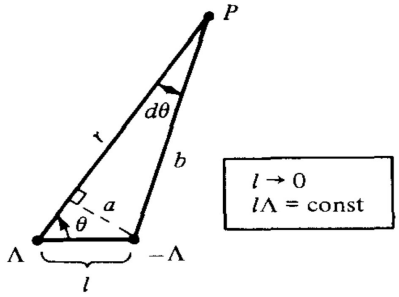

Figure 2.19: Limiting case for a doublet (Anderson,Jr., 2001)

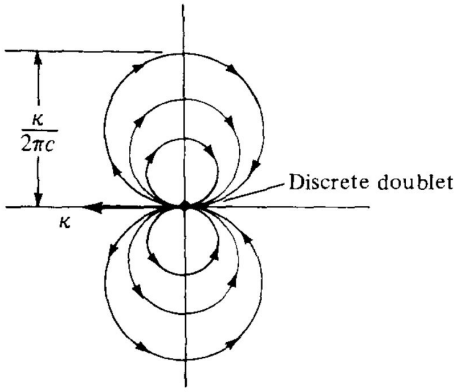

Figure 2.20: Doublet flow (Anderson,Jr., 2001)

The radial (V_r) and the tangential (V_θ) velocities are given as follows:

$$V_r = -\frac{\kappa cos\theta}{2\pi r^2} \tag{2.7}$$

$$V_\theta = -\frac{\kappa sin\theta}{2\pi r^2} \tag{2.8}$$

The stream function (ψ) and the potential function (ϕ) are defined as follows (Anderson,Jr., 2001):

$$\psi = -\frac{\kappa sin\theta}{2\pi r} \tag{2.9}$$

$$\phi = \frac{\kappa cos\theta}{2\pi r} \tag{2.10}$$

For the combined source and doublet panel method, first the surface of the airfoils is divided into a number of panels (N) using the full-cosine method (figure 2.21). The main advantage of this distribution is that the panel density is larger at the edges of the airfoil. The panels are formed chordwise using the following equation:

$$x = \frac{c}{2}(1 - cos\beta) \tag{2.11}$$

The intervals at which end points of panels are created specified as follows:

$$\Delta\beta = \frac{\pi}{N} \tag{2.12}$$

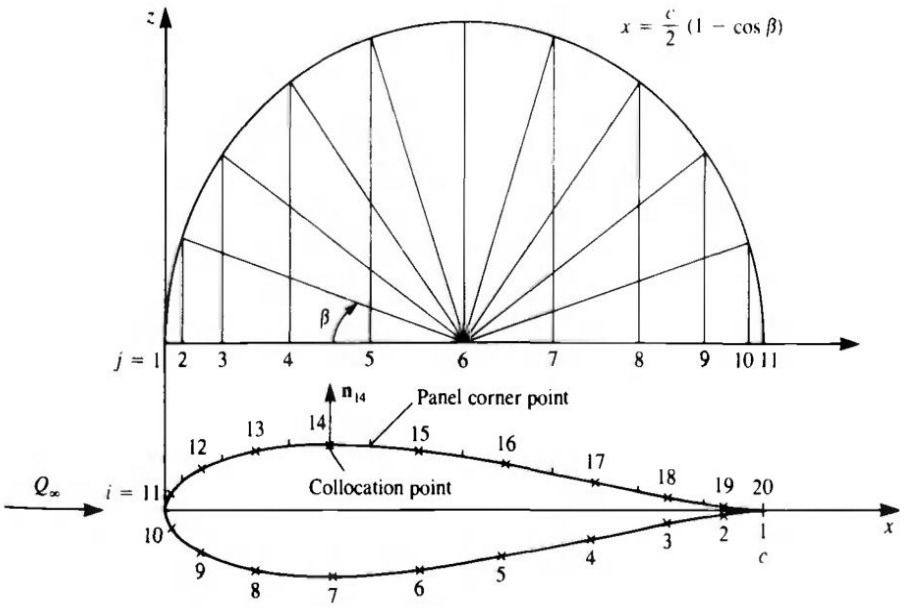

Figure 2.21: Full-cosine method of spacing the panels (Katz and Plotkin, 2000)

The number of cornerpoints of the panels is N+1. An additional panel is added at the trailing edge of the airfoil along the x-axis to model the wake of the airfoil and it is modelled using a doublet of strength μ_W. At the centre of each panel, the boundary conditions are specified and these points are known as 'Collocation Points'. The total internal velocity potential ϕ_i is divided into free-stream potential ϕ_∞ and perturbation potential ϕ. The boundary condition used for this method is the Dirichlet boundary condition which specifies that the total velocity potential (ϕ_i) inside the body remains constant. For using Dirichlet boundary condition, the Neumann boundary condition is used which states that the velocity component normal to the surface of the airfoil is equal to zero and is specified as follows:

$$\frac{\partial \phi_i}{\partial n} = 0 \tag{2.13}$$

In order to fulfill this condition, the collocation points are placed slightly inside the body. Also, the total internal potential is equated to free stream potential ϕ_∞. This makes the total internal potential zero. For this case the source strength at each panel is given by:

$$\sigma = \vec{n} \cdot \vec{Q_\infty} \tag{2.14}$$

In the above equation $\vec{n}$ is unit vector perpendicular to the surface of the panel, $\vec{Q}_\infty$ is the velocity of the free-stream and σ is the source strength of each panel. For a surface divided into N panels, the numerical solution using the Dirichlet boundary condition is given as follows:

$$\sum_{j=1}^{N} \frac{1}{2\pi} \int_{panel} \sigma \ln(r) dS - \sum_{j=1}^{N} \frac{1}{2\pi} \int_{panel} \mu \frac{\partial}{\partial n} (\ln r) dS = 0 \tag{2.15}$$

The influence of the doublet element of j^{th} panel at a given point is:

$$\frac{1}{2\pi} \int_{panel} \frac{\partial}{\partial n} (\ln r) dS \Big|_j \equiv C_j \tag{2.16}$$

and that of the source element of the same panel is given by:

$$\frac{-1}{2\pi}\int_{panel}(\ln r)\,dS\Big|_j \equiv B_j \tag{2.17}$$

Therefore equation 2.15 becomes:

$$\sum_{j=1}^{N} B_j\sigma_j + \sum_{j=1}^{N} C_j\mu_j = 0 \tag{2.18}$$

The velocity potential due to the constant-strength source element of a panel with end points defined as (x_1,y_1) and (x_2,y_2) at a point (x,y) that does not lie on the surface of the panel is given by:

$$\phi = \frac{\sigma}{4\pi}\left\{(x-x_1)\ln\left[(x-x_1)^2+y^2\right]-(x-x_2)\ln\left[(x-x_2)^2+y^2\right]+2y\left(\tan^{-1}\frac{y}{x-x_2}-\tan^{-1}\frac{y}{x-x_1}\right)\right\} \tag{2.19}$$

and due to a constant-strength doublet element at the same point is given by:

$$\phi = -\frac{\mu}{2\pi}\left[\tan^{-1}\frac{y}{x-x_2}-\tan^{-1}\frac{y}{x-x_1}\right] \tag{2.20}$$

Next the increment in the velocity potential at each collocation point i due to the unit-strength source element and the unit-strength doublet element of panel j are calculated using the two equations mentioned above and are denoted by b_{ij} and c_{ij} respectively. The influence of a source panel on itself is calculated using equation 2.19 and that of a doublet panel on itself (c_{ii}) is equal to 0.5.

Since the wake doublet is included in this calculation as well, the determination of influence of doublets at each and every collocation point will lead to generation of a N× N matrix with N+1 unknowns. The equation required to correct this situation is provided by Kutta condition. The Kutta condition states that the sharp trailing edge of an airfoil is left smoothly by the flow and the velocity of flow at this edge is finite. This means that the circulation at the trailing edge is zero and the vortex generated due to the doublet strength difference between the first and the N^{th} panels is cancelled by the wake doublet. Hence, the Kutta condition for this case is specified as follows:

$$(\mu_1-\mu_N)+\mu_W = 0 \tag{2.21}$$

When the above equation is combined with the generated matrix for influence of doublets the order of the matrix becomes N+1 and it is defined as follows:

$$\sum_{i=1}^{N+1}\sum_{j=1}^{N+1} C_{ij}\mu_j = \begin{pmatrix} c_{11} & c_{12} & \dots & \dots & c_{1N} & c_{1W} \\ c_{21} & c_{22} & \dots & \dots & c_{2N} & c_{2W} \\ \dots & \dots & \dots & \dots & \dots & \dots \\ c_{N1} & c_{N2} & \dots & \dots & c_{NN} & c_{NW} \\ 1 & 0 & 0 & \dots & -1 & 1 \end{pmatrix}\begin{pmatrix}\mu_1\\ \mu_2\\ \dots\\ \mu_N\\ \mu_W\end{pmatrix} \tag{2.22}$$

μ_W is then replaced by μ_N-μ_1 and the order of the generated matrix for the influence of doublets is reduced to N. The doublet influence is rewritten as follows:

$$a_{ij} = c_{ij}, \quad j \neq 1, N \tag{2.23a}$$

$$a_{i1} = c_{i1} - c_{iW}, \quad j = 1 \tag{2.23b}$$

$$a_{iN} = c_{iN} + c_{iW}, \quad j = N \tag{2.23c}$$

With the a similar matrix generated for the influence of sources, equation 2.18 becomes:

$$\begin{pmatrix} a_{11} & a_{12} & \dots & \dots & a_{1N} \\ a_{21} & a_{22} & \dots & \dots & a_{2N} \\ \dots & \dots & \dots & \dots & \dots \\ \dots & \dots & \dots & \dots & \dots \\ a_{N1} & a_{N2} & \dots & \dots & a_{NN} \end{pmatrix}\begin{pmatrix}\mu_1\\ \mu_2\\ \dots\\ \dots\\ \mu_N\end{pmatrix} + \begin{pmatrix} b_{11} & b_{12} & \dots & \dots & b_{1N} \\ b_{21} & b_{22} & \dots & \dots & b_{2N} \\ \dots & \dots & \dots & \dots & \dots \\ \dots & \dots & \dots & \dots & \dots \\ b_{N1} & b_{N2} & \dots & \dots & b_{NN} \end{pmatrix}\begin{pmatrix}\sigma_1\\ \sigma_2\\ \dots\\ \dots\\ \sigma_N\end{pmatrix} = 0 \tag{2.24}$$

The source strength is calculated using equation 2.14 and the second matrix multiplication in equation 2.24 is then executed and moved to the right-hand side of the equation. This product is rewritten as:

$$\begin{pmatrix} RHS_1 \\ RHS_2 \\ \dots \\ \dots \\ RHS_N \end{pmatrix} = - \begin{pmatrix} b_{11} & b_{12} & \dots & \dots & b_{1N} \\ b_{21} & b_{22} & \dots & \dots & b_{2N} \\ \dots & \dots & \dots & \dots & \dots \\ \dots & \dots & \dots & \dots & \dots \\ b_{N1} & b_{N2} & \dots & \dots & b_{NN} \end{pmatrix} \begin{pmatrix} \sigma_1 \\ \sigma_2 \\ \dots \\ \dots \\ \sigma_N \end{pmatrix} \tag{2.25}$$

The equation 2.24 then takes the form:

$$\begin{pmatrix} a_{11} & a_{12} & \dots & \dots & a_{1N} \\ a_{21} & a_{22} & \dots & \dots & a_{2N} \\ \dots & \dots & \dots & \dots & \dots \\ \dots & \dots & \dots & \dots & \dots \\ a_{N1} & a_{N2} & \dots & \dots & a_{NN} \end{pmatrix} \begin{pmatrix} \mu_1 \\ \mu_2 \\ \dots \\ \dots \\ \mu_N \end{pmatrix} = \begin{pmatrix} RHS_1 \\ RHS_2 \\ \dots \\ \dots \\ RHS_N \end{pmatrix} \tag{2.26}$$

The above matrix equation has N equations and N unknown values of μ for which the equation is then solved. Once the doublet strength for each panel has been calculated, the external potential (ϕ_e) for each panel can be calculated as well. This potential is equal to the sum of internal potential (ϕ_i) and the potential jump across the surface (figure 2.22).

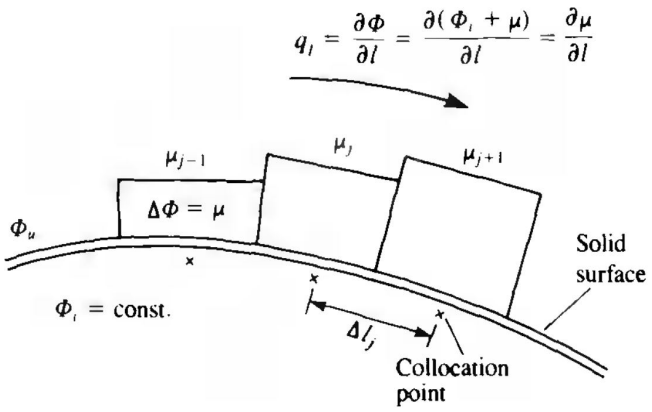

Figure 2.22: Doublet panels on the surface of the airfoil (Katz and Plotkin, 2000)

The external potential is defined as:

$$\phi_e = \phi_i + \mu \tag{2.27}$$

Since the internal potential is already equal to zero, the external potential at a particular panel is equal to the potential jump across that panel. The tangential velocity at a particular panel with potential jump μ is defined as:

$$Q_t = \frac{\partial \phi_e}{\partial l} = \frac{\partial \mu}{\partial l} \tag{2.28}$$

The pressure coefficient (C_{P_j}) of the j^{th} panel is then calculated using the following equation:

$$C_{P_j} = 1 - \frac{Q_{t_j}^2}{Q_\infty^2} \tag{2.29}$$

The contribution of the panel to the lift coefficient is then calculated as:

$$\Delta C_{l_j} = -C_{P_j} \Delta l_j \cos \alpha_j \tag{2.30}$$

The variables Δl_j and α_j are defined in the following figure:

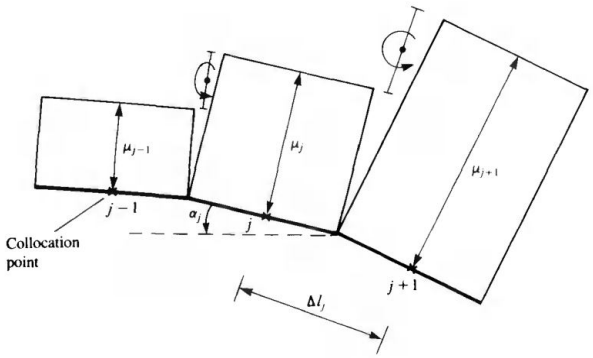

Figure 2.23: Segment with constant strength doublet panels (Katz and Plotkin, 2000)

The total lift and the total moment calculated by summing up the lift and the moment contributed by each panel:

$$L = \sum_{j=1}^{N} \Delta L_j \tag{2.31}$$

$$M_O = \sum_{j=1}^{N} \Delta L_j \left(x_j \cos \alpha \right) \tag{2.32}$$

The lift contribution by a panel (ΔL_j) is calculated as:

$$\Delta L_j = -\rho Q_\infty \left(\mu_{j+1} - \mu_j \right) \tag{2.33}$$

In the above equation, Q_∞ is the speed of the free-stream of the fluid and ρ is the fluid density. The non-dimensional coefficients for lift and moment are calculated as follows:

$$C_l = \frac{L}{\frac{1}{2}\rho Q_\infty^2 c} \tag{2.34}$$

$$C_{m_0} = \frac{M}{\frac{1}{2}\rho Q_\infty^2 c} \tag{2.35}$$

In the above equations, 'c' is the length of the chord of the airfoil.

2.4. CURRENT STATUS

As mentioned in the previous chapter, very few studies have been done to study the behaviour of VAWTs under turbulent wind. Merz (2012) developed a blade-element momentum method for VAWTs, which included both dynamic stall and dynamic inflow. The rotor had two or three blades and additional 'ghost' blades were defined about the rotor azimuth. Dynamic stall model was used by the author to allow the natural evolution of flow on the real and the ghost blades. This evolution of flow on each blade allowed the author to record the forces continuously on each blade and then calculate the dynamic inflow from the recorded forces. Typical operating conditions were simulated on a VAWT using this model using 36 blades which included both the real and the ghost blades. The motion of the platform of a floating VAWT was also simulated using a simple mass-spring-damper model. A schematic of the model can be seen in figure 2.24.

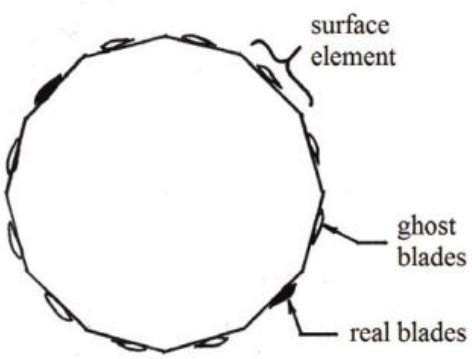

Figure 2.24: Schematic of the model describing both ghost blades and real blades. The number of blades in this schematic has been reduced for convenience of sketching (Merz, 2012)

This model produced almost the same rotor loads and platform motion as an iterative method that used quasi-static induced velocity. The main advantage of this model was that it eliminated iteration and the potential numerical instability in the induced velocity calculation. In case of unusual cases like the abrupt changes in the rotor speed, this model has a general applicability. It could also predict the evolution of the induced velocity for both a VAWT with aerodynamic control devices and a VAWT using a variable pitch with straight blades.

The development of multi megawatt turbines has received a sudden boost after the end of Èole 4 MW (figure 2.25) project in the early 1990s. It has been estimated that the cost of the blades of VAWTs can be lower when compared to those of HAWTs in the multi megawatt range. This may lead to a lower Cost of Energy (COE) for offshore wind power generation. The ongoing research is being carried out on both, the straight bladed and the Darrieus rotors. The earlier extensive research that has already been carried out on the HAWTs has benefited the ongoing research on VAWTs. The absence of egdewise loading on the blades of VAWTs has enabled the manufacturers to manufacture the blades into sections and then assemble them at the installation site. Sandia National Laboratories (SNL) is currently developing advanced rotors for US offshore wind power generation which is funded by the United States Department of Energy (US DOE). The design which is favoured by SNL is an innovated phi rotor. Offshore VAWTs in multi megawatt range are also being developed in some of the European countries (Tjiu *et al.*, 2015b).

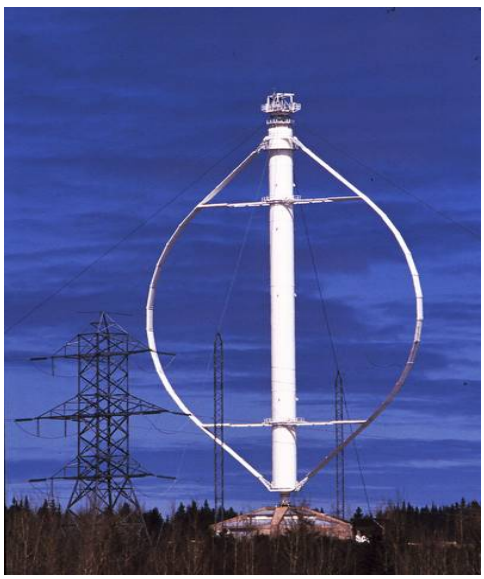

Figure 2.25: The Èole 4MW Darrrieus VAWT (Gipe, 2016)

Nakamura *et al.* (2013) developed a floating VAWT which was a combination of a floating VAWT and

counter-rotating water current turbine. The purpose of the water current turbine was to cancel the reaction torque of electric generator and generate some additional power from the water current. The turbine was a sub megawatt turbine with a rated power of 500 kW. The rotor of the wind turbine had three straight blades while the water current turbine was a two bucket-two layer Savonius turbine. The concept was named by the authors as Savonius Keel Wind turbine Darrieus (SKWID). The schematic drawing and the experimental model of the turbine can be seen in figure 2.26.

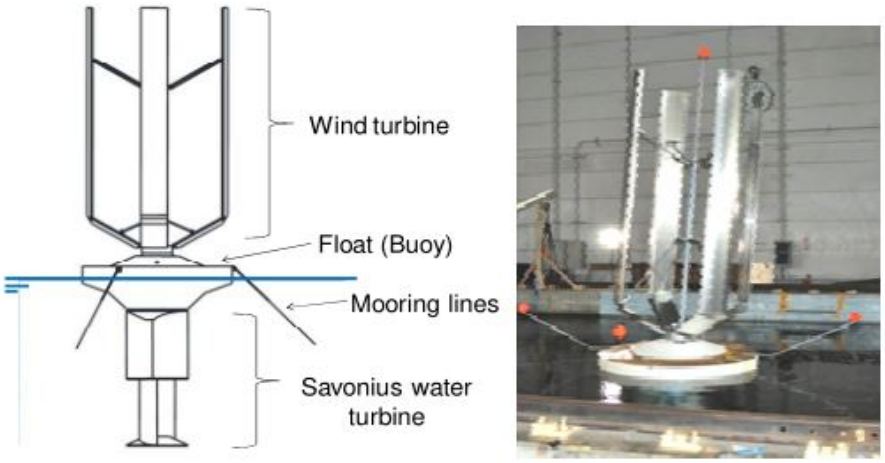

Figure 2.26: The schematic diagram (left) and experimental model (right) of the SKWID concept turbine (Nakamura *et al.*, 2013)

The authors observed that the torque cancellation in the turbine reduced the oscillations of the float and chain links which increased the operational life of the turbine. The expected energy production per unit area of the sea surface of the turbine was higher than the HAWTs.

Cahay *et al.* (2011) designed a 2MW VAWT with three helicoidal blades for offshore applications (figure 2.27). There were a few advantages of the helicoidal blades when compared to the straight blades. These were the reduction of dynamic stall during one rotation, minimization of torque variation during one rotation and simplicity in the manufacturing process of the blades. A 35kW onshore prototype was developed by the authors to test and validate the floating VAWT concept (figure 2.28).

Figure 2.27: Onshore prototype of the of the Vertiwind prototype (Cahay *et al.*, 2011)

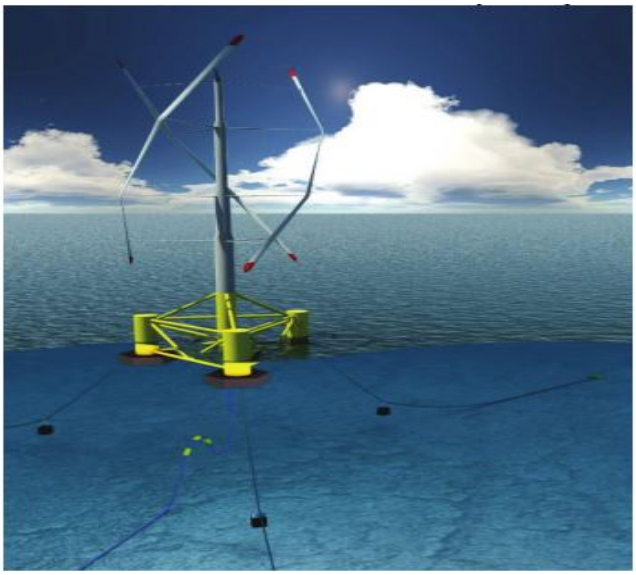

Figure 2.28: Offshore concept of the of the Vertiwind prototype (Cahay *et al.*, 2011)

The dynamic behaviour of the prototype was stable and in line with the aerodynamic and mechanical calculations. The measured power curve validated the predictions as well. Special focus was laid on the floater of the turbine. The standards of the offshore oil and gas industry were used to design the floater since there are no current standards to design the offshore floaters for wind turbines. The floater was designed to place the turbine at the centre of the rotor which ensured that the centre of gravity, the buoyancy and the convergence point of the mooring lines were all on the same axis.

As cited by Tjiu *et al.* (2015b), the Novel Offshore Vertical Axis (NOVA) turbines project which was launched in January 2009 aimed at reducing the Cost of Energy (COE) and install 1 GW of offshore VAWTs by 2020. A design named Aerogenerator was developed by British Aerodynamist David Sharpe in 2005 and developed by Wind Power Ltd. The rotor of the aerogenerator model was similar to a H-rotor but the support bars were tilted upwards at the pivotal hub. Several blades were there along the support bar in the early designs and guy wires were used to join each half of the bar together to improve the structural strength of the bars. A 6 KW prototype was designed and tested in the wind tunnels which showed achievable rated power and could withstand extreme wind speeds (above 28.6 m/s).

Another model was proposed on the basis of the findings from the aerogenerator concept in 2010 which had only two blades at the ends of the support bar and did not use guy wires on the support bar as well (figure 2.29). The full scaled version of this rotor would have a rated power of 10 MW with a height of 130m and a rotor diameter of 270m.

Figure 2.29: Aerogenerator X conecpt (Tjiu *et al.*, 2015b)

A gyroscopic analysis of the turbine was done to predict the characteristics of the turbine in response to rolling and pitching of the floating semi-submersible vessel on which the turbine was mounted. The gyroscopic moments did not have any significant effects on both rotor and vessel even though they caused significant motions at certain frequencies. This also proved that the low Centre of Gravity (COG) of the turbine was advantageous as it stabilized the turbine even in harsh sea conditions.

Another 10 MW offshore wind turbine was designed by VertAx Wind Ltd. to lower the cost of offshore wind energy (figure 2.30).

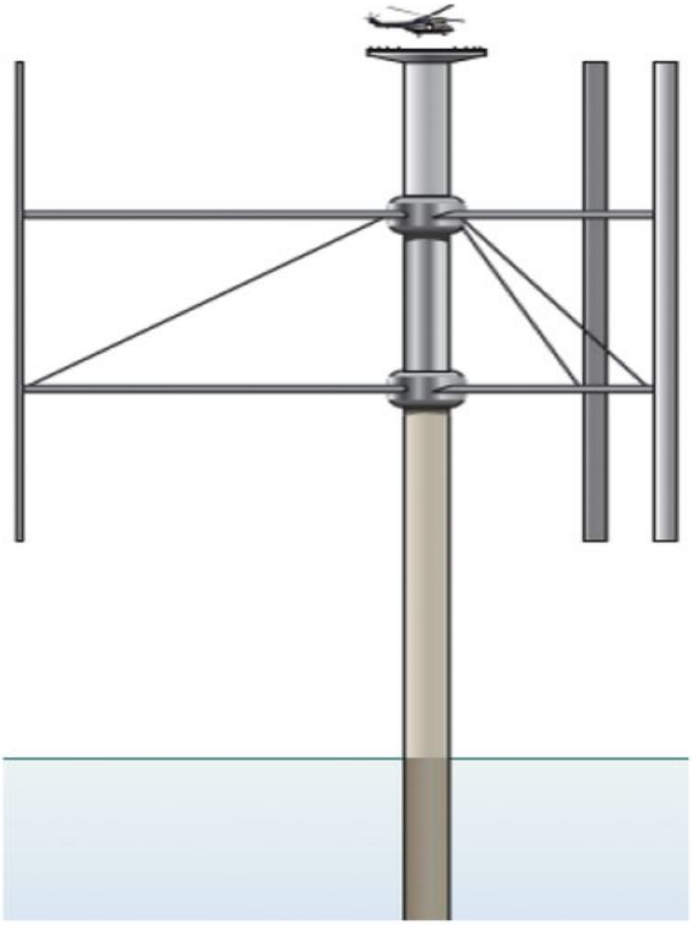

Figure 2.30: Proposed design of 10 MW VertAx turbine (Tjiu *et al.*, 2015b)

The diameter of the proposed rotor was 140 m while the length of the blades of the turbine was 110 m. The electricity was produced by the turbine using two 5 MW permanent magnet Direct Drive Generator (DDG) units. To ease the transport and logistics of the blade, they were manufactured in segments of 11 m. To maintain the strength, low weight and cost effectiveness of the blades, they were manufactured using composite materials. The speed of the turbine was 4 RPM at the rated power and the generator had 180 poles. The efficiency of the generators at full load was around 92.5%. A helipad was also placed on the top of the turbine to facilitate maintenance.

Dabiri (2011) investigated arrays of counter-rotating VAWTs of 10 m height in natural conditions in the summer of 2010 and achieved higher power output per unit area when compared to wind farms which consist of HAWTs. These investigations revealed that power densities of a magnitude greater than those of HAWT wind farms (typically around 2-3 MW per square meter of land area) could be achieved by arranging VAWTs in arrangements that enabled them to extract energy from the wakes of adjacent wind turbines and from above the wind farm. The improvements did not require any increase in wind turbine efficiency. Only closer wind turbine spacing and vertical fluxes of turbulent kinetic energy of sufficient magnitudes from the atmospheric surface layer were required for this. These wind farms would also help in the reducing the cost, size and environmental impacts of wind farms. Two configurations can be seen in figure 2.31. The configuration on

the left consists of three turbines while the one on right consists of two turbines.

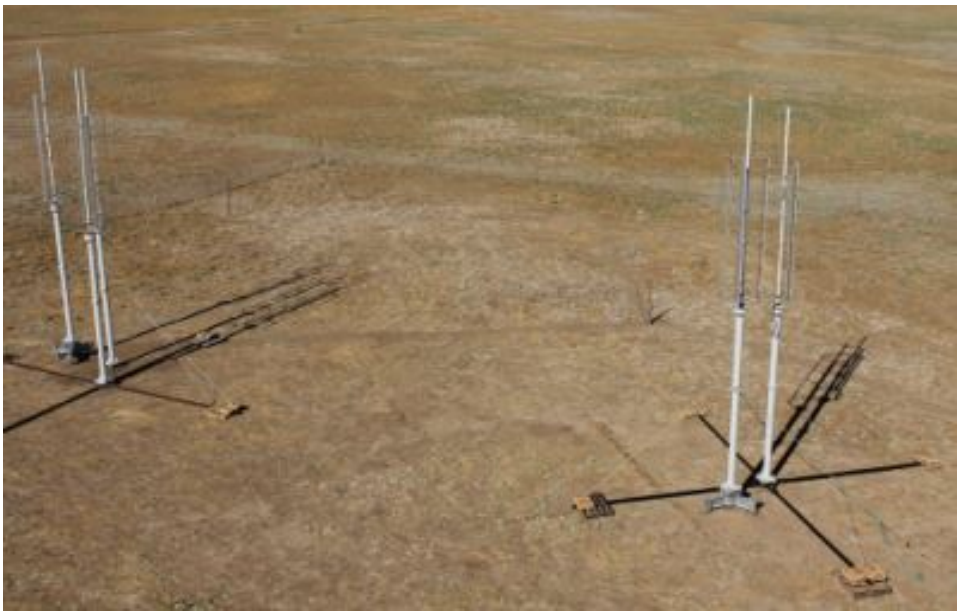

Figure 2.31: Sample configurations used by Dabiri (2011)

Another big project that was carried out to promote VAWTs was the 'Deewpind' project. A 5 MW offshore floating VAWT was designed by Verelst *et al.* (2014) in this project (figure 2.32).

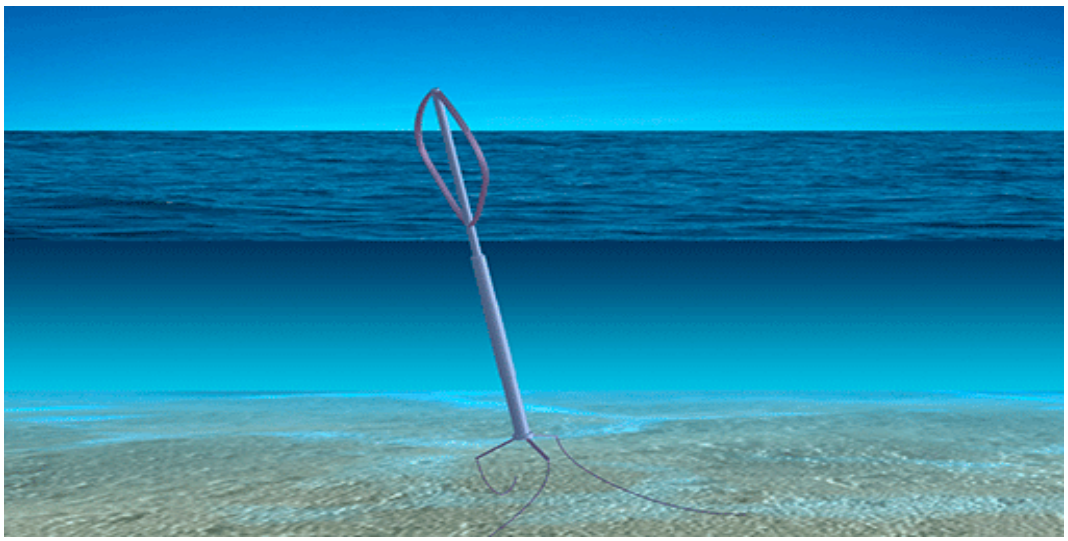

Figure 2.32: The Deepwind concept turbine (DeepWind, 2014)

This project was a part of the DeepWind project funded by European Union's Seventh Framework Programme for research, technological development and demonstration. This project was carried out between 2011 and 2014 (DeepWind, 2014). The simulation of the designed VAWT and load cases was done in the aeroelastic code HAWC2. The loads were calculated only for the normal operation of the turbine. Further details of the turbine can be seen in table 2.1. For the blades, NACA0025 airfoil was used for the upper and the lower sections while NACA0018 airfoil was used in the middle section. The length of the chords of the airfoils in each section was 5 m. The upper, middle and lower sections of the blades had lengths of 21.7 m, 149.29 m and 29.44 m respectively (Verelst *et al.*, 2014). The reference location for the turbine was the Hywind site which is located near the Norwegian sea coast (Paulsen *et al.*, 2014)

Table 2.1: Operational and geometric data of the Deepwind 5 MW turbine rotor (Verelst *et al.*, 2014)

Property	Value	
Rated electrical power	5	[MW]
Rated rotational speed	5.95	[rpm]
	0.62	[rad/s]
Rated wind speed	14	[m/s]
Cut in wind speed	4	[m/s]
Cut out wind speed	25	[m/s]
Number of blades	2	[-]
Rotor Diameter	121	[m]
Rotor height-to-diameter ratio	1.18	[-]
Blade chord	5	[m]
Solidity	0.165	[-]
Swept area	11996	[m^2]

The turbine was placed on a rotating spar platform. In order to design and simulate this VAWT, a module for VAWTs in HAWC2 was introduced. The actuator cylinder model was used to simulate VAWTs in this module. Pultrusion technology was used to manufacture the blades for the turbine. The material used to manufacture the blades was glass fibre reinforced epoxy with unidirectional fibre orientation. The material properties were assumed to be orthotropic (Verelst *et al.*, 2014). This technology was already implemented successfully by Sandia National Laboratories in their research on VAWTs between 1970s and 1990s. This manufacturing had proven to be cost competitive when compared to the manufacturing cost of HAWT blades despite the length of the blades of VAWTs being twice as long as their HAWT counterparts (Sutherland *et al.*, 2012). A schematic of the pultrusion process has been shown in figure 2.33.

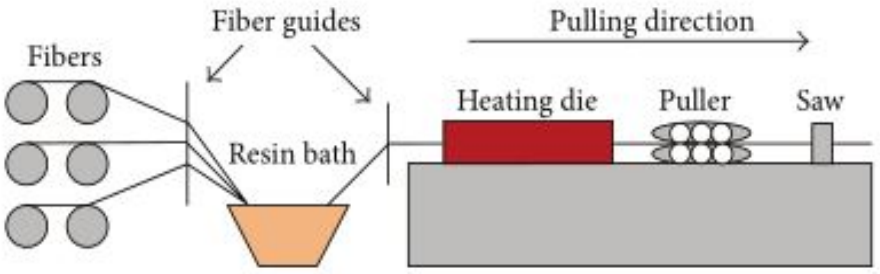

Figure 2.33: Schematic of Pultrusion process (Carlone *et al.*, 2013)

It was found that the strain level on the rotor during the real time operation was less than the predicted value of maximum strain limit under design loads obtained from HAWC2 simulations. The wind flow used for HAWC2 simulations was deterministic and the wind speed was 24 m/s at sea state 3. The electrical system of the turbine faced many challenges because of the undersea environment and very slow rotation speeds of the rotor. The results also showed that the rotor performed with expected performance without any horizontal struts throughout operational wind speed range without any stability problems. The influence of Magnus forces on the rotor could be controlled as well. Additionally, the simulation of fault in electrical network proved that rapid variations in generator torque should be avoided (Paulsen *et al.*, 2014).

A modified version of the rotor of this turbine has been used in this study which has been discussed in next chapter.

2.5. CONCLUSIONS

After the initial research on the VAWTs between 1970s and 1990s, the research came to an effective halt around mid 1990s. Reemergence of interest in VAWTs has occurred due to rise of interest in wind energy in built environment.

The three main research methods to analyse VAWT are Computational Aerodynamics, Computational Fluid Dynamics (CFD) and experimental methods. In computational aerodynamics method, the two main

models used for VAWT analysis were the momentum model and vortex model. While computational aerodynamics method has been used for a long time, the innovations and rapid development in computer science has given rise to CFD as a very effective method. Although they consume more time, CFD models are more accurate when compared to computational aerodynamics models. 3D CFD models have been most accurate amongst CFD models as their predictions are closer to the experimental results. Experimental methods have also seen some development in the last few years. Wind tunnel experiments and Particle Image Velocimetry (PIV) methods have been extensively used by some researchers to study the aerodynamics of VAWTs with some focus on the behaviour of the wake of the VAWTs as well. Most of the research in experimental methods is coupled with numerical simulations as well, in order to develop more accurate simulation methods and aeroelastic codes.

Since late 2000s, a lot of research has been carried out to promote offshore and urban VAWTs. Due to their better accessibility, greater stability and lower operational speeds, they would prove to be a better substitution for HAWTs in offshore applications. Some research on wind turbine arrays has been carried out as well. It was also found out in these studies that the energy produced per unit surface area by VAWT wind farms was higher when compared to HAWT wind farms. Some multi megawatt projects such as the SKWID concept, the Vertiwind concept and VertAx concept are also being carried out. These projects have turbines with a rated power up to 10 MW. Additionally, there has been much focus on the development of floating platforms for VAWTs.

Research on the behaviour of VAWTs to turbulent and unsteady wind has not been carried out extensively. Some experimental work has been carried out in this regard but simulation work has not been explored much. Most of the research that has been carried out on VAWTs has been under steady conditions. Hence, the behaviour of VAWTs under the influence of atmospheric turbulence still remains an area to be explored. Extensive research in this area would tremendously help in developing VAWTs for offshore and urban applications.

3

METHODS

3.1. VERTICAL AXIS WIND TURBINE (VAWT) MODEL

The VAWT model used for this study is a two dimensional model of the modified DeepWind rotor that has been taken from Galinos (2015). As mentioned earlier, the original DeepWind rotor was designed by Verelst *et al.* (2014). The modified DeepWind rotor was designed by changing the stiffness of the blades and the tower. This was done to reduce the large blade edgewise deflections at the equator. The equator of the turbine in this case was defined as the height with the maximum diameter of the turbine by the author. The hub height was taken by the author as the height at which a horizontal line divides the rotor swept area in to two halves. The stiffness of the blades was increased by increasing the distance between the shear webs in the blades and moving them closer to the edges. Four shear webs were also added close to the edges to achieve the desired stiffness. Furthermore, the tip speed ratio of the turbine has been taken as 4 for this study since a value lesser than this would be very low and would not be optimal for the simulation of the turbine. The specifications of the modified DeepWind rotor are as follows:

Table 3.1: Operational and geometric data for the turbine used (Galinos, 2015).

Property	Value	
Rated electrical power	5	[MW]
Rated rotational speed	5.95	[rpm]
	0.62	[rad/s]
Rated wind speed	13.5	[m/s]
Rated tip speed	37.5	[m/s]
Hub height	90	[m]
Cut-in wind speed	4	[m/s]
Cut-out wind speed	25	[m/s]
Number of blades,N	2	[-]
Rotor Diameter, D	121	[m]
Rotor height to diameter ratio	1.18	[-]
Blade chord, c_a	5	[m]
Solidity, $\sigma = \frac{Nc_a}{R}$	0.165	[-]
Swept area	11996	[m^2]
Rotor inertia on LSS	184.2x10^6	[kg m^2]
Generator inertia on HSS	534	[kg m^2]
Gearbox ratio	87:1	[-]
Rotor mass	615800	[kg]
Blade mass	52400	[kg]
Total height	170	[m]
Rotor height	143	[m]

The 2D model used in this study can be seen in figure 3.1. This figure shows the top view of the turbine. The plane of rotation of the turbine is horizontal. The turbine rotates in clockwise direction and the incoming wind comes from left side of the turbine. The two blades can be seen as the airfoils on the circumference of the turbine. Hence the terms blades and airfoils have used interchangeably for most of this study. The co-ordinate axes can be seen at the centre of the turbine. This coordinate system has been followed throughout this study and in this report. The azimuthal angle (θ) is defined in the direction of rotation of the turbine which is clockwise in this study. The lower blade in the diagram is referred as 'Blade 1' and the upper blade is referred as 'Blade 2'. The quarter chord point of the Blade 1 is kept at zero degrees azimuthal angle at the start of every simulation. All the forces and the moments due to wind were measured at the quarter chord point of each airfoil. This turbine was simulated using the aeroelastic code 'Unsteady Two-Dimensional Vorticity Aerodynamics (U2DiVA)' which has been discussed further in section 3.5. From this point onwards in this report, the term 'turbine' will refer to the 5 MW modified DeepWind VAWT.

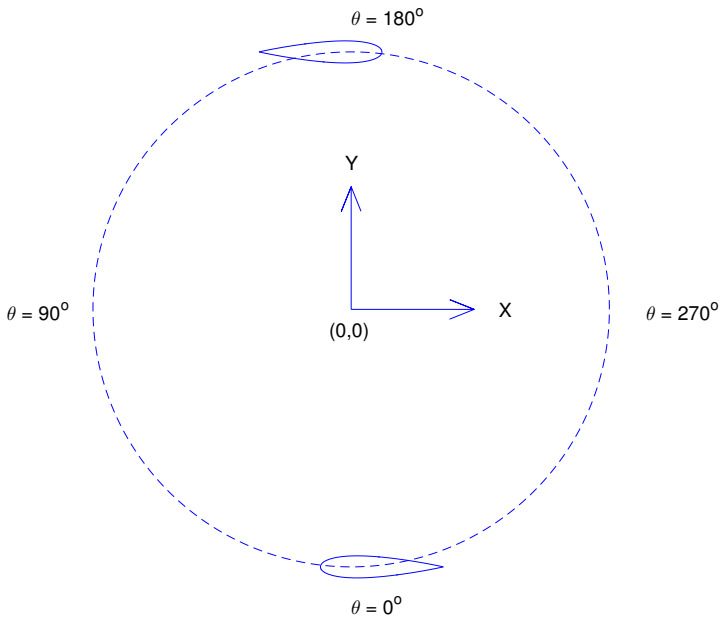

Figure 3.1: Schematic of the 2D VAWT

3.2. COORDINATE SYSTEM

As mentioned in previous section, the coordinate system followed throughout this study and in this report has been defined in figure 3.1. The centre of the turbine is the origin of this coordinate system. The direction of incoming wind field to the turbine is along the x-axis. Therefore the term 'Streamwise direction' refers to the direction of positive x-axis. The horizontal direction is also considered along the x-axis while the lateral direction is considered along the y-axis. The term 'Cross-streamwise direction' hence refers to the direction of y-axis. The z-axis in this coordinate system points out of the page and the vertical direction is considered along this axis. The wind velocities in the horizontal, lateral and vertical directions are denoted by the letters 'U', 'V' and 'W' respectively.

3.3. ABOUT THE STANDARD

The 'IEC 61400-1' standard defines a number of relevant external conditions and design situations for wind turbines. The latest version of the standard which was published in 2005 is widely used and hence, has been used in this study as well. The guidelines established by the standard are defined for wind turbines in general

but the standard seems more suitable and tailored for the Horizontal Axis Wind Turbines (HAWTs). During their lifetime, wind turbines are subjected to various environmental and external conditions. The changes in these conditions affect the loading, durability and operation of the turbines. The environmental, electrical and soil parameters should be considered so that proper reliability and safety is ensured. The environmental conditions consist of the wind conditions and other environmental conditions. The conditions that affect the electrical power network are the electrical conditions and the conditions that affect the design of the foundation of the turbine are the soil conditions. External conditions can be further divided into normal and extreme conditions. While the normal conditions occur repeatedly during the lifetime of the wind turbine, the extreme conditions occur very rarely on the other hand. Wind conditions are primary conditions which affect the structural integrity of the turbine. The Design Load Cases (DLCs) are a combination external conditions and the operation modes of wind turbine and are potentially critical. The normal and extreme conditions for the wind turbines are defined by the classes of the wind turbine (International Electrotechnical Commission, 2005).

On the basis of the location where the wind turbines have to be installed, they are divided into three classes. Wind speed and turbulence parameters are used to define these classes. The reference turbulence intensity, which is the expected value of turbulence intensity at a wind speed of 15 m/s is also defined in the standard and is used for calculation of turbulence intensity at other wind speeds depending on the turbulence model used. The following table defines the parameters that are used to define the wind models for the simulation of a wind turbine at a particular location:

Table 3.2: Basic parameters for wind turbine classes (International Electrotechnical Commission, 2005)

Wind turbine class		**I**	**II**	**III**
V_{ref}	(m/s)	50	42.5	37.5
V_{ave}	(m/s)	10	8.5	7.5
A	I_{ref} (-)		0.16	
B	I_{ref} (-)		0.14	
C	I_{ref} (-)		0.12	

The description of the symbols in the table 3.1 is as follows:

- V_{ref} is the reference wind speed average over a time period of 10 minutes.
- V_{ave} is the mean wind over a time period of 10 minutes and equals to $0.2V_{ref}$.
- A defines the category for higher turbulence characteristics.
- B defines the category for medium turbulence characteristics.
- C defines the category for lower turbulence characteristics.
- I_{ref} is the expected value of turbulence intensity at 15m/s.

As per the standard, the values specified in the table above are applied at the hub height of the turbine. The location of the VAWT used in this study is offshore and hence the turbine class '1C' has been used here as specified in Veldkamp (2016). The Normal Turbulence Model (NTM) has been used in this study to simulate the turbulent wind on the turbine. The wind fields required for the simulation of the turbine were generated using the turbulence simulator 'TurbSim'. This simulator has been discussed in detail in section 3.6. The term 'Standard' or 'IEC 61400-1' will hereby refer to the 3rd edition of the standard IEC 61400-1.

3.4. SITE CONDITIONS FOR THE TURBINE

The site chosen for the simulation of the turbine was the location of the Offshore Wind Farm Egmond aan Zee (OWEZ) project. This site is located 18 kms offshore from the coast of Egmond aan Zee, the Netherlands (52^{o}36'22.9"N 4^{o}23'22.7"E).

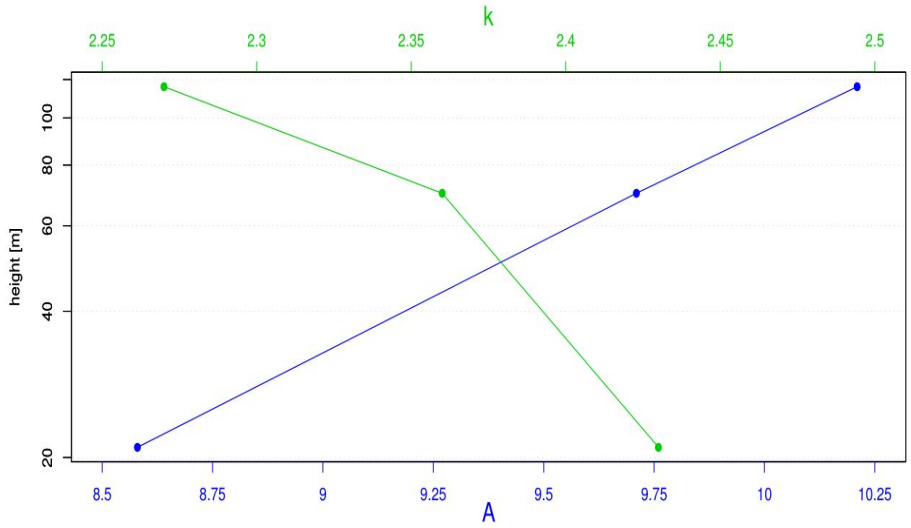

Figure 3.2: Weibull scale (A) and shape (k) parameters variation with height (Barth and Eecen, 2006).

The measurement and evaluation of the wind characteristics of the site was carried out by NoordzeeWind. The data for the characterization of wind, waves and currents was measured using a meteorological mast (metmast) of 116 m height. The metmast was a lattice tower and had three booms at heights 21 m, 70 m and 116 m above Mean Sea Level (MSL). The data was measured from June 2005 to December 2006. The wind speed frequency distribution was found out from the wind speed data measurement at three heights and a Weibull distribution was fitted on the calculated frequency distribution at each heights. Based on these fits, the scale and shape parameters of the Weibull distribution for each height were found out. Figure 3.2 shows the variation of shape and scale parameters of Weibull distribution (Barth and Eecen, 2006). Based on the values of scale and shape parameters at different heights, the values of scale and shape parameters were calculated at the hub height (90 m) of the turbine by interpolation. The scale parameter for the hub height of the turbine was found to be 9.93 while the shape parameter was found to be 2.32. The average wind speed was found to be 8.79 m/s according to the Weibull distribution found out from the shape and scale parameters for the hub height of the turbine. The wind speed frequency distribution calculated from the scale and shape parameters at the hub height can be seen in figure 3.3 and the Cumulative Density Function (CDF) for this wind speed frequency distribution can be seen in figure 3.4 . The average wind speed has also been mentioned in the figure.

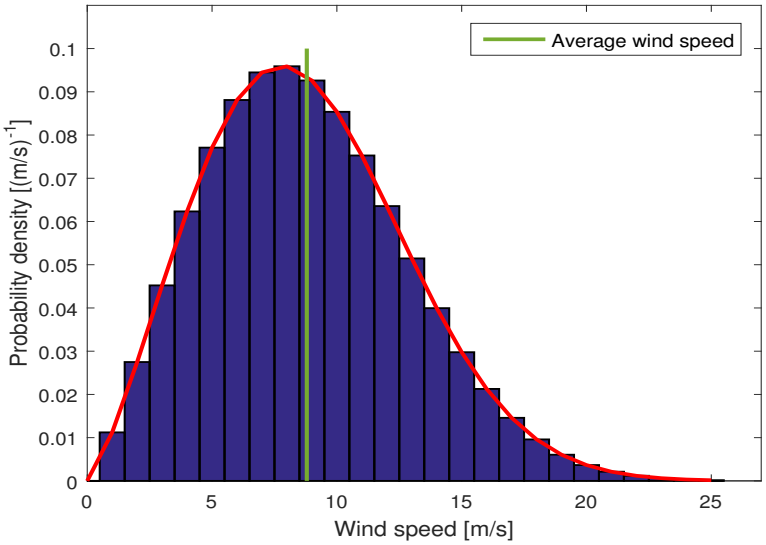

Figure 3.3: Wind speed frequency distribution for hub height.

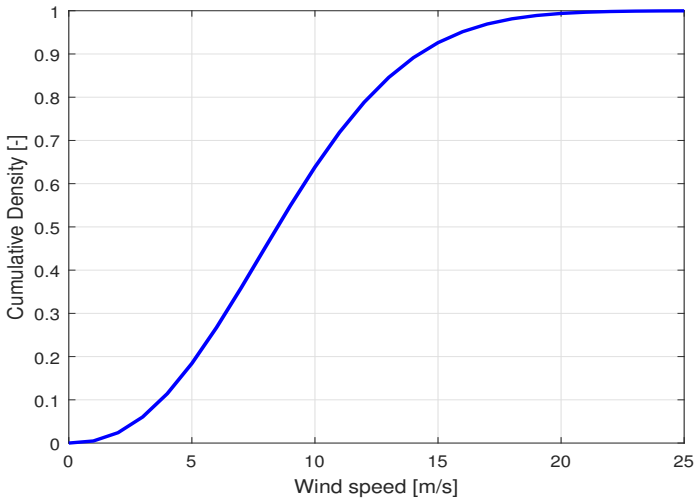

Figure 3.4: Cumulative density distribution for the wind speed frequency distribution at hub height.

3.5. U2DiVA

The Unsteady Two-Dimensional Vorticity Aerodynamics (U2DiVA) model is a numerical model developed by Ferreira (2009) to analyze the wake behaviour of 2D VAWTs. It is a 2D unsteady multibody free-wake panel-code which has been formulated on the basis of the methods defined in Katz and Plotkin (2000). Using a distribution of constant strenght sources and doublets, the bodies are modelled by this code. Constant strength doublet panels are used to model the near wake of the turbine while vortex points are used to model the far wake (Ferreira *et al.*, 2014). This model has been developed in the programming language 'MATLAB'. The outputs given by the model are the time series of forces in the streamwise and cross-stream directions, and moment around a specified point. These series are normalized by dynamic pressure $\frac{1}{2}\rho {U_{ref}}^2$ where ρ is the density of air and U_{ref} is the reference velocity. The value of the reference velocity in this case is 1 m/s. The rotor and wake plot of the turbine can be seen in figure 3.5.

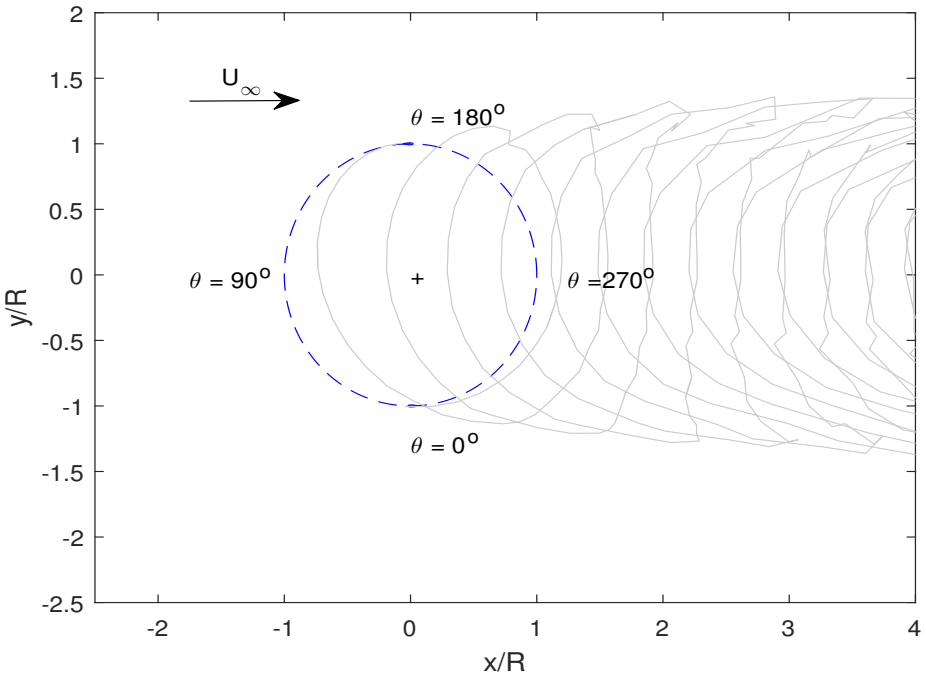

Figure 3.5: Plot of rotor and wake simulated using U2DiVA

3.6. TURBSIM

TurbSim is a stochastic, full-field, turbulent wind field simulator. It generates wind fields using a statistical model as opposed to a physics-based model. A time series of three component velocity vectors is generated at the points of a two-dimensional vertical rectangular grid by TurbSim (figure 3.6). The generated flow field contains coherent turbulence structures. Proper spatiotemporal turbulent velocity field relationships are reflected by these turbulence structures. These relationships are seen in the instabilities that are associated with nocturnal boundry layer flows. Also, these relationships are not well represnted by IEC Normal Turbulence Models (NTM) (Jonkman and Kelly, 2016).

Turbulent wind fields generated by TurbSim are based on Taylor's frozen turbulence hypothesis. Several different sets of output files are generated by TurbSim. The full-field turbulent wind can be generated in three output formats namely, TurbSim/AeroDyn, BLADED/AeroDyn and formatted (readable) formats. The TurbSim/AeroDyn and BLADED/AeroDyn formats have the extension .bts and .wnd respectively while the formatted format leads to generation of three output files with extensions .u, .v, and .w. The extensions .u, .v, and .w represent the velocities in horizontal, lateral and vertical directions respectively.

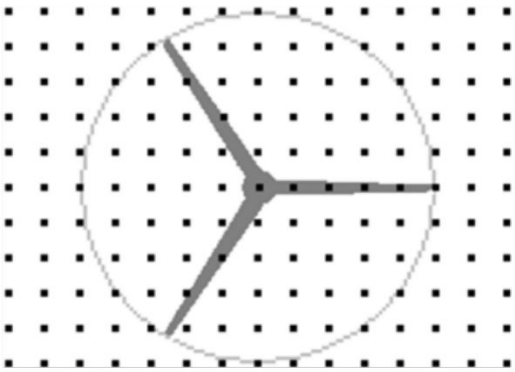

Figure 3.6: Rectangular grid for turbulent field generation (Jonkman, 2009)

For this study, the flow field files were generated in .wnd format. The wind data from these files was extracted using MATLAB programs and was then stored in .mat format. TurbSim generates turbulent wind fields only for HAWTs (Jonkman, 2009).

Since the turbine used for simulation in this study is two-dimensional, the wind velocity time series at the grid line along the lateral direction at hub height was extracted from the two-dimensional time series generated by TurbSim. The extracted time series was therefore a one-dimensional time series. This one-dimensional time series was extracted using a program developed in MATLAB. From the extracted time series, only the horizontal and lateral components of velocity were used for the simulation since the turbine used in this study is a two-dimensional turbine rotating in a horizontal plane. Six different seeds were used to generate turbulent wind fields at each wind speed (at an interval of 1 m/s) between the cut-in and cut-out wind speeds of the turbine. The turbulent wind fields used in this study are discussed further in chapter 4.

3.7. DEVELOPMENT OF TOOLS

For post processing of the results from U2DiVA and calculation of change in equivalent loads, a rainflow counting program and a post processor were developed in MATLAB.

3.7.1. RAINFLOW COUNTING PROGRAM

The rainflow counting program was developed using 'Rainflow Algorithm I' as mentioned in Downing and Socie (1982). In this algorithm, first the peaks and the valleys of the input time series are identified and stored as a sequence. Once the peaks and valleys are identified, the sequence is rearranged in such a way that it begins and ends with either the maximum peak or the minimum valley and the counting is done subsequently. For the rainflow counting program developed in this study, the sequence of peaks and valleys is rearranged to start and end at the maximum peak. The output of this program is a series of ranges and their corresponding means.

3.7.2. POST PROCESSOR

The post processor developed in this study takes the array of inverse slopes and the type of turbulence model for which the equivalent loads are to be calculated as input. The outputs are the changes in equivalent load for streamwise, radial, and tangential forces, and moment around the aerodynamic centre of the airfoil. The following steps are followed by it to calculate the outputs:

1. The time series of tangential and radial forces on each blade from the streamwise and cross-stream forces for each seed at a particular wind speed are calculated.

2. The results from the previous step are then stacked in a single time series of tangential force, radial force, streamwise force and moment for each blade.

3. The rainflow counting program is then used to calculate the relevant ranges of the streamwise force, tangential force, radial force, and the moment.

4. The ranges for each force and the moment are then binned in different bins.

5. The upper limit of the each bin powered by the inverse slope is multiplied by the number of counts in the corresponding bin.

6. The obtained values from the previous step are then summed up together and multiplied by the probability of occurrence of the wind speed for which the calculations are done.

7. This procedure is repeated for each wind speed bin and then the sums obtained for each wind speed are added together.

The above mentioned steps are followed for the results obtained from simulations of the turbulent model on the turbine and simulations without turbulence. The equivalent loads obtained from both simulations are then compared by calculating the changes in equivalent loads under the influence of turbulence with respect to equivalent loads under the influence of wind without turbulence. The theoretical aspects of the post processor have been discussed in detail in chapter 4.

For the verification of accuracy of the results of the rainflow counting program and the post processor, three time series of forces and moments on one of the blades and two time series of forces and moments on the hub of a demo HAWT specified in the aeroelastic code GH Bladed were processed in both, GH Bladed and the post processor. The time series on the blade which were processed included the edgewise shear force, the flapwise bending moment, and the moment in streamwise direction while for hub, the time series processed were the force in streamwise direction and the moment in vertical direction. Rainflow counting and calculation of equivalent loads for each time series was done for the verification. GH Bladed uses 'Rainflow Algorithm I' from Downing and Socie (1982) as well for the rainflow counting. The equivalent loads are calculated on the basis of following equation:

$$F_{eq} = \left(\frac{\sum_i n_i S_i^m}{Tf} \right)^{\frac{1}{m}} \tag{3.1}$$

where F_{eq} is the equivalent load, n_i is the number of cycles in load range S_i, T is the duration of the time series and f is the constant frequency of the sinusoidal load F_{eq} (Garrad Hassan and Partners Limited, 2014). The frequency of the sinusoidal load was taken as 1 Hz for the verification.

The results of rainflow counting using both GH Bladed and post processor for the forces and moments on the blade and the hub can be seen in figures 3.7, 3.8, 3.9, 3.10, and 3.11 .

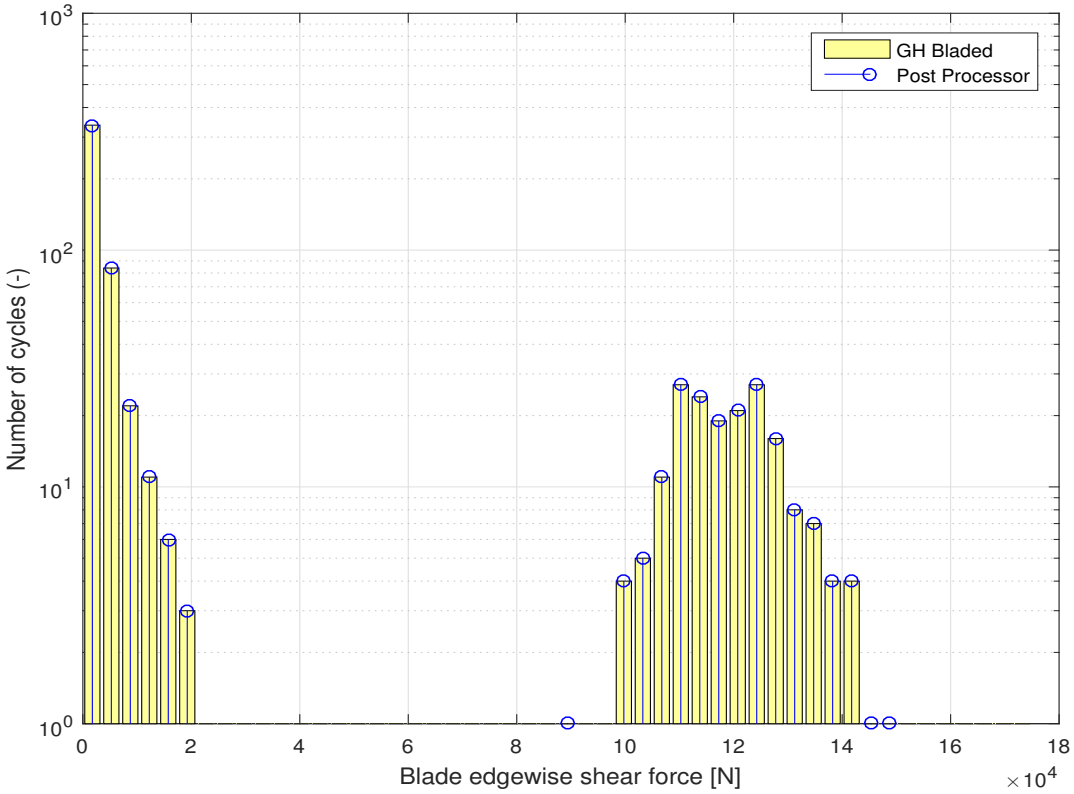

Figure 3.7: Bin count of edgewise shear force on blade

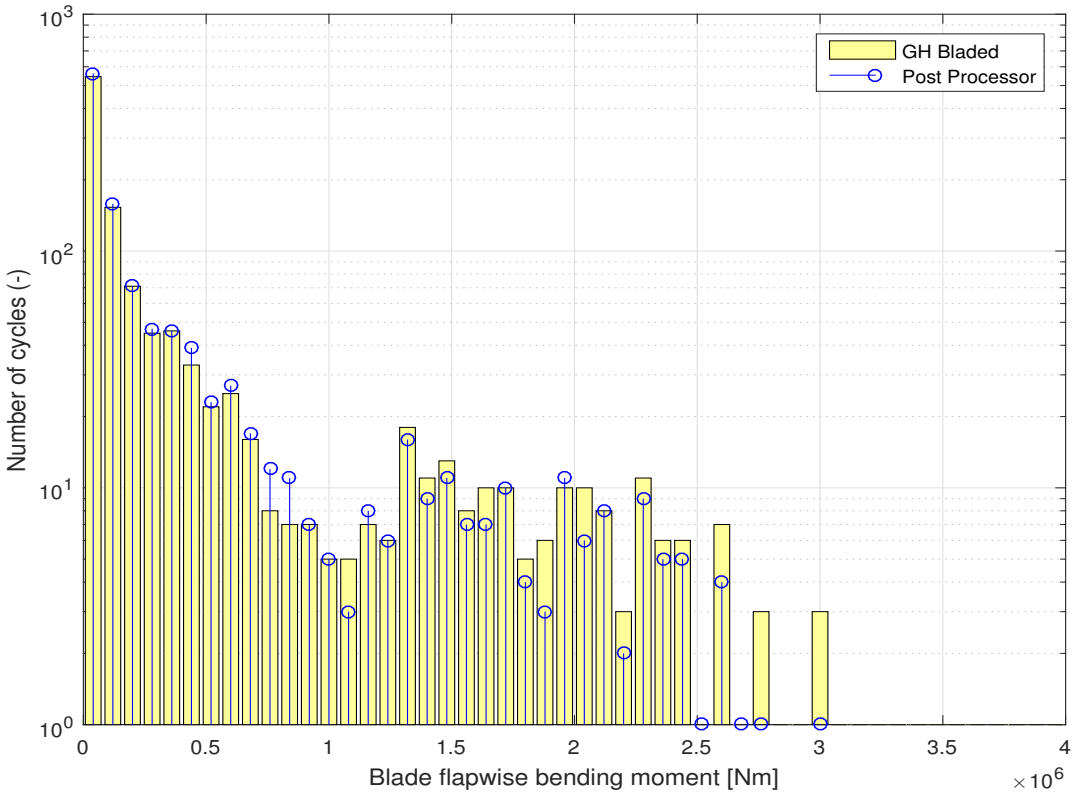

Figure 3.8: Bin count of flapwise bending moment on blade

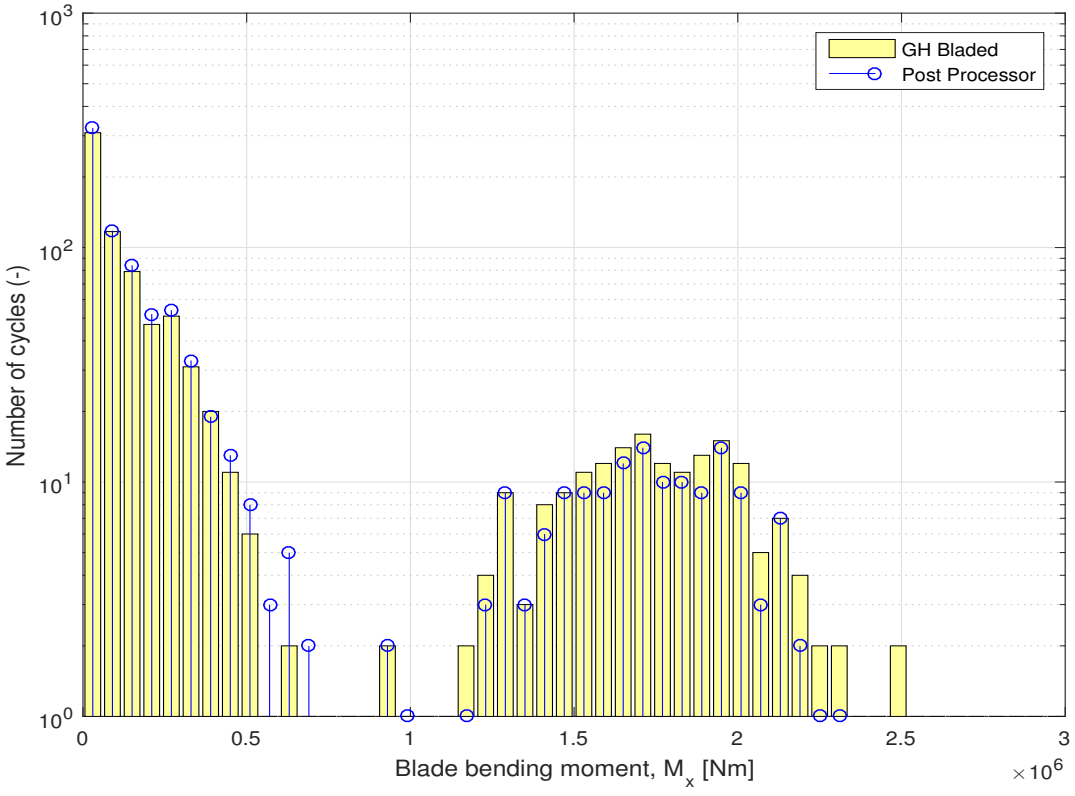

Figure 3.9: Bin count of bending moment in streamwise direction on blade

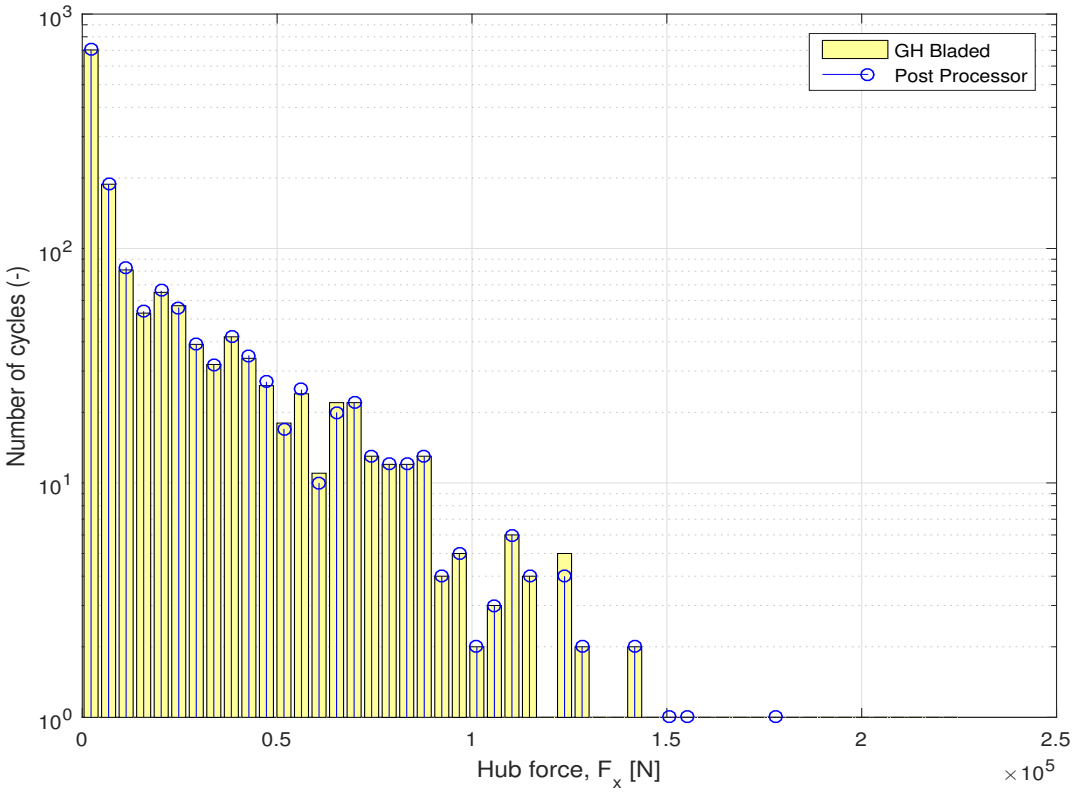

Figure 3.10: Bin count of force in streamwise direction on hub

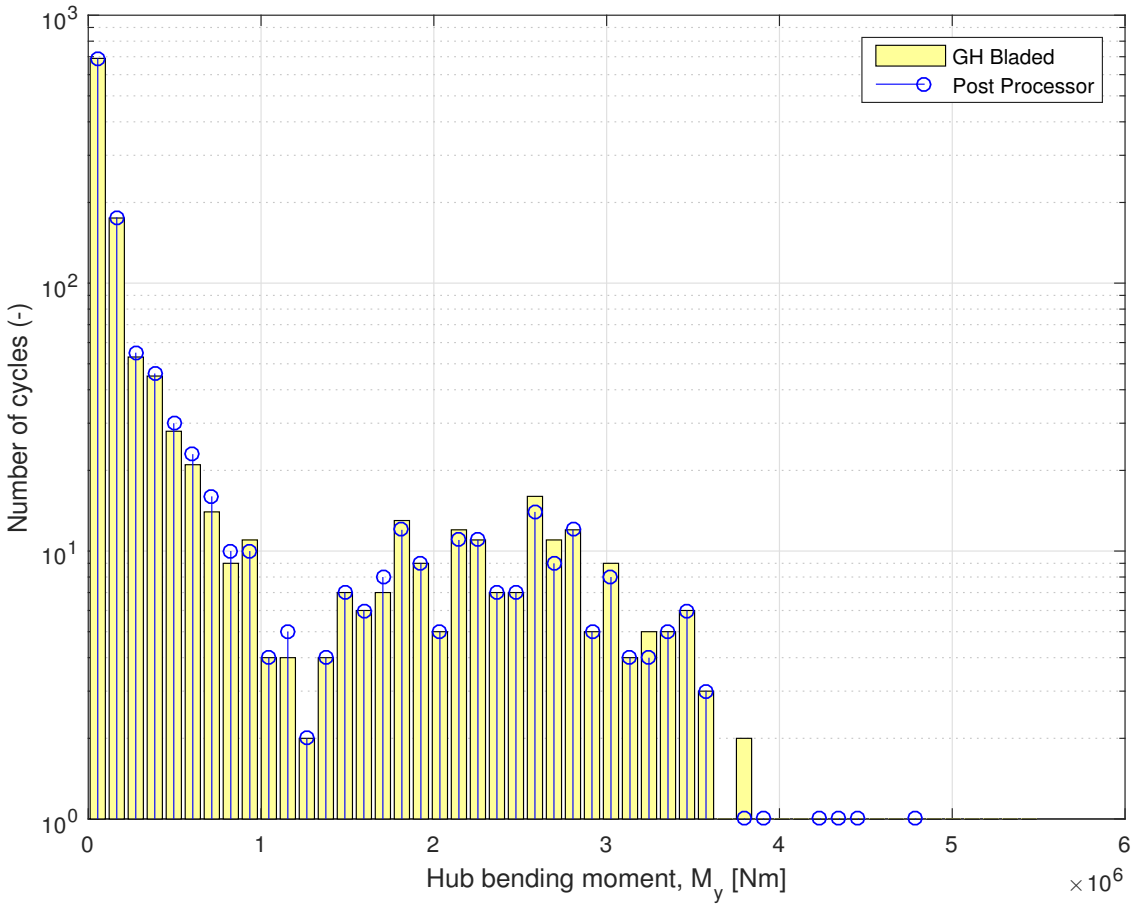

Figure 3.11: Bin count of moment in vertical direction on hub

It can be observed from the above figures that the results obtained from both, GH bladed and rainflow counting program developed in this study show similar results for the demo HAWT. In most of the cases it can be seen that the results obtained from both the programs in general are similar and in some cases exact. Hence it can be concluded that the rainflow counting program developed in this study is accurate enough to be used further in this study and in the future research.

The results of the calculation of equivalent loads from GH Bladed and post processor can be seen in tables 3.3, 3.4,3.5, 3.6, and 3.7. The difference between the values has been calculated with respect to the equivalent loads obtained from GH Bladed.

Table 3.3: Calculated equivalent edgewise shear forces for the blade and the difference between them

Inverse Slope	Bladed [kN]	Post processor [kN]	Difference [%]
3	81.54	80.37	1.46
4	90.44	89.16	1.44
5	96.38	95.02	1.43
6	100.67	99.26	1.42
7	103.96	102.51	1.41
8	106.58	105.11	1.40
9	108.75	107.26	1.39
10	110.59	109.09	1.38
11	112.19	110.68	1.37
12	113.60	112.08	1.36

Table 3.4: Calculated equivalent flapwise bending moments for the blade and the difference between them

Inverse Slope	Bladed [MNm]	Post processor [MNm]	Difference [%]
3	1.32	1.19	9.56
4	1.51	1.37	9.39
5	1.66	1.49	9.52
6	1.78	1.61	9.87
7	1.89	1.69	10.39
8	1.99	1.78	10.99
9	2.08	1.84	11.60
10	2.17	1.90	12.23
11	2.24	1.95	12.83
12	2.31	2.00	13.34

Table 3.5: Calculated equivalent moments on blade (M_x) and the difference between them

Inverse Slope	Bladed [MNm]	Post processor [MNm]	Difference [%]
3	1.20	1.11	7.58
4	1.34	1.26	6.29
5	1.44	1.36	5.60
6	1.52	1.44	5.17
7	1.58	1.51	4.99
8	1.64	1.56	4.88
9	1.68	1.59	4.92
10	1.72	1.63	4.99
11	1.76	1.67	5.15
12	1.79	1.69	5.30

Table 3.6: Calculated equivalent forces on hub (F_x)and the difference between them

Inverse Slope	Bladed [kN]	Post processor [kN]	Difference [%]
3	60.27	59.94	0.55
4	68.84	67.47	1.98
5	76.97	74.47	3.24
6	84.64	80.94	4.38
7	91.82	86.90	5.36
8	98.49	92.38	6.21
9	104.64	97.41	6.91
10	110.27	102.02	7.49
11	115.42	106.23	7.96
12	120.12	110.09	8.35

Table 3.7: Calculated equivalent moments on hub (M_z) and the difference between them

Inverse Slope	**Bladed [MNm]**	**Post processor [MNm]**	**Difference [%]**
3	1.81	1.76	2.35
4	2.07	2.02	2.33
5	2.27	2.22	2.38
6	2.45	2.39	2.52
7	2.60	2.53	2.71
8	2.74	2.66	2.89
9	2.87	2.78	3.06
10	2.98	2.89	3.20
11	3.09	2.99	3.30
12	3.18	3.08	3.40

The difference in results range from 0.55% to 13.34% with an average of 5.19%. It can be observed that the bigger differences in equivalent loads were obtained in cases where the results of the rainlow counting from both programs were not exactly the same. Therefore an average difference of around 5% can be considered reasonable. This makes the post processor suitable for further use in this study and in future research as well.

4

SIMULATION OF LOAD CASES AND POST PROCESSING

4.1. TURBULENCE MODEL

The Normal Turbulence Model (NTM) wind specified in the standard was used to simulate turbulence on the turbine. This model represents the conditions under which the turbine produces power during most of its lifetime. The longitudinal turbulence standard deviation (σ_1) corresponding to this model is defined by equation 4.1, where I_{ref} refers to the expected value of turbulence intensity at the wind speed of 15 m/s and V_{hub} is the wind speed at hub height of the turbine.

$$\sigma_1 = I_{ref}(0.75V_{hub} + 5.6) \tag{4.1}$$

The longitudinal turbulence intensity (TI) is defined by following equation:

$$TI_1 = \frac{\sigma_1}{V_{hub}} \tag{4.2}$$

The vertical wind shear for this model is defined by power law (equation 4.3).

$$V(z) = V_{hub}\left(\frac{z}{z_{hub}}\right)^{0.2} \tag{4.3}$$

where z is the height at which wind velocity needs to be calculated.

From this point, the terms 'Turbulence Standard Deviation' and 'Turbulence Intensity' will refer to longitudinal turbulence standard deviation (σ_1) and longitudinal turbulence intensity (TI_1) respectively in this report.

Since the turbine simulated in this study is a two-dimensional turbine in a horizontal plane located at the hub height of the original turbine, the variable z in equation 4.2 is equal to 'z_{hub}'. This shows that vertical wind shear cannot be applied in this study and the value of wind speed is always equal to the wind speed at hub height.

As mentioned earlier in table 3.2, the value of I_{ref} is selected according to wind turbine class and the category of turbulence and accordingly, the wind turbine class '1C' has been chosen for study. The variation of turbulence standard deviation and turbulence intensity with wind speed for all three categories of turbulence can be seen in figures 4.1 and 4.2 respectively.

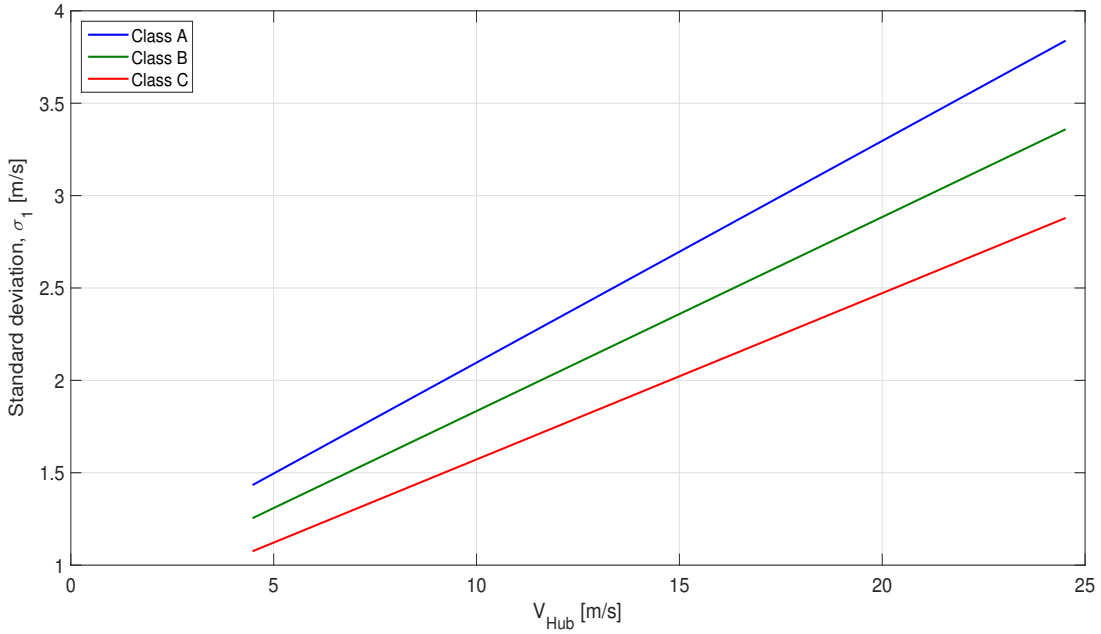

Figure 4.1: Variation of turbulence standard deviation with wind speed

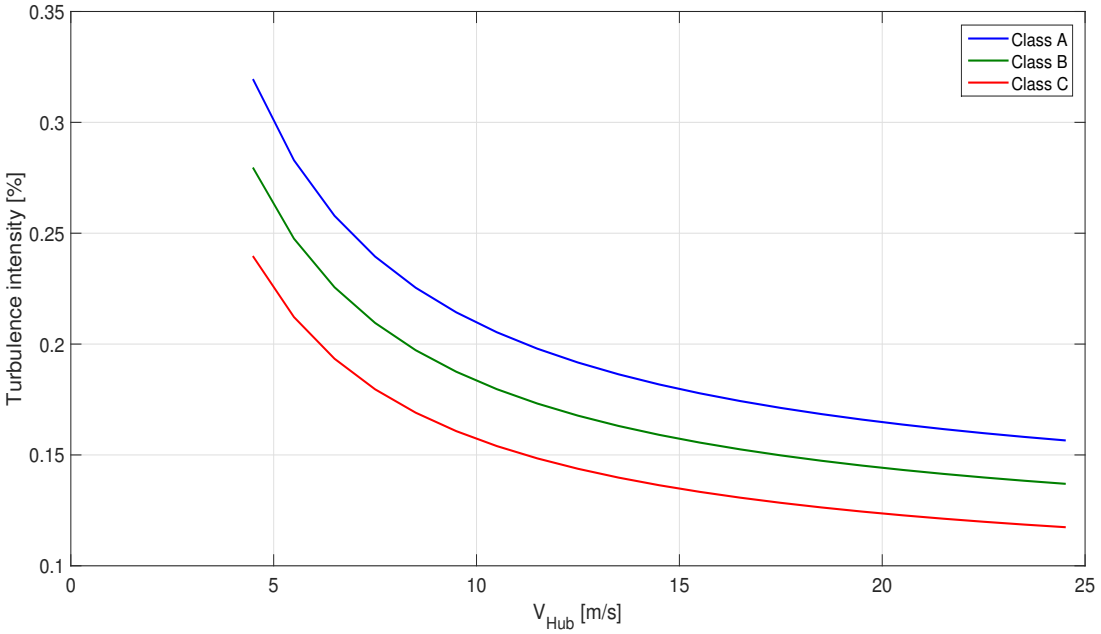

Figure 4.2: Variation of turbulence intensity with wind speed

The fatigue analysis during power production has been done in this study. This corresponds to the Design Load Case (DLC) 1.2 as specified in the standard. For this case, the simulations should be done between cut-in wind speed and cut-out wind speeds in various wind speed bins. As mentioned earlier in chapter 3, the wind speed bins used in this study had a bin width of 1 m/s with representative speed for each bin at the center of each bin. The wind speed bins and their representative wind speeds can be seen in table 4.1.

Table 4.1: Wind speed bins and their representative wind speeds

Wind speed bin [m/s]	Representative wind speed [m/s]
4-5	4.5
5-6	5.5
6-7	6.5
7-8	7.5
8-9	8.5
9-10	9.5
10-11	10.5
11-12	11.5
12-13	12.5
13-14	13.5
14-15	14.5
15-16	15.5
16-17	16.5
17-18	17.5
18-19	18.5
19-20	19.5
20-21	20.5
21-22	21.5
22-23	22.5
23-24	23.5
24-25	24.5

4.2. GENERATED TURBULENCE MODELS

The turbulence models for the simulations were generated in the simulator 'TurbSim' as mentioned earlier in chapter 3. Six different seeds were used to generate the NTM wind fields. Each seed leads to generation of a wind field with turbulence intensity slightly greater or lesser than the expected value at that wind speed. The duration of wind velocity time series of the turbulent wind fields was 600 seconds and the time step used was 0.05 seconds. A one-dimensional time series was extracted from the two-dimensional wind velocity time series generated by TurbSim. A sample turbulent wind field is shown in figure 4.3.

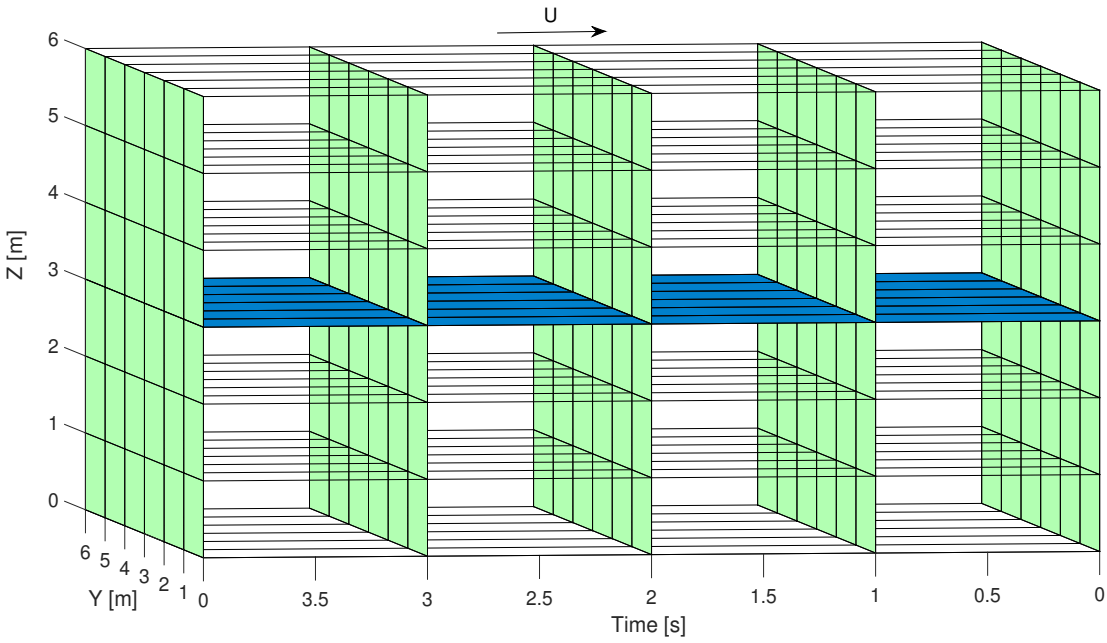

Figure 4.3: Sample turbulenct wind field

Each vertical (green) grid represents the wind field at the rotor of a HAWT at the corresponding time. Each point in the grid has wind velocity components in horizontal, lateral and vertical directions. The blue horizontal grid represents the extracted wind field and lies at the hub height of the HAWT. The extracted wind field represents a one-dimensional time series. Only the horizontal and lateral components of velocities in the horizontal grid were used for the simulations.

The Kaimal spectrum and exponential coherence model (as specified in the standard) was used to generate the wind fields. The turbulence intensity used for this model is defined by equation 4.1 while the longitudinal turbulence scale parameter is defined as follows:

$$\Lambda_1 = \begin{cases} 0.7z, & z \leq 60m \\ 42m, & z > 60m \end{cases} \tag{4.4}$$

The variation of averaged longitudinal and lateral turbulence standard deviations for the six seeds with velocity can be seen in figures 4.4 and 4.6. The variation of standard deviations with velocity for turbulence class 'C' has also been shown in both of the figures to compare both the values. A similar comparison has been made in figures 4.5 and 4.7 for the longitudinal and lateral turbulence intensities of the generated wind fields.

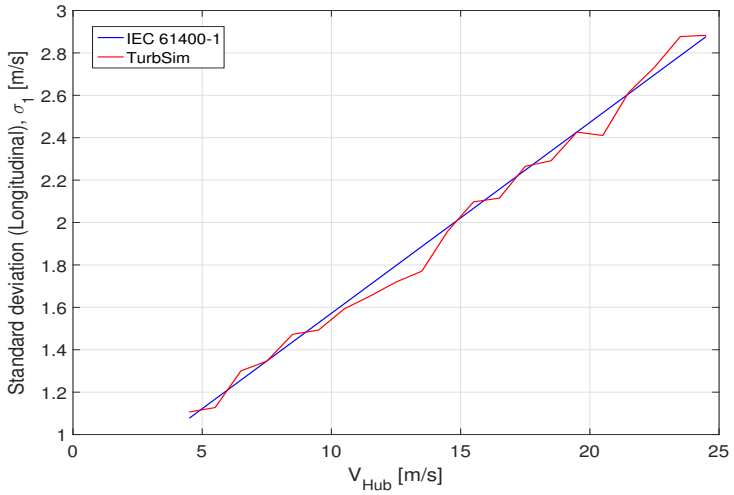

Figure 4.4: Variation of averaged longitudinal turbulence standard deviations (in x-direction) of the generated wind fields with wind speed at hub height

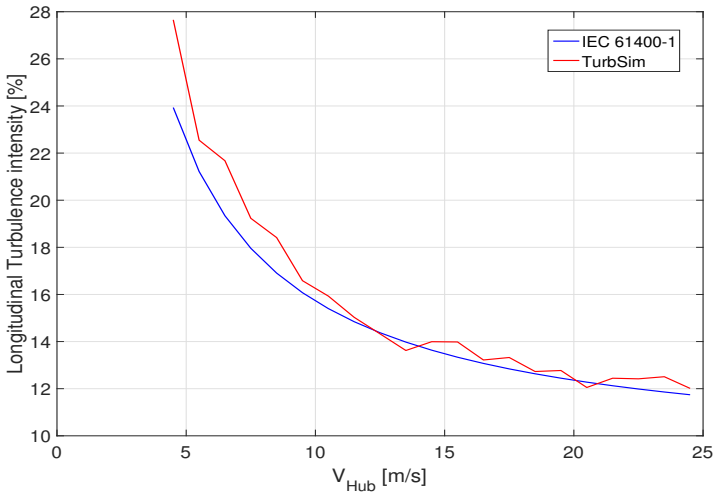

Figure 4.5: Variation of averaged longitudinal turbulence intensity (in x-direction) of the generated wind fields with wind speed at hub height

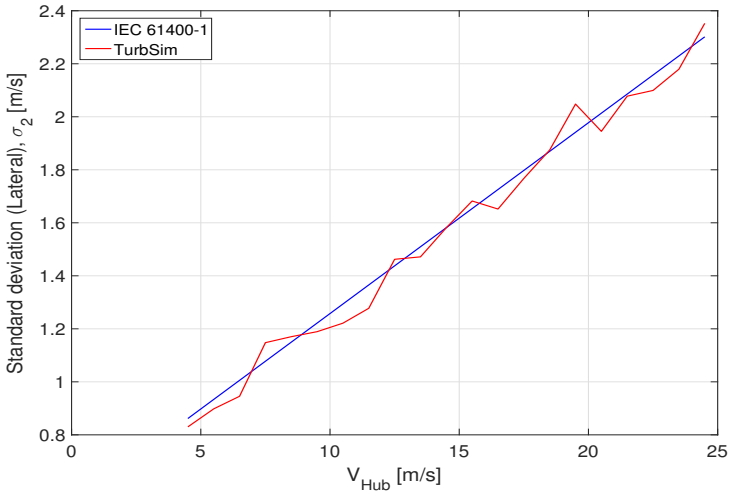

Figure 4.6: Variation of averaged lateral turbulence standard deviations (in x-direction) of the generated wind fields with wind speed at hub height

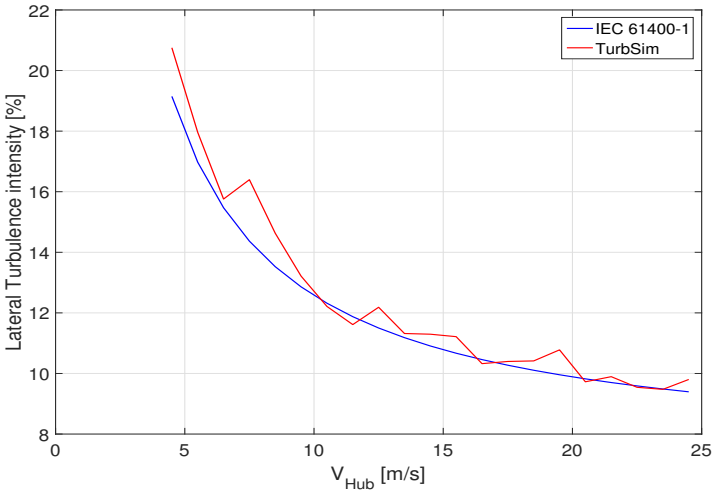

Figure 4.7: Variation of averaged lateral turbulence intensity (in x-direction) of the generated wind fields with wind speed at hub height

From the above figures, it can be observed that both, the average turbulence standard deviation and the average turbulence intensity both directions at each wind speed is not exactly the same as expected according to the standard. This is due to averaging of the values for only six seeds. For a very high number of seeds (≥ 100), the average values are highly likely to be the same as expected according to the standard.

A 19×19 vertical grid was generated for the all the turbulent wind fields. Each point in this grid had an individual wind velocity time series. The grid points in the lateral direction at the centre of this grid were located at the hub height of the turbine. These grid points can be seen in figure 4.8 (represented by red, white, green and black stars). U_∞ is the streamwise wind velocity in this figure. The time series at these grid points were used for the simulations. The height and the width of the grid were both equal to the diameter of the turbine.

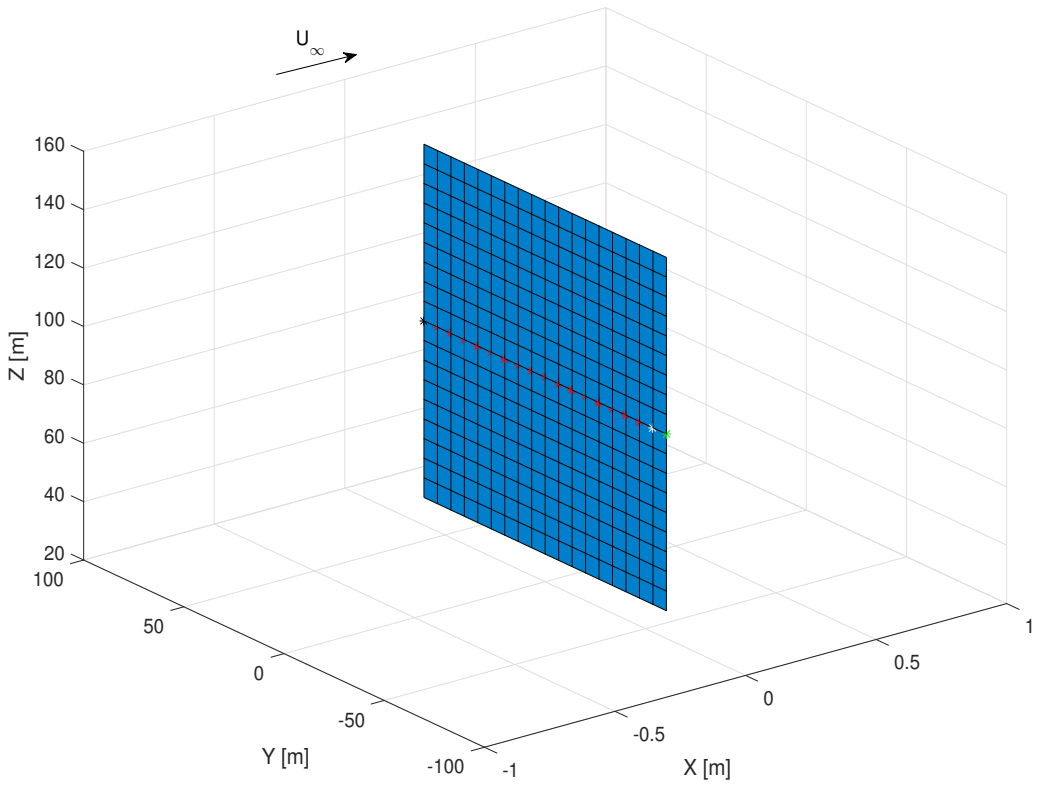

Figure 4.8: Generated grid for the turbulent wind field and the grid points in the lateral direction at the hub height

The time duration of the generated wind fields was slightly greater than the specified time duration. Hence the first few seconds of the time series were not used for the simulations so that the total time duration of each simulation remains 600 seconds.

The average velocity of the generated wind fields in both horizontal ($\bar{u}$) and lateral ($\bar{v}$) directions was 0 m/s. Hence the wind speed in the streamwise direction (U_∞) was added to the components of velocity in the horizontal direction (u) in the wind field so that it represents the movement of wind field in streamwise direction. This can be described as follows:

$$\bar{u} = \bar{v} = 0 \tag{4.5}$$

$$U_i = U_\infty + u_i \tag{4.6}$$

where u_i is the component of wind velocity in the streamwise direction at the i_{th} point in the grid of the generated wind field

The time series of the horizontal component of wind velocity at three different grid points in the turbulent wind fields generated at wind speed 4.5 m/s, 13.5 m/s and 24.5 m/s can be seen in figures 4.9, 4.10 and 4.11 respectively. The seed used for generation of each of these wind fields is different. Points 1 and 2 lie next to each other in the grid shown in figure 4.8 (represented by green and white stars respectively) while Point 3 (represented by black star) lies far away from points 1 and 2. The time series of the lateral component of wind velocity for the same points can be seen in figures 4.12, 4.13 and 4.14. More information on these time series can be found in Appendix B.

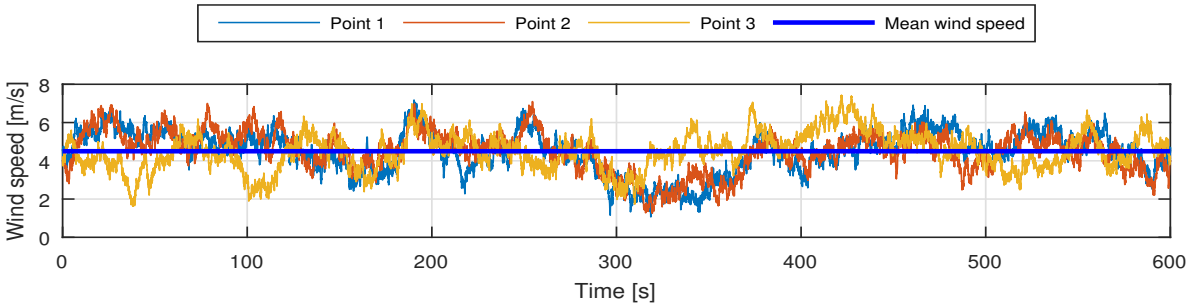

Figure 4.9: Time series of horizontal component of velocity for three points in the turbulent wind field generated at a wind speed of 4.5 m/s.

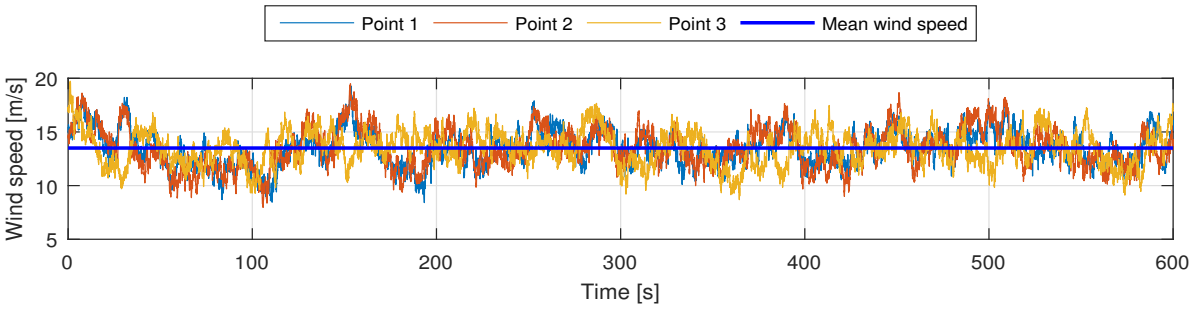

Figure 4.10: Time series of horizontal component of velocity for three points in the turbulent wind field generated at a wind speed of 13.5 m/s.

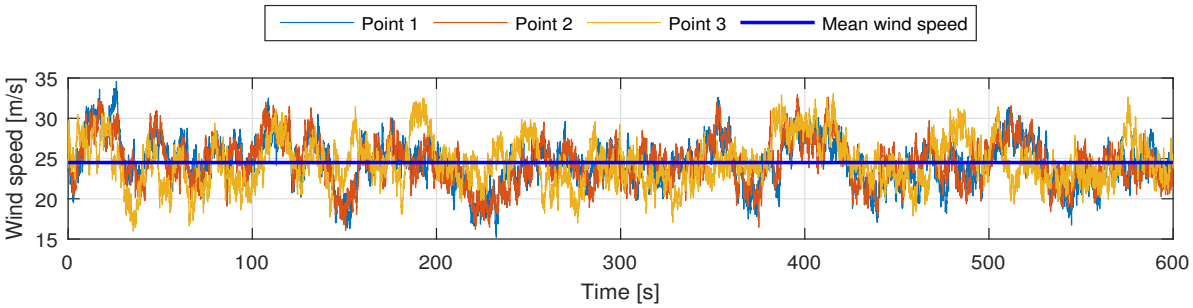

Figure 4.11: Time series of horizontal component of velocity for three points in the turbulent wind field generated at a wind speed of 24.5 m/s.

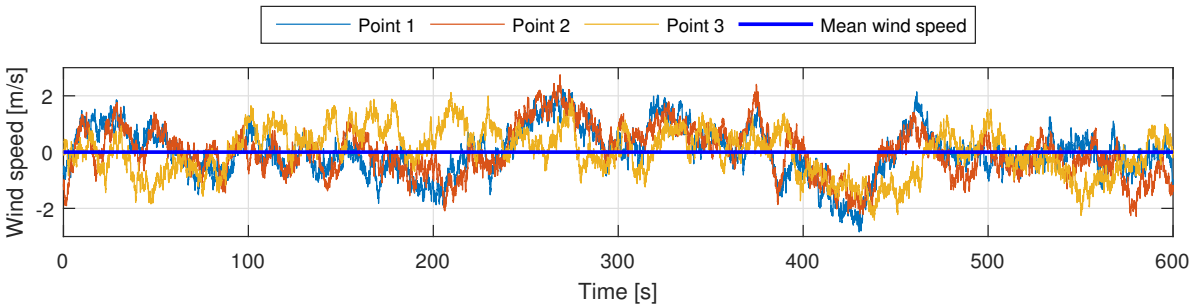

Figure 4.12: Time series of lateral component of velocity for three points in the turbulent wind field generated at a wind speed of 4.5 m/s.

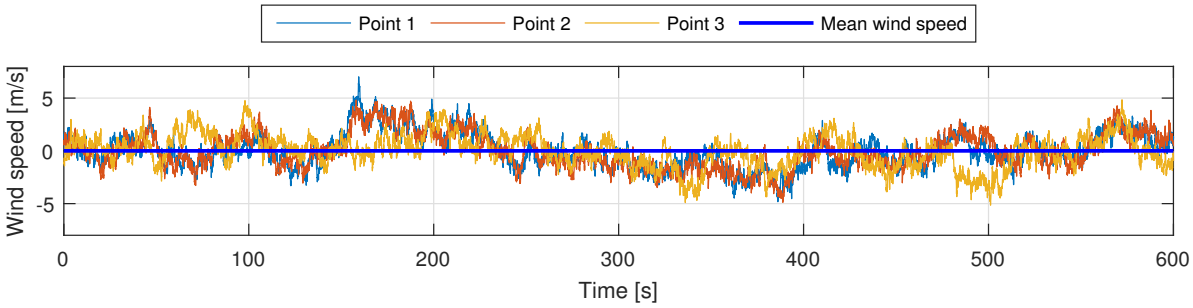

Figure 4.13: Time series of lateral component of velocity for three points in the turbulent wind field generated at a wind speed of 13.5 m/s.

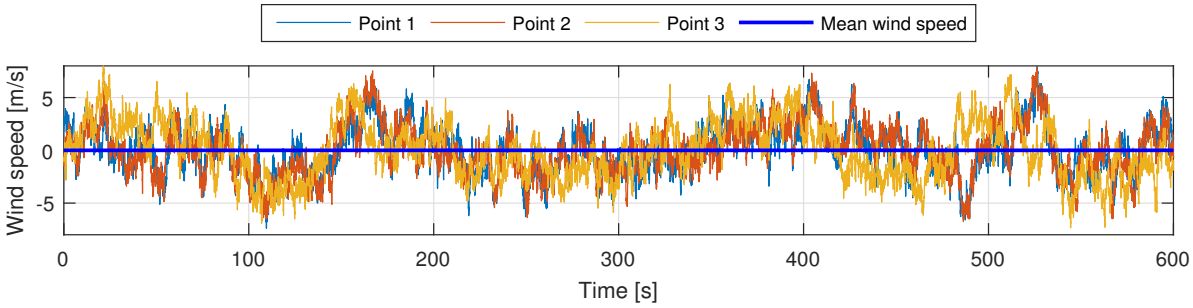

Figure 4.14: Time series of lateral component of velocity for three points in the turbulent wind field generated at a wind speed of 24.5 m/s.

From the above figures, it can be observed that the time series for points 1 and 2 look more alike while when compared to the time series for point 3. The histograms of time series of the horizontal wind velocity component at these points at wind speeds of 4.5 m/s, 13.5 m/s and 24.5 m/s can be seen in figures 4.15, 4.16, and 4.17 respectively.

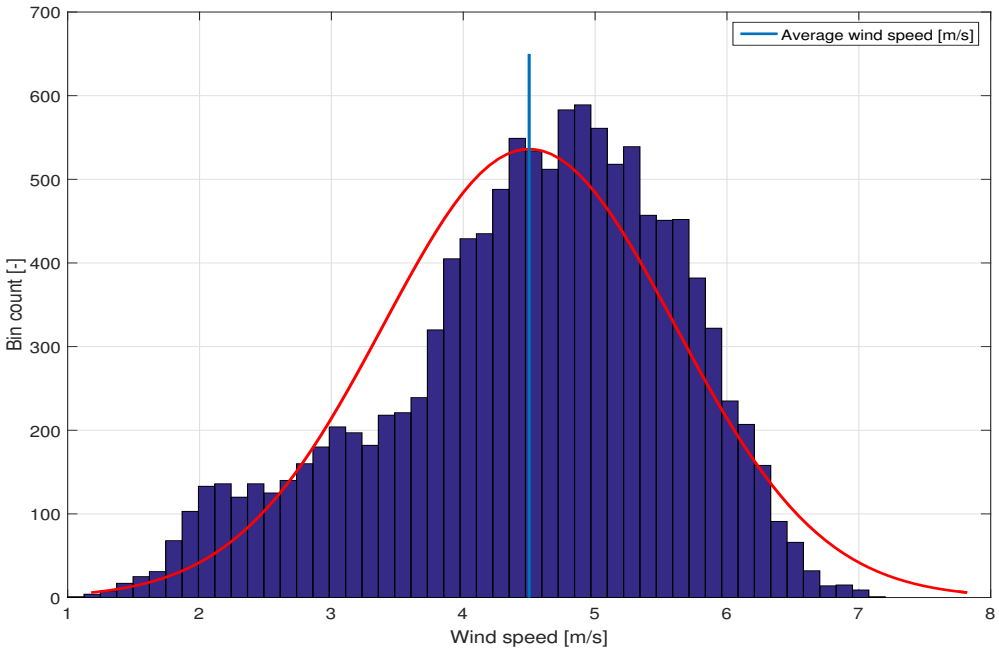

Figure 4.15: Histogram for wind velocity in horizontal direction at a wind speed of 4.5 m/s

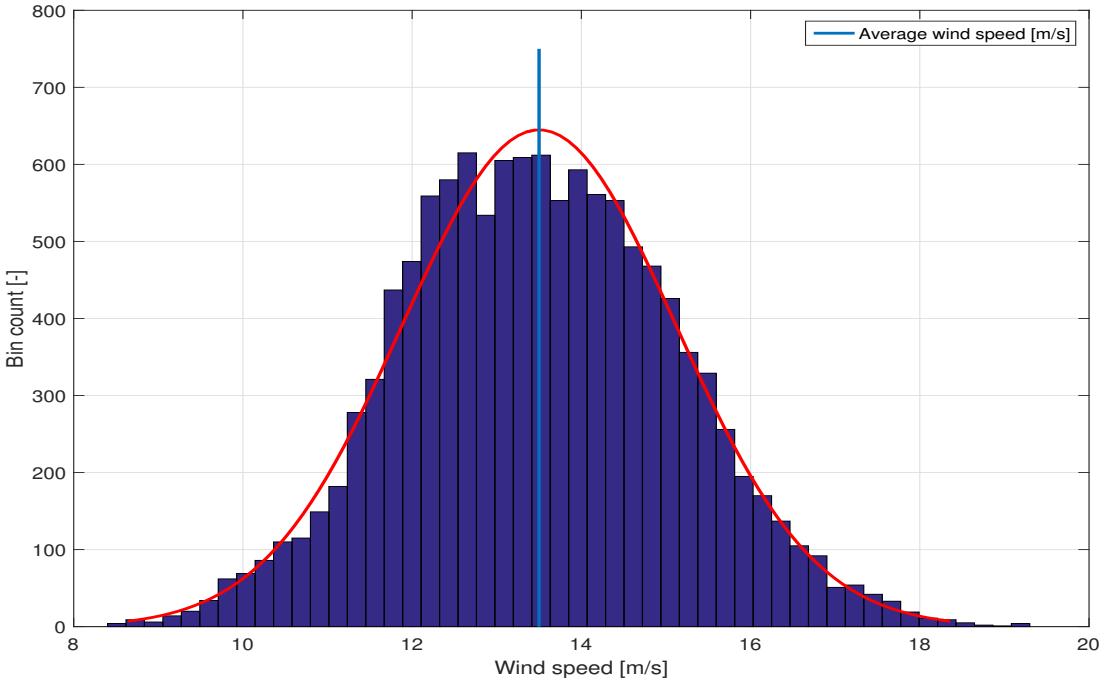

Figure 4.16: Histogram for wind velocity in horizontal direction at a wind speed of 13.5 m/s

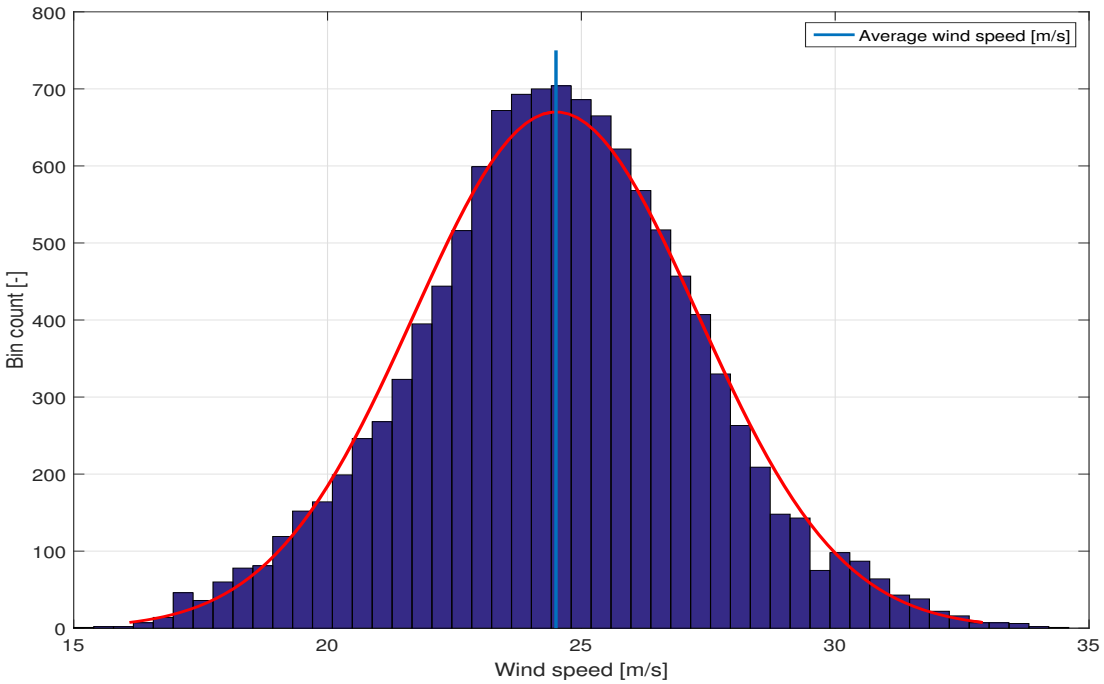

Figure 4.17: Histogram for wind velocity in horizontal direction at a wind speed of 24.5 m/s

The histograms of the time series of wind velocity in lateral direction can be seen in figures 4.18, 4.19 and 4.20.

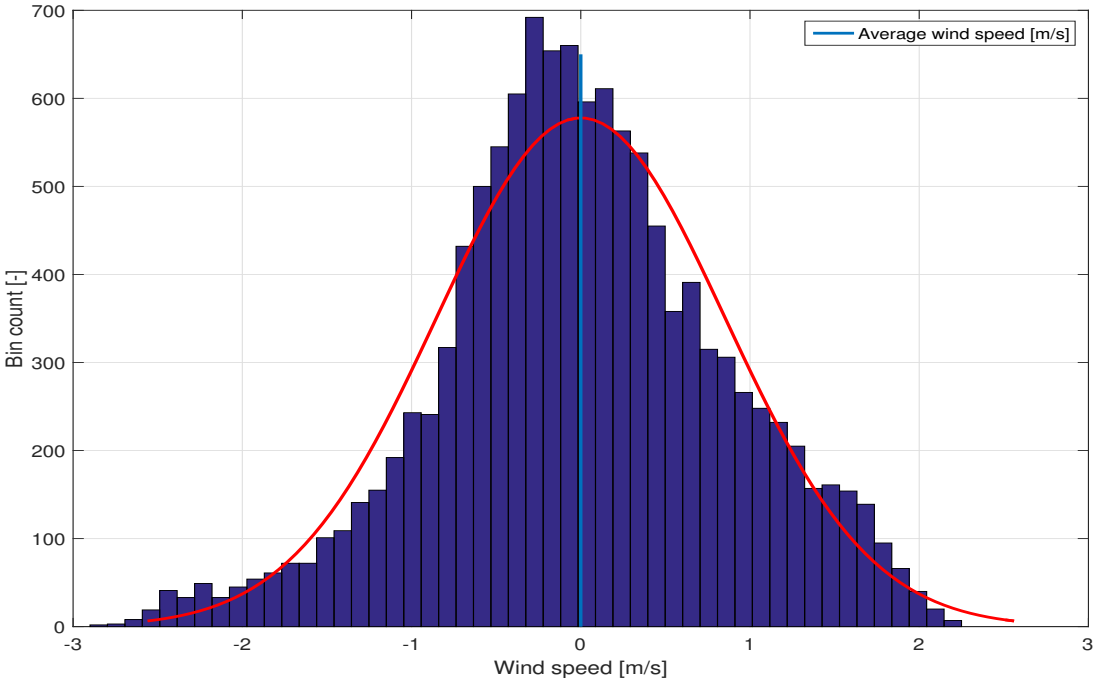

Figure 4.18: Histogram for wind velocity in lateral direction at a wind speed of 4.5 m/s

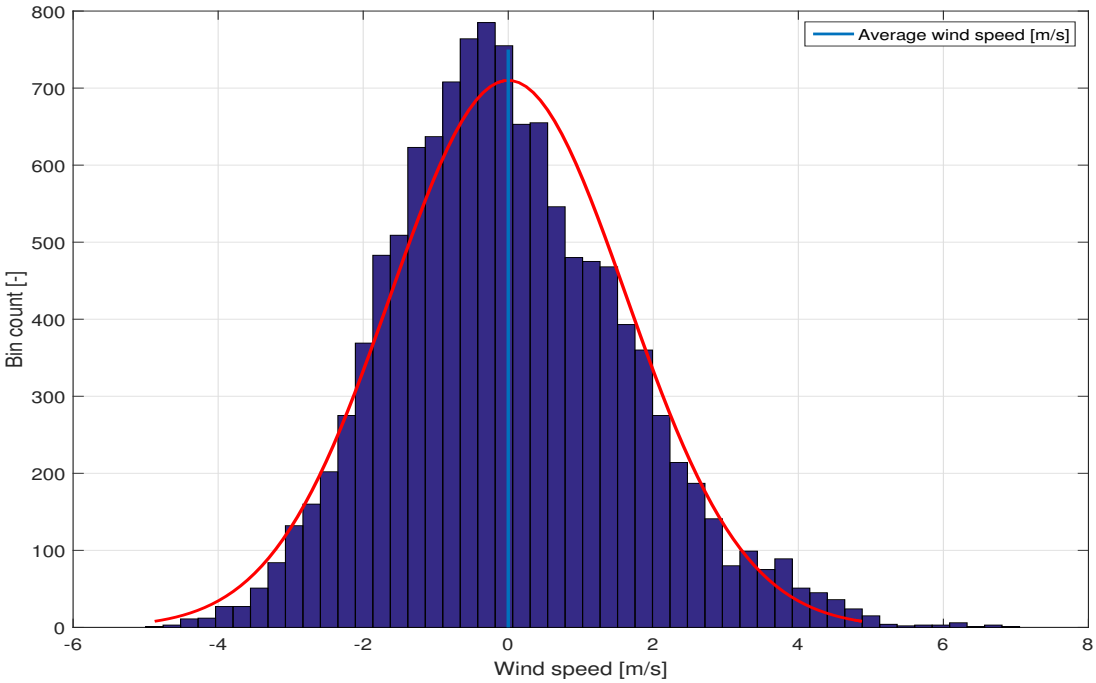

Figure 4.19: Histogram for wind velocity in lateral direction at a wind speed of 13.5 m/s

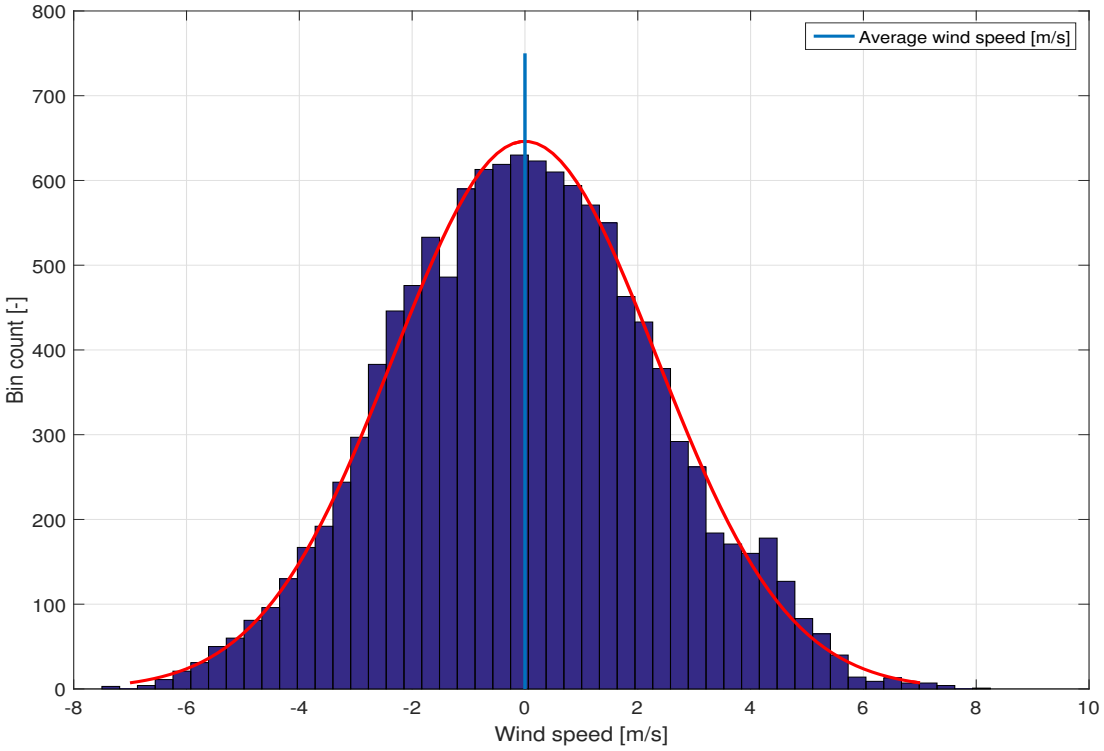

Figure 4.20: Histogram for wind velocity in lateral direction at a wind speed of 24.5 m/s

In the histograms for the wind speed in the lateral direction, the average wind speed is always zero. This is because there is no net wind speed in the lateral direction.

The histograms in the above figures prove that the time series of the generated wind fields follow the Gaussian distribution which is necessary to generate stochastic wind fields. On the other hand, the time series at two nearby points marked by green and white stars in figure 4.8 at different wind speeds are more similar to each other than the time series at a point located far away from them which is marked by the black star in the same figure (as observed from figures 4.9 to 4.14). This proves that the generated wind fields are correct and suitable for further use in this study. Therefore these wind fields were used for the simulations in this study.

4.3. SIMULATION OF NTM WIND FIELDS ON THE TURBINE

After the generation and verification of the NTM wind fields, they were simulated on the turbine. One hour simulations were done at each wind speed bin using six NTM fields of duration 600 seconds (10 minutes). These fields were generated using six different seeds. The turbulent wind fields were simulated only on the turbine and not its wake since only the forces and moments on the airfoils of the turbine are required for this study. Figure 4.21 shows the simulation of a sample turbulent wind field on the turbine. The black grid in this figure represents the turbulent wind field moving along the horizontal direction at the speed of the free stream. Since the turbulent wind field is of frozen type, the movement of turbine has no effect on the turbulent wind field.

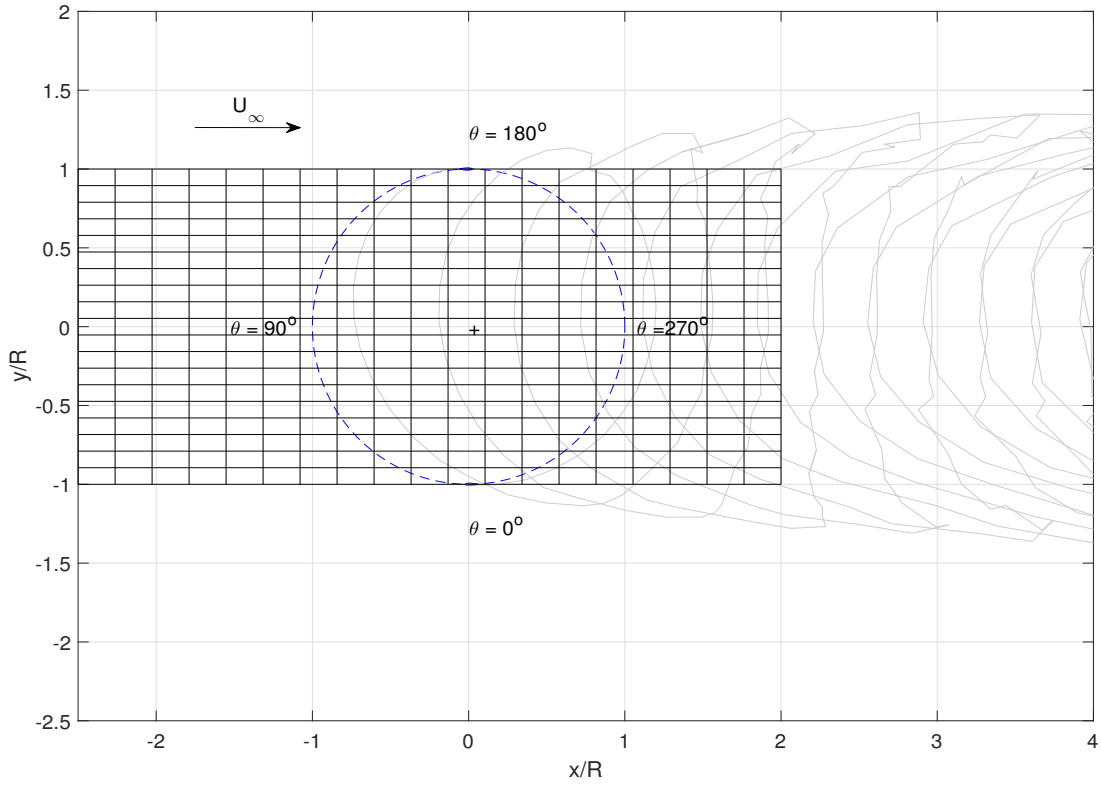

Figure 4.21: Simulation of a sample turbulent wind field on the turbine.

The velocities at the points of the turbine which did not coincide with the grid points of the turbulent wind field at a particular time step were calculated by two-dimensional interpolation. The forces and moments on the turbine airfoils were recorded at every 10^o of rotation of the turbine. This data was stored as a time series, with each time step containing the values of streamwise forces, cross-streamwise forces, and the moment at the centre of the airfoils of the turbine. Therefore a total of 36 time steps were recorded in every rotation of the turbine. It took 25 rotations (900 time steps) for the turbine wake to develop completely. Hence the turbulent wind fields were simulated after the turbine had completed 25 rotations. This means that the data of the first 900 time steps in every simulation was not used for calculations and post processing.

The total number of time steps required to complete a 10-minute simulation increased with increasing wind speed. This was because no control scheme was applied on the turbine and the tip speed ratio (λ) of the turbine remained constant. Therefore as the wind speed (U_∞) increased, the rotational speed (ω) of the turbine increased as well. This can be described as follows:

$$\lambda = \frac{\omega R}{U_\infty} \tag{4.7}$$

R is the radius of the turbine in the above equation. The value of λ remains constant throughout the simulations. Therefore the rotational speed (ω) of the turbine becomes proportional to the incoming wind speed (U_∞) and hence the number of rotations required for the simulations increased with increasing wind speed resulting in the increase in number of time steps. Table 4.2 shows the number of time steps required for each simulated wind speed.

Table 4.2: Time steps required for the wind speeds simulated

Wind speed [m/s]	Time steps [-]
4.5	1924
5.5	2151
6.5	2379
7.5	2606
8.5	2833
9.5	3061
10.5	3288
11.5	3516
12.5	3743
13.5	3970
14.5	4198
15.5	4425
16.5	4653
17.5	4880
18.5	5107
19.5	5335
20.5	5562
21.5	5790
22.5	6017
23.5	6245
24.5	6472

4.4. SIMULATION OF CONSTANT WIND ON THE TURBINE

In these simulations the velocity of the incoming wind remained constant throughout the simulations. These simulations were one hour simulations as well as opposed to varying velocity at different points in time in the previous simulations. The time steps required for each wind speed in these simulations was same as those required for turbulent wind fields (see table 4.2). The reader can refer to figure 3.5 for a better under-standing of simulations under these conditions. The results of these simulations were used as a baseline to understand the change in loads on the turbine under the influence of turbulence.

4.5. LOADS ON THE TURBINE

As mentioned in section 3.5, the outputs obtained from simulations in U2DiVA are the time series of streamwise and cross-streamwise forces (per unit span of the blade) normalized by dynamic pressure and the moments at specified points on the blades. The points specified in this study for the calculation of forces and moments were the quarter chord points of the airfoils. These time series are first multiplied by the dynamic pressure to obtain the actual values of streamwise and cross-streamwise forces. The tangential and radial forces (per unit span of the blade) on each blade were calculated as follows:

$$\begin{bmatrix} F_T \\ F_R \end{bmatrix} = \begin{bmatrix} -cos\theta & sin\theta \\ sin\theta & cos\theta \end{bmatrix}^{-1} \begin{bmatrix} F_x \\ F_y \end{bmatrix} = \begin{bmatrix} -cos\theta & sin\theta \\ sin\theta & cos\theta \end{bmatrix} \begin{bmatrix} F_x \\ F_y \end{bmatrix} \tag{4.8}$$

In the above equation F_T is the tangential force, F_R is the radial force, F_x is the streamwise force, F_y is the cross-streamwise force, and θ is the azimuth angle of the turbine. The position of these forces on the turbine blades at an azimuth angle θ can be seen in figure 4.22.

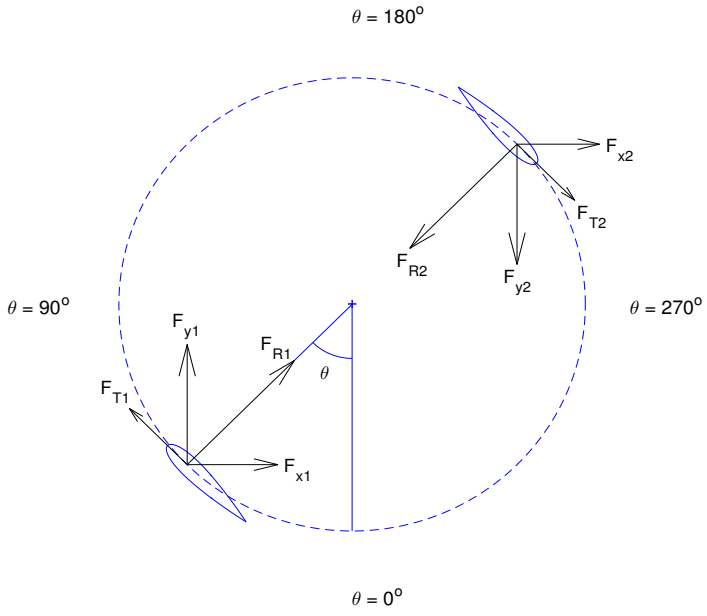

Figure 4.22: Positions of forces on the turbine blades

4.6. POST PROCESSING

4.6.1. EQUIVALENT LOAD CALCULATIONS

After the simulations on the turbine were done, the damage equivalent loads on the airfoils of the turbine from both simulations were calculated. The damage equivalent load on a component due to all the loads acting on it is defined as follows (Veldkamp, 2016):

$$F_{eq} = \left(\frac{1}{N_{eq}} \sum_j n_j F_j^m \right)^{\frac{1}{m}} \tag{4.9}$$

In the above equation, F_{eq} is the damage equivalent load, N_{eq} is an arbitrarily chosen number of cycles for which F_{eq} is applied on the component to produce the same damage as all other loads combined. F_j represents a load in the given load spectrum and n_j is the number of cycles for which the load F_j acted on the component while 'm' is the inverse slope of the material of the component. Generally the values of N_{eq} are 5×10^6, 10^7, or N_{eq} = L where L is the lifetime of the component when F_{eq} is applied on it with a frequency of 1 Hz. In this study the value of N_{eq} used is 5×10^6. The variable 'F' in equation 4.9 can be a force or a moment acting on the component.

In this study, the equivalent loads were calculated separately for the tangential force, the radial force and the moment about the centre of the airfoil for various values of 'm'. To calculate these loads, first the equivalent tangential force, radial force and moment at each wind speed were calculated using equation 4.9 for each value of m. Then the total equivalent tangential force, radial force and moment at each value of m were calculated using the following equation:

$$F_{eq,m} = \left[\sum_{U=4.5}^{24.5} F_{eq,U}^m \left[cdf\left(U+\frac{1}{2}\right) - cdf\left(U-\frac{1}{2}\right) \right] \right]^{\frac{1}{m}} \tag{4.10}$$

In the above equation, $F_{eq,U}$ is the total equivalent load (can be the tangential force or the radial force or the moment) at the wind speed U representative for the wind speed bin in which the calculations are done and cdf(U) represents the cumulative density function which defines the probability that the value of wind speed will be less than or equal to U.

4.6.2. ANALYSIS OF RESULTS

Once these calculations were performed, the results were analysed by means of various plots of the forces and moments obtained as a result of post processing against the representative wind speeds. Only one blade was considered for the analysis. The equivalent loads were plotted against the wind speeds for each value of m. The changes in equivalent loads due to turbulence were plotted against the values of m to see how sensitive these changes were with respect to the value of m. The changes in equivalent loads due to turbulence were calculated with respect to total equivalent loads due to constant wind. This was done using the following equation:

$$\Delta F_{eq} = \frac{F_{eq,NTM} - F_{eq,clean}}{F_{eq,clean}} \times 100 \tag{4.11}$$

In the above equation, ΔF_{eq} is the change in equivalent load, $F_{eq,NTM}$ is the equivalent load due to turbulent wind and $F_{eq,clean}$ is the equivalent load due to constant wind. These loads were calculated for each value of m using equation 4.10. After this the loads for the value of inverse slope equal to 10 were studied, since this value is recommended in literature (Brøndsted *et al.*, 2005). This was coupled with simulations aimed at finding the effect of phase angle on the loads. The phase angles used for this study were 0^o, 45^o, 90^o, and 135^o and the simulations were done using the same turbulent wind models used earlier in this study. The loads due to the effect of phase angles were compared to the loads due to phase angle of 0^o using following equation:

$$\Delta F_{eq} = \frac{F_{eq,0} - F_{eq,phase}}{F_{eq,0}} \times 100 \tag{4.12}$$

In the above equation, $F_{eq,0}$ is the equivalent load when the phase angle is 0^o while $F_{eq,phase}$ is the equivalent load at a particular phase angle. The phase angle 0^o was used to compare the loads since the normal simulations are done at this phase angle.

The equivalent loads are calculated in terms of stresses (σ) which are proportional to the moments (M) due to various forces as follows:

$$\sigma \propto M = FH \tag{4.13}$$

In the above equation, H is the perpendicular distance between the point of calculation of moment and the point where the force acts. In this study only the changes in equivalent loads have been studied. Since the perpendicular distance 'H' remains constant and only the value of force changes, hence any change in the force according to equations 4.11 and 4.12 is equal to the change in corresponding moments as well.

5

RESULTS AND DISCUSSIONS

5.1. VARIATION IN LOADS

After the simulations were performed, first the variations in loads were observed for the cut-in (4.5 m/s), rated (13.5 m/s), and cut-out (24.5 m/s) wind speeds. The figures show the variation under both, constant and turbulent winds.

5.1.1. TANGENTIAL FORCE

A part of the time series of tangential force on the blade for the cut-in, rated, and cut-out wind speeds can be seen in figures 5.1, 5.2, and 5.3 respectively.

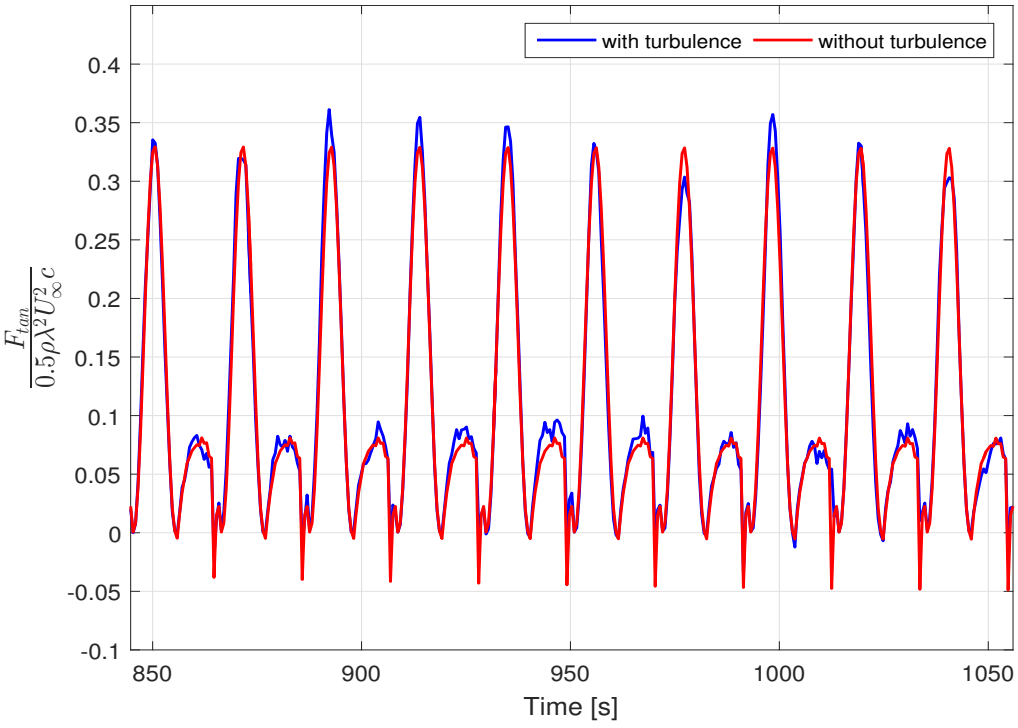

Figure 5.1: Time series of tangential force at wind speed of 4.5 m/s

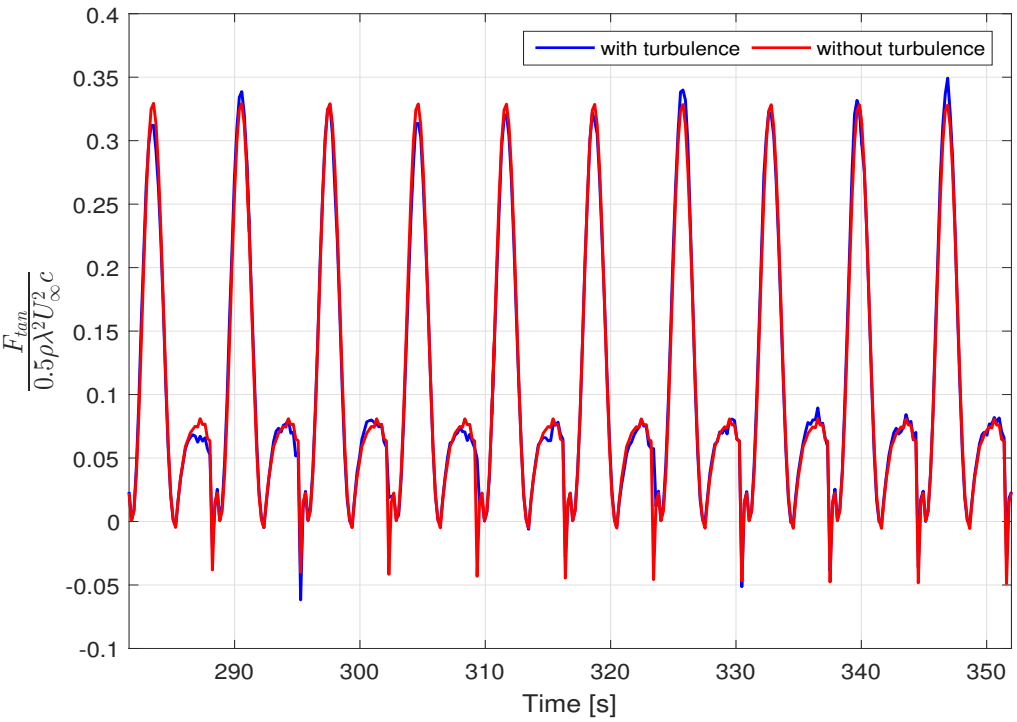

Figure 5.2: Time series of tangential force with time at wind speed of 13.5 m/s

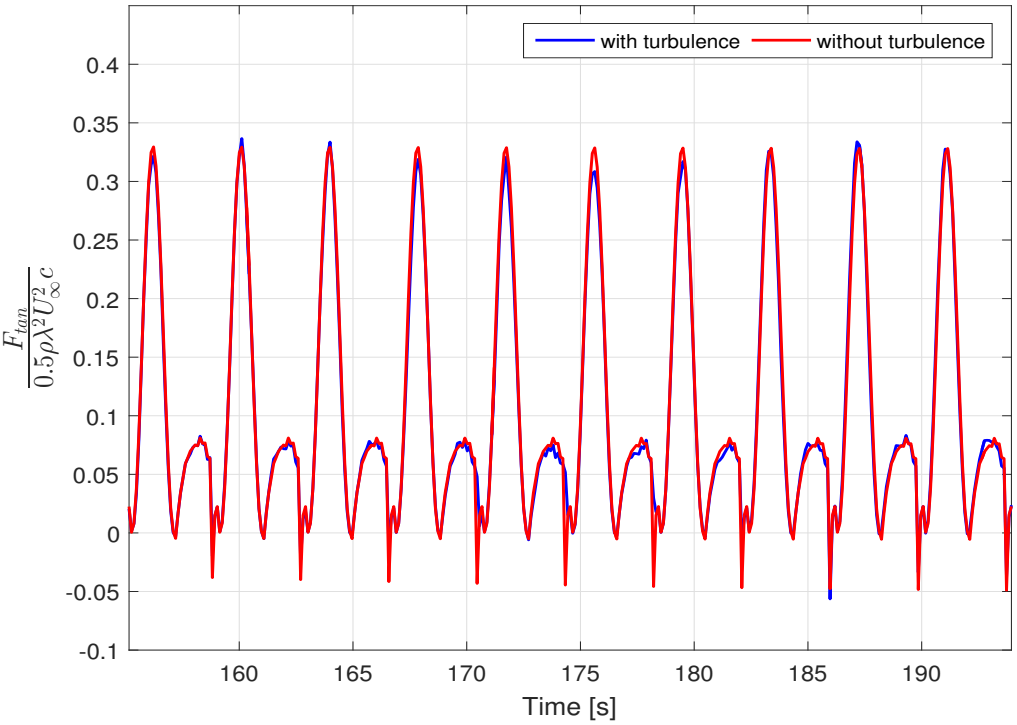

Figure 5.3: Time series of tangential force with time at wind speed of 24.5 m/s

For all three wind speeds it can be observed that there was more variation in tangential force under turbulent wind when compared to turbulent wind. The variation in tangential force due to turbulence reduced with increasing wind speed.

5.1.2. RADIAL FORCE

A part of the time series of radial force on the blade at the cut-in, rated, and cut-out wind speeds can be seen in figures 5.4, 5.5, and 5.6

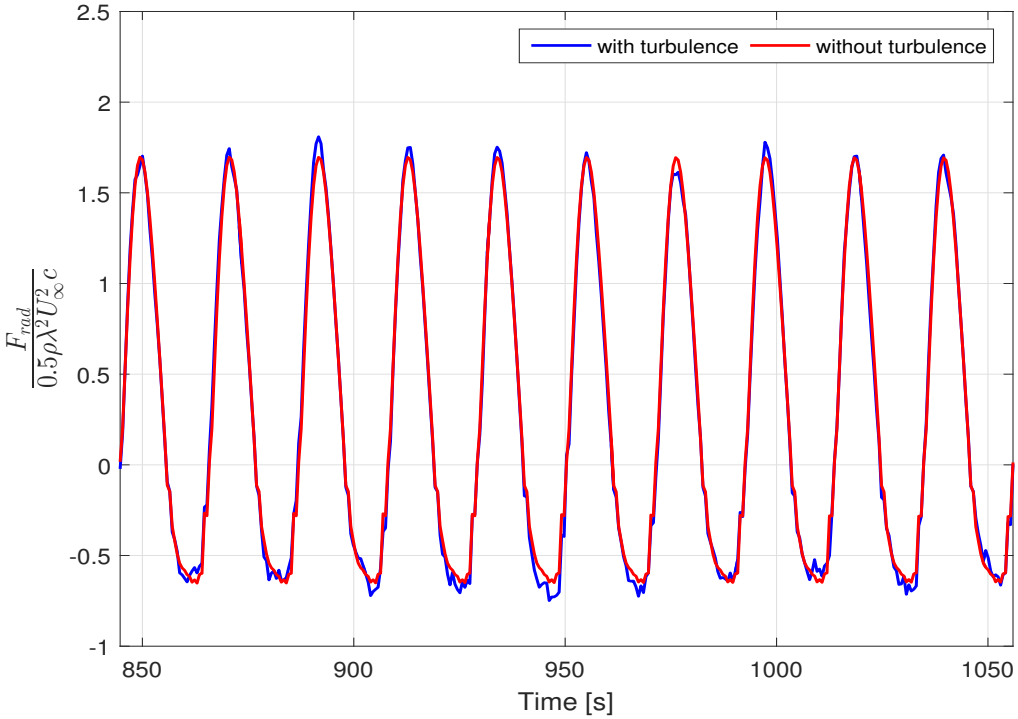

Figure 5.4: Time series of radial force at wind speed of 4.5 m/s

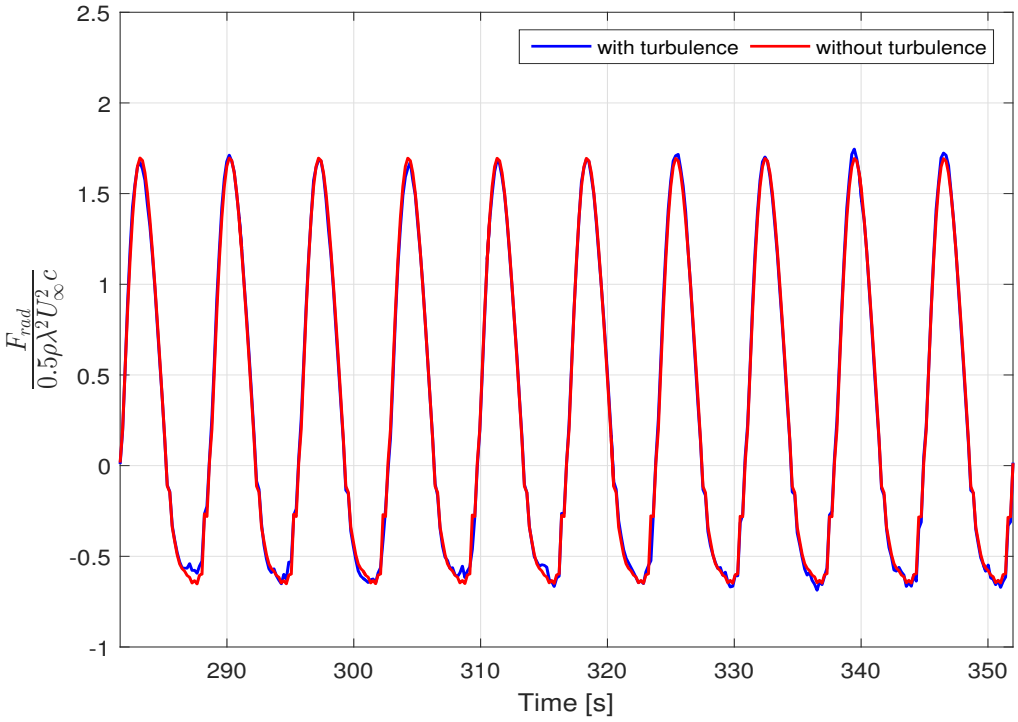

Figure 5.5: Time series of radial force at wind speed of 13.5 m/s

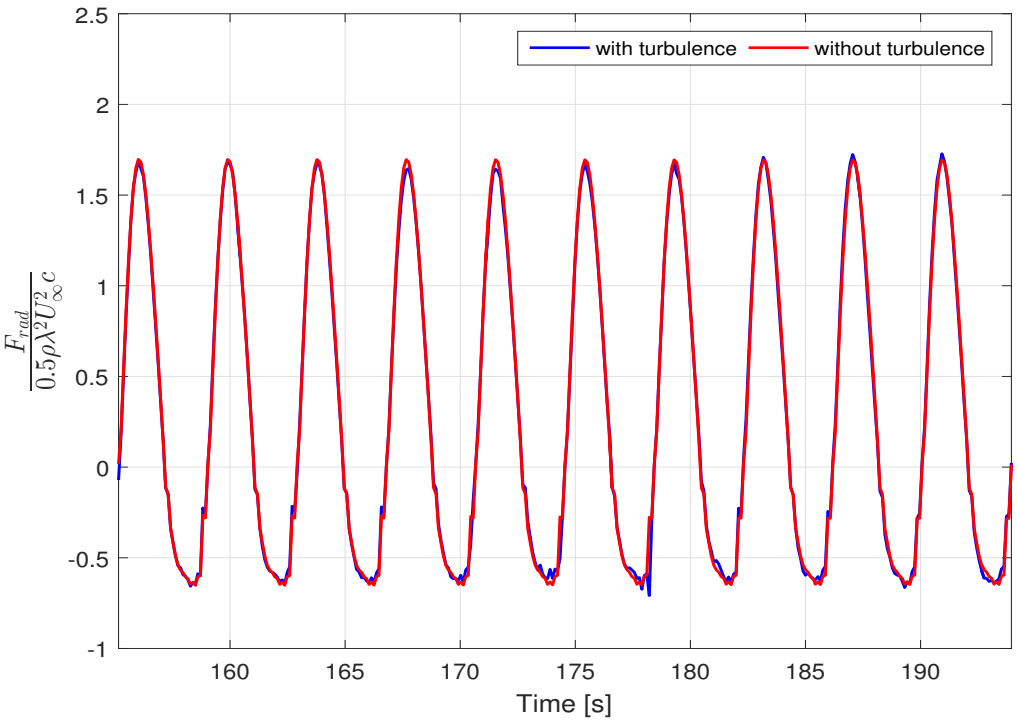

Figure 5.6: Time series of radial force at wind speed of 24.5 m/s

Similar to the tangential forces on the blades, the variation in radial forces under the influence of turbulent wind was more when compared to constant wind and decreased with increasing wind speed.

5.1.3. MOMENT

The time series of the moment on the blade can be seen in figures 5.7, 5.8, and 5.9.

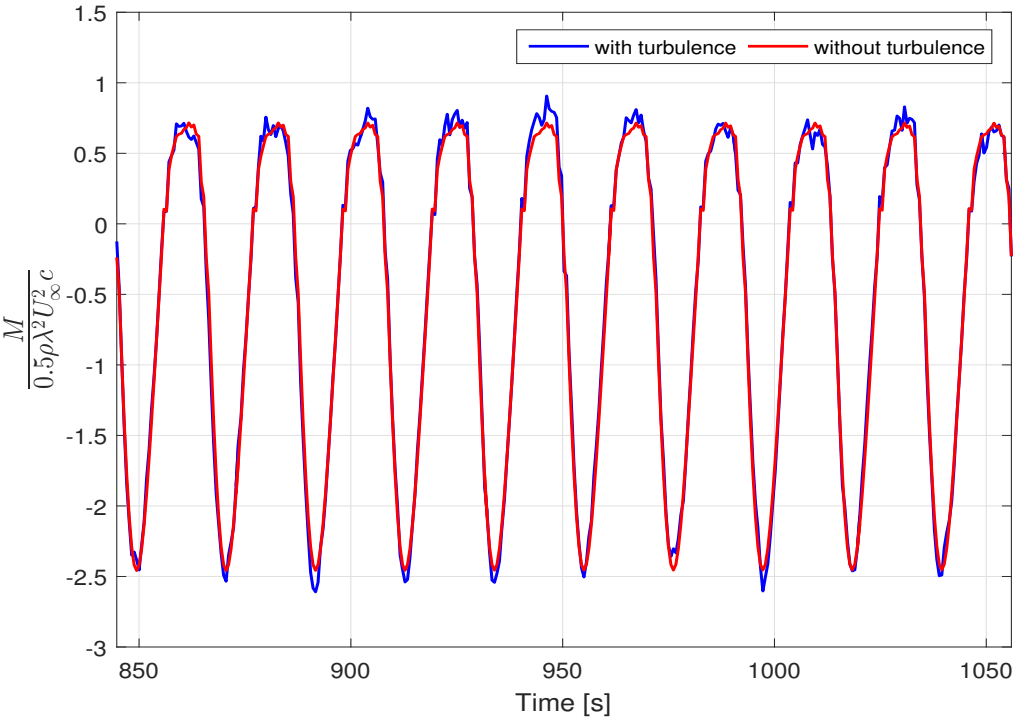

Figure 5.7: Time series of moment at wind speed of 4.5 m/s

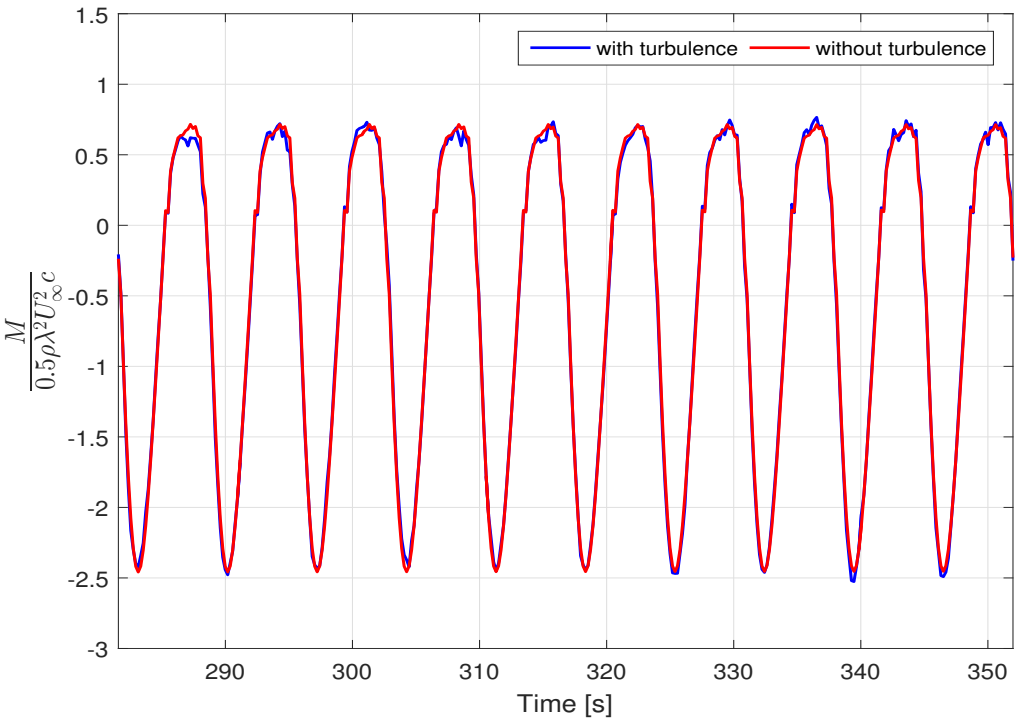

Figure 5.8: Time series of moment at wind speed of 13.5 m/s

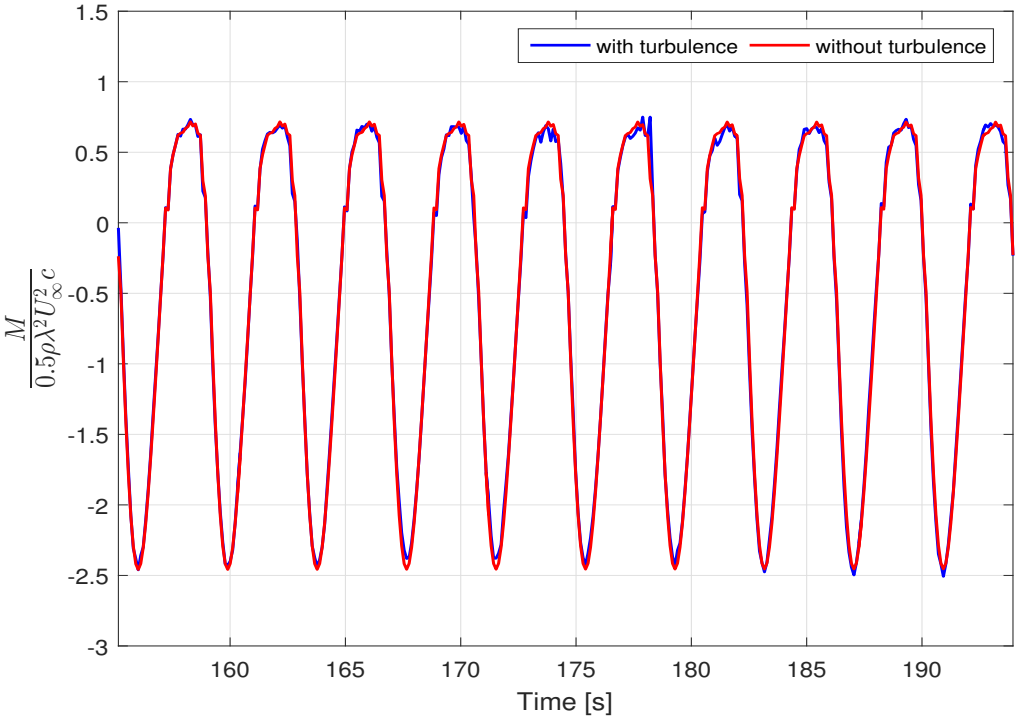

Figure 5.9: Time series of moment at wind speed of 24.5 m/s

The trend of variation in moment along with time is similar to other loads. The reduction in variation in loads due to the turbulent wind is due to the decrease in turbulence intensity with increasing wind speed (see figure 4.2). The time series of these loads were subsequently subjected to rainflow counting, to include only the relevant load ranges for further calculations.

5.2. RAINFLOW COUNTING

The rainflow counting for the loads was done using same bins for every wind speed. The number of bins defined was 50. For equivalent load calculation, the highest value of load in each bin (upper limit of the bin) was used as specified in Sutherland (1999). The results of rainflow counting for the tangential force, radial force, and moment about the aerodynamic centre of the airfoil can be seen in figures 5.10, 5.11, and 5.12. The number of cycles in each bin shown in these figures is the estimated number of cycles that would occur in 20 years, i.e. the lifetime of the turbine.

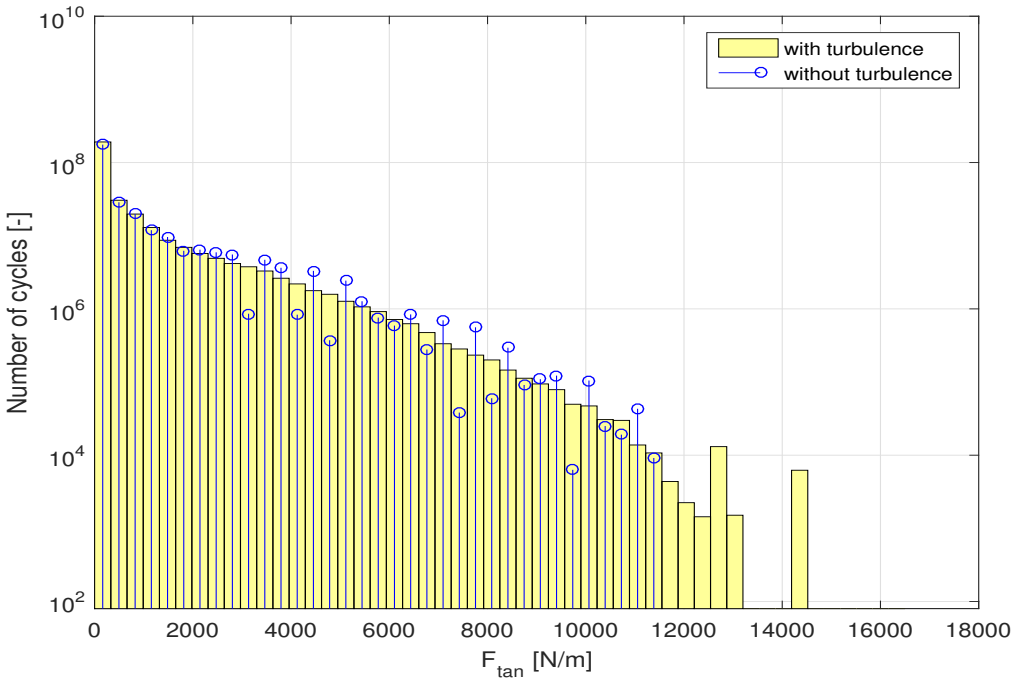

Figure 5.10: Rainflow counting results for the tangential force (F_{tan}) on the airfoils.

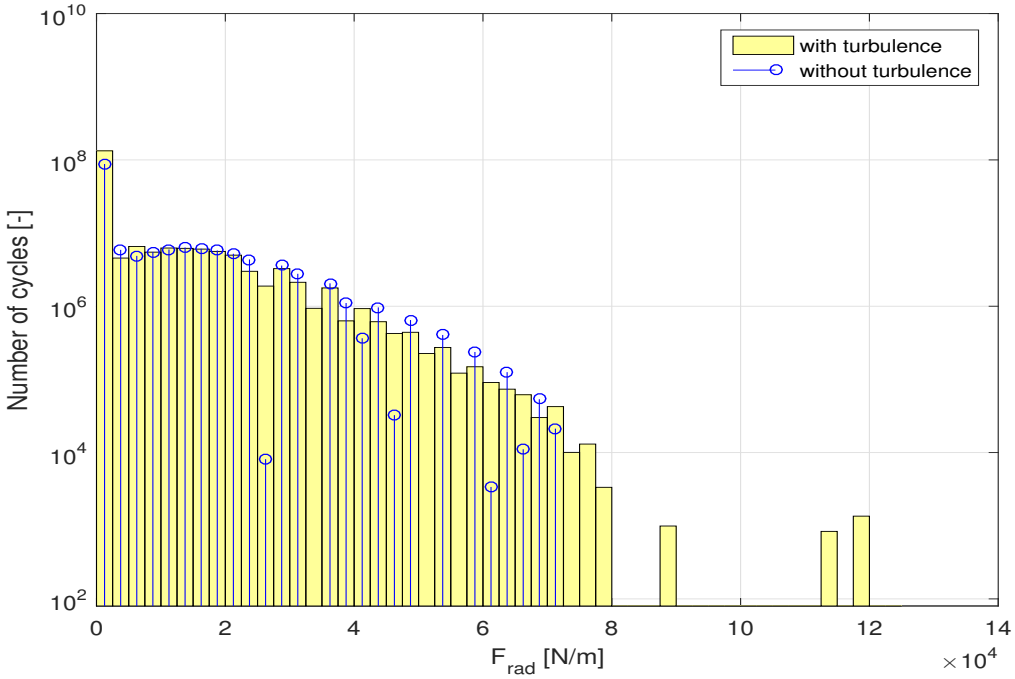

Figure 5.11: Rainflow counting results for the radial force (F_{rad}) on the airfoils.

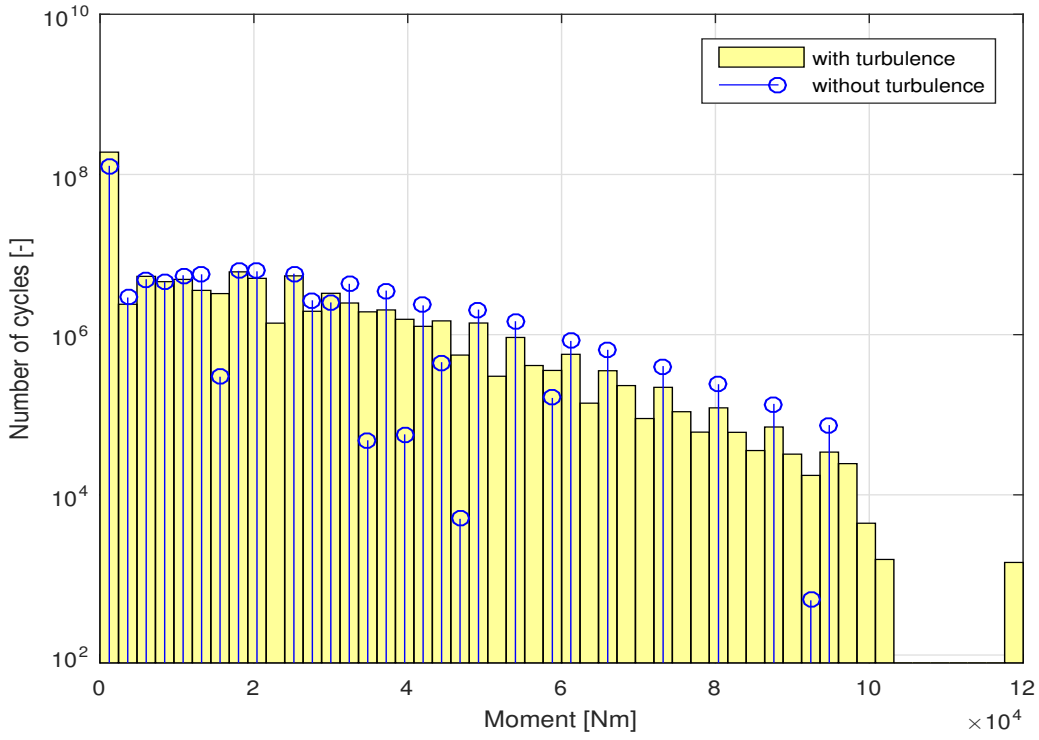

Figure 5.12: Rainflow counting results for the Moment on the airfoils.

The above figures have been plotted with a semi-log scale on the y-axis. For all three loads, the number of cycles in the first bin is significantly high when compared to other bins. While the loads under the effect of turbulent wind seem to decrease gradually, the same is not the case for the constant wind. No cycles due to constant wind are present in some of the load ranges of the radial force and the moment. Additionally, some more load cycles appear in the higher load ranges in case of turbulent wind. For all the loads, the number of cycles in most of the bins is almost equal for both cases. Overall, it can be observed that the number of cycles under turbulent wind is greater than under the constant wind. Very few cycles are present in the higher load ranges under the constant wind when compared to the turbulent wind. The presence of large number of cycles in these ranges under the turbulent wind (especially for the tangential force and the moment) can significantly affect the fatigue life of the turbine and should be considered in future developments of the design of the turbine.

The variation of number of load cycles for the tangential force, the radial force, and the moment with wind speed for both turbulent wind and constant wind can be seen in figures 5.13, 5.14, and 5.15 respectively. These numbers are defined only for one hour simulations. It can be observed from all the figures the number of cycles increases with increasing wind speed for both cases. This is because the tip-speed ratio of the turbine is greater than one and this leads to the turbine rotate at higher speeds with increasing wind speed (see equation 4.7). For constant wind, this increase is almost linear for all the loads except at low wind speeds (up to 6.5 m/s) in case of tangential force. For turbulent wind, the increase is not linear and the number of cycles at each wind speed is greater than that in case of constant wind. The non-linear increase in the number of cycles in this case is due to the velocity fluctuations in the turbulent wind fields. For tangential forces, the number of cycles due to turbulent wind is lesser than those due to constant wind up to a wind speed of 6.5 m/s. The difference in number of cycles from both cases increased with increasing wind speed. The increase in number of cycles with wind speed for tangential force is the lowest while it was highest for the radial force.

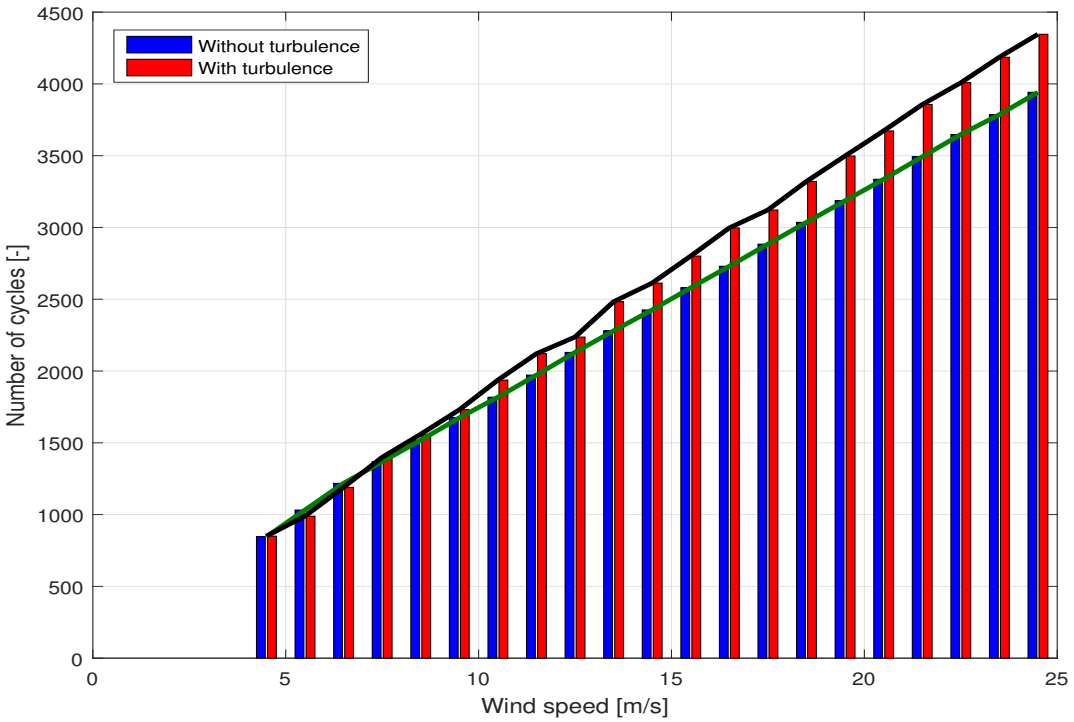

Figure 5.13: Variation of number of cycles of tangential force with wind speed.

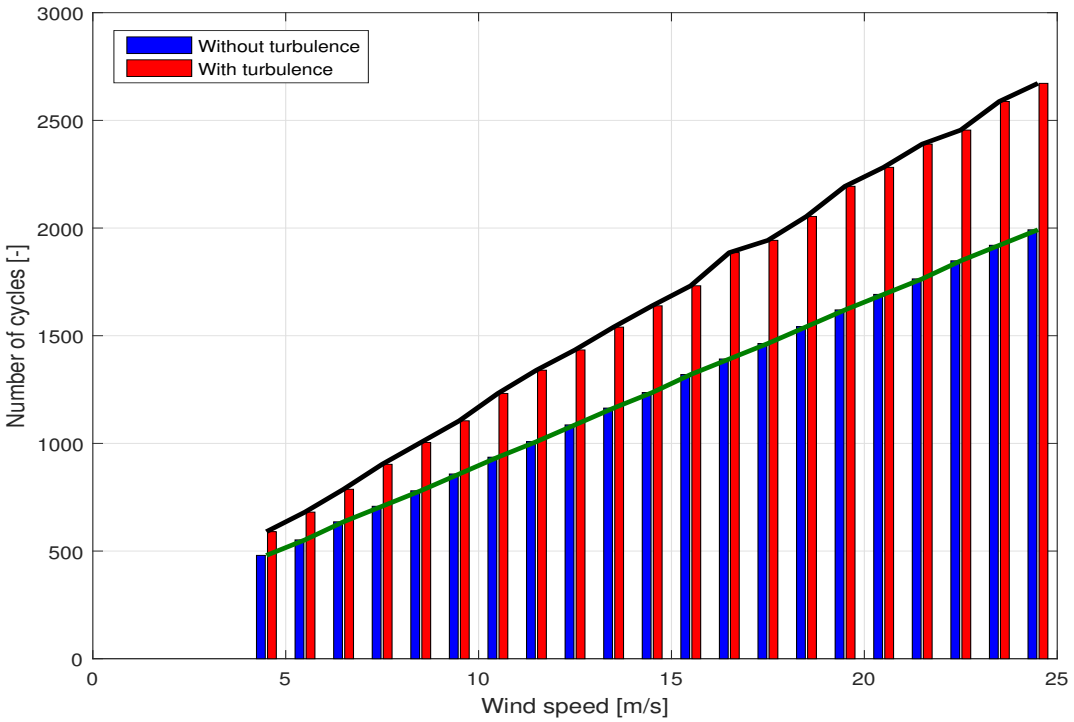

Figure 5.14: Variation of number of cycles of radial force with wind speed.

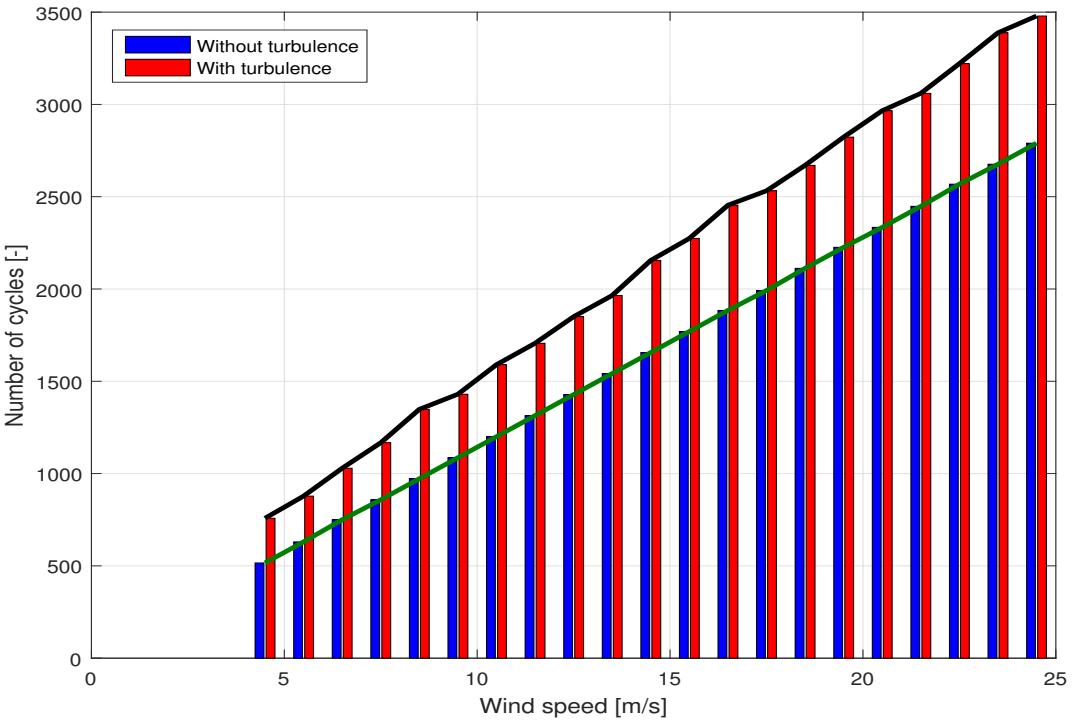

Figure 5.15: Variation of number of cycles of moment with wind speed.

5.3. VARIATION IN EQUIVALENT LOADS FOR DIFFERENT INVERSE SLOPES

After the rainflow counting, the equivalent loads at each wind speed were calculated using equation 4.8. The variation of these loads with wind speeds for different values of inverse slope (m) of the S-N curve can be seen in figures 5.16, 5.17, and 5.18. These loads were calculated for the whole lifetime of the turbine.

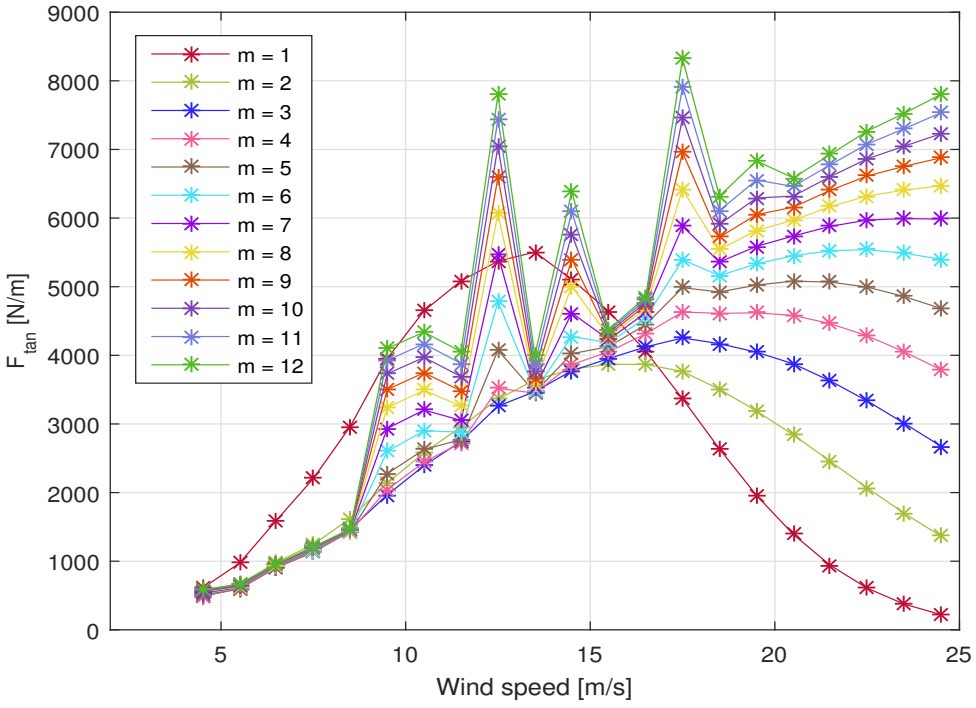

Figure 5.16: Variation of equivalent tangential force with wind speed for various inverse slopes.

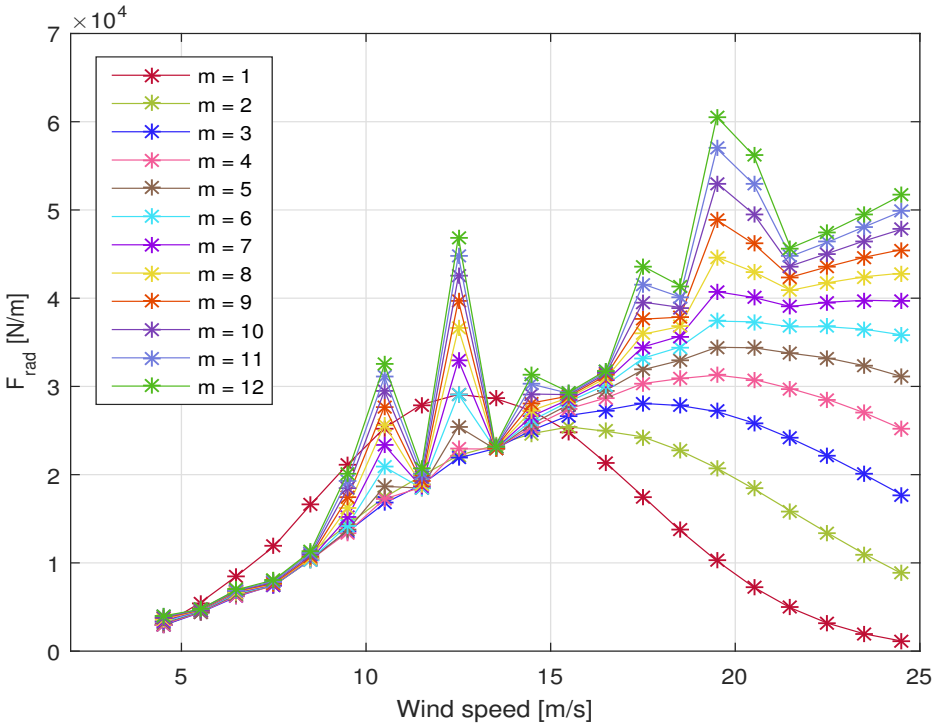

Figure 5.17: Variation of equivalent radial force with wind speed for various inverse slopes.

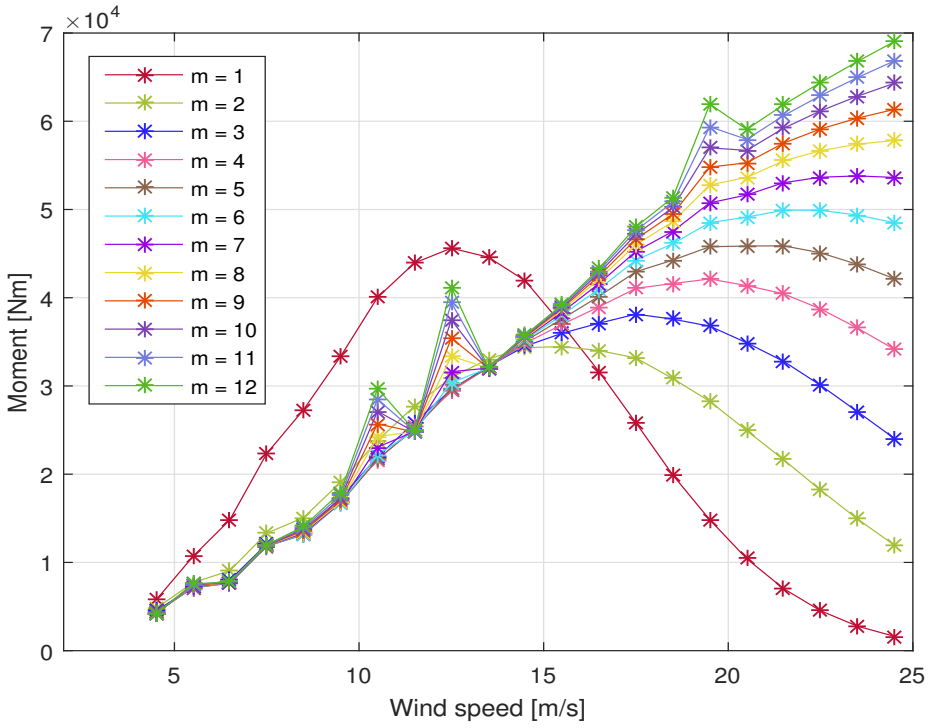

Figure 5.18: Variation of equivalent moment with wind speed for various inverse slopes.

The equivalent loads tend to follow the Gaussian distribution at lower values of the inverse slope. This is clearly visible for the value of inverse slope equal to 1. In general, for higher values of inverse slope (greater

than 4), some peaks are observed at various wind speeds instead of a steady increase. A sudden decrease in the values of equivalent loads is also observed after the value of inverse slope increases from 1 to 2. From wind speed of 4.5 m/s up to 8.5 m/s, the values of equivalent loads are almost equal for all values of inverse slope greater than 1.

For tangential force, the maximum values were obtained at the wind speed of 17.5 m/s for values of inverse slope greater than 2. Local peaks occurred at wind speeds of 10.5 m/s, 12.5 m/s, and 14.5 m/s for values of inverse slope greater than 4. Another local maximum was observed at the wind speed of 19.5 m/s but only for values of inverse slope greater than 10. For the radial force, the maximum value was observed at wind speed of 19.5 m/s for values of inverse slope greater than 3. The local peaks followed a similar trend as that of the tangential force. For the moment, no local peaks occurred at wind speed of 14.5 m/s and 17.5 m/s. Local peaks also occurred at wind speed of 19.5 m/s only when the value of inverse slope was greater than 9. The maximum values of equivalent moment occurred at the cut-out speed for values of inverse slope greater than 6. Below this value, the maximum values of equivalent moment occurred at different wind speeds.

5.4. CHANGES IN TOTAL EQUIVALENT LOADS WITH INVERSE SLOPE

As mentioned in section 4.6.2, the changes in total equivalent loads were found out with respect to equivalent loads due to constant wind for each value of the inverse slope. The total equivalent loads were calculated using equation 4.10. Figures 5.19, 5.20, and 5.21 show the variation of change in equivalent load due to turbulent wind for the tangential force, the radial force, and the moment respectively for various values of inverse slope.

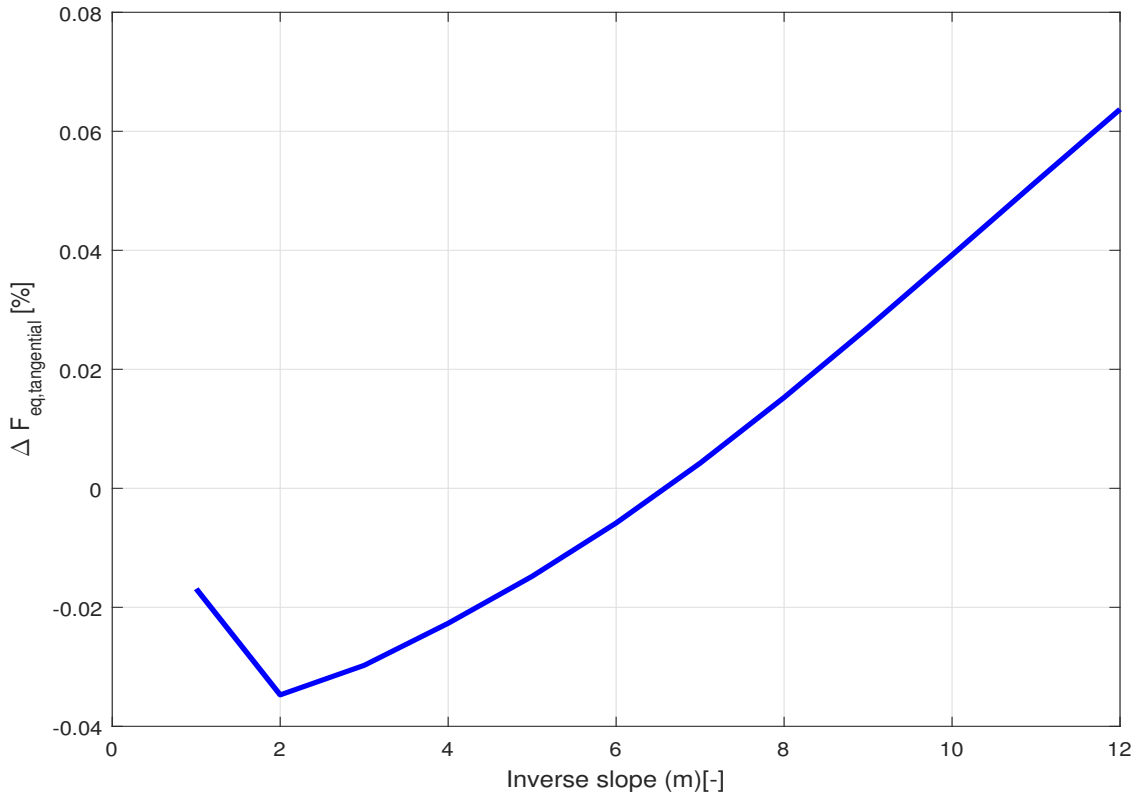

Figure 5.19: Variation of change in equivalent tangential force with inverse slope.

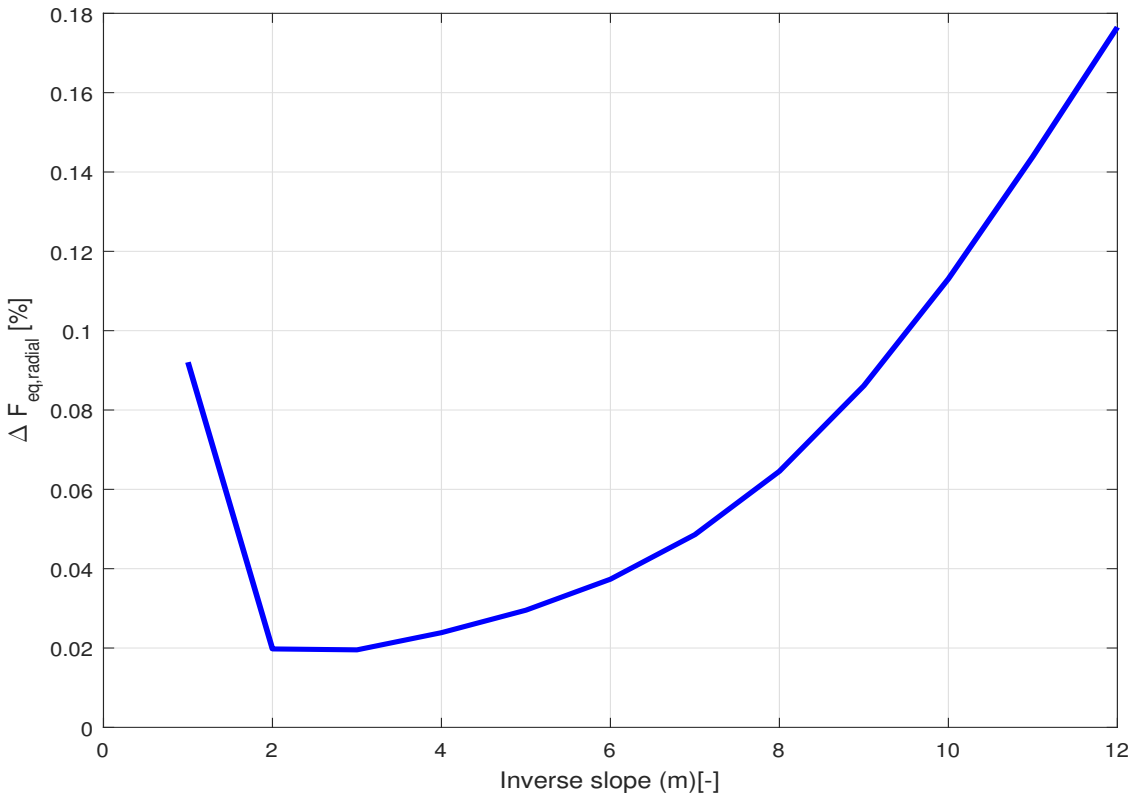

Figure 5.20: Variation of change in equivalent radial force with inverse slope.

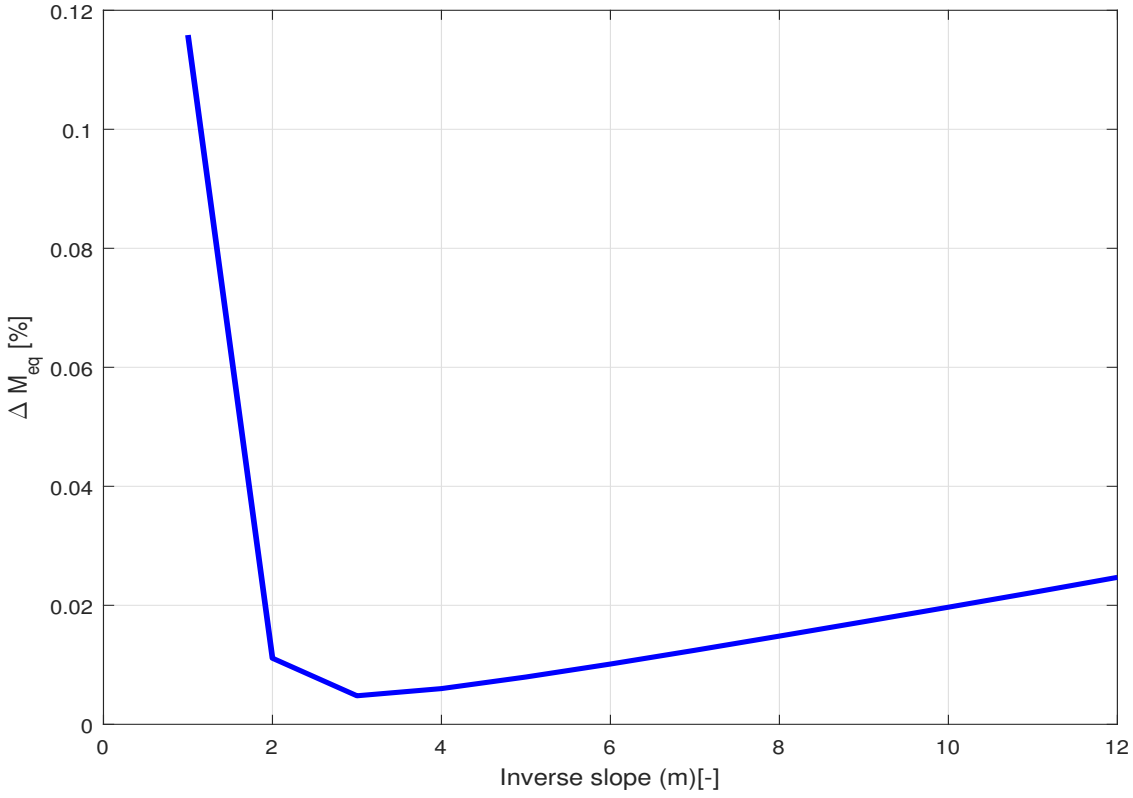

Figure 5.21: Variation of change in equivalent moment with inverse slope.

In these figures, it can be seen that after an initial decrease in the change in equivalent loads, the change in the loads continues to increase. The maximum increase among the loads is only around 0.18%.

For tangential force, the maximum change is around 0.06%. The change is negative until the value of inverse slope is around 7. This means that the equivalent tangential force decreases under the influence of turbulence till the value of inverse slope is less than 7. In case of radial force, the equivalent force starts increasing after the value of inverse slope increases from 3. The maximum increase is around 0.18% when the value of inverse slope is 12 while the minimum increase is 0.02% when the value of 2 and 3. For moment about the aerodynamic centre, there is a sharp decrease in the change when the value of inverse slope changes from 1 to 2. The minimum change is 0.008% when the value of the inverse slope is 3 and the maximum change is around 0.12% when the value is 1.

While it is clear that the net increase in loads is always less than 0.2%, the values of inverse slope where the minimum change in loads takes place is either 2 or 3. The material which has inverse slope around these values is welded steel (Veldkamp, 2006). Steel is relatively heavy and hence it is not suitable for commercial turbines. The other material that can be used is aluminium which has an inverse slope value of 6 (Sutherland, 1999). During 1970's, 80's, and 90's, 6063 T5 aluminium (also known as extrudable aluminium) was used to manufacture VAWT blades. One of the main reasons for this was the light weight of the aluminium blades. The resulting turbines had poor fatigue life and the failure usually occurred at joint structures which had large stress concentrations (Sutherland *et al.*, 2012). Hence, aluminium cannot be regarded as a suitable material for VAWT blades. Currently, composites have become the choice of material for blades since they can be tailored according to the loads and have high stiffness and strength. Usually, fibreglass composites are used to manufacture wind turbine blades which have an inverse slope of 10 or higher (Sutherland, 1999).

It is clear from the results of this study that the change in equivalent loads due to turbulent wind is very small and hence materials with high values of inverse slopes (greater than 10) can be used. Hence the choice of composites is justified for the manufacturing of wind turbine blades.

5.5. EFFECT OF PHASE ANGLE ON THE LOADS

Once it was confirmed that the composites can be used for manufacturing of VAWT blades, it was decided that the inverse slope value of 10 would be used for the remaining part of this study. This slope has been recommended in the literature (Brøndsted *et al.*, 2005). Furthermore, the material used to manufacture blades for the VAWT used in this study is unidirectional fibre reinforced glass epoxy which has an inverse slope value of around 10 (Philippidis *et al.*, 2006). Therefore it is suitable to use this value.

Phase angle is the angle between the incoming wind stream and the blades of the turbine at the beginning of the simulations. An example of the phase angle can be seen in figure 4.22 (also denoted by θ). The phase angle is zero degrees when the chords of the blades are parallel to the direction of the incoming wind stream at the beginning of the simulations. Simulations were done for four phase angles namely 0^o, 45^o, 90^o, and 135^o. To find the effect of phase angle on the loads, the variation in number of load cycles, equivalent load at each wind speed and equivalent loads due to the equivalent loads at each wind speed were studied.

5.5.1. VARIATION IN THE NUMBER OF LOAD CYCLES WITH WIND SPEED

The variation in number of load cycles of tangential force, radial force, and moment with wind speed can be seen figures 5.22, 5.23, and 5.24 respectively. For the tangential force, the number of load cycles show a continuous increase with wind speed only for 0^o phase angle. For other angles the number of cycles first increased up to a certain wind speed and then decreased suddenly (except 45^o) and increased later. For 45^o phase angle, the number of cycles decreased between 12.5 m/s 14.5 m/s. For 90^o and 135^o phase angles, the decrease was observed at wind speeds of 15.5 m/s and 12.5 m/s respectively. The number of cycles were highest for 0^o phase angle followed by 45^o,135^o, and 90^o respectively.

For the radial force and the moment, the number of cycles continuously increased with wind speed. In case of the radial force, the highest number of load cycles were observed for 90^o phase angle followed by 135^o, 45^o, and 0^o respectively. For the moment, the number of load cycles were almost the same for phase angles 45^o and 135^o, and, 0^o and 90^o with 45^o and 135^o having larger number of cycles.

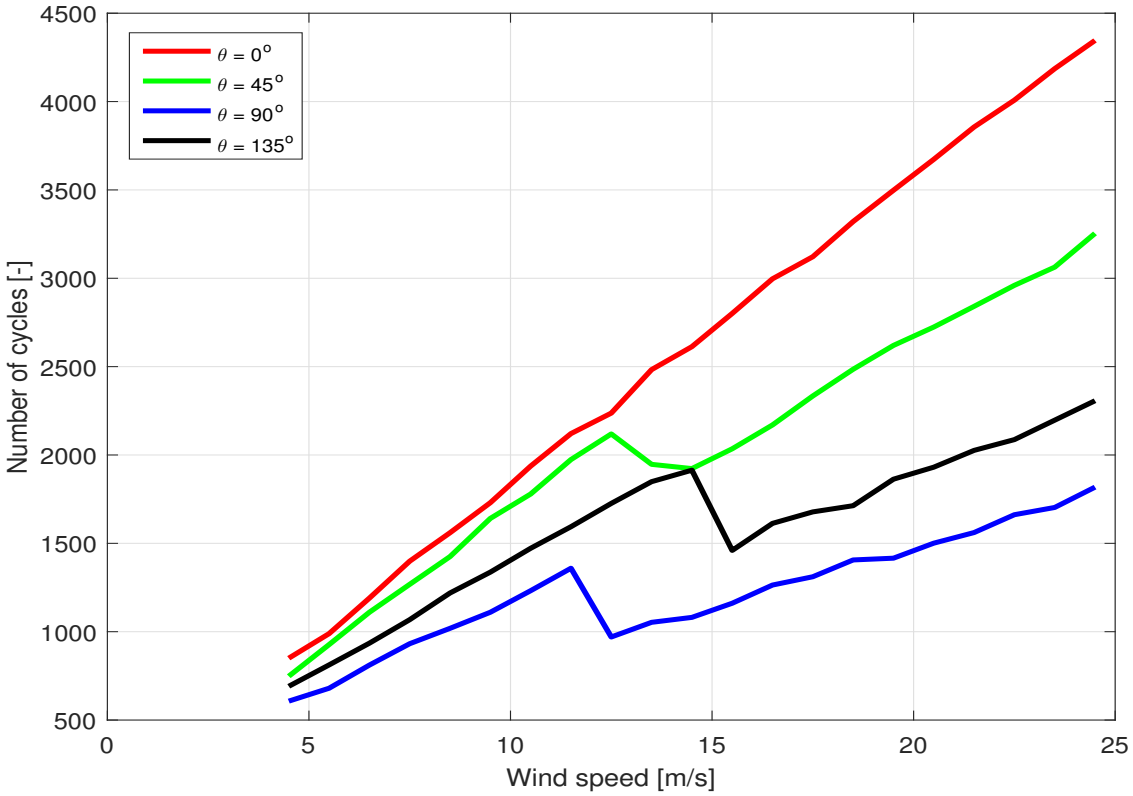

Figure 5.22: Variation of number of cycles of tangential force with wind speed for different phase angles.

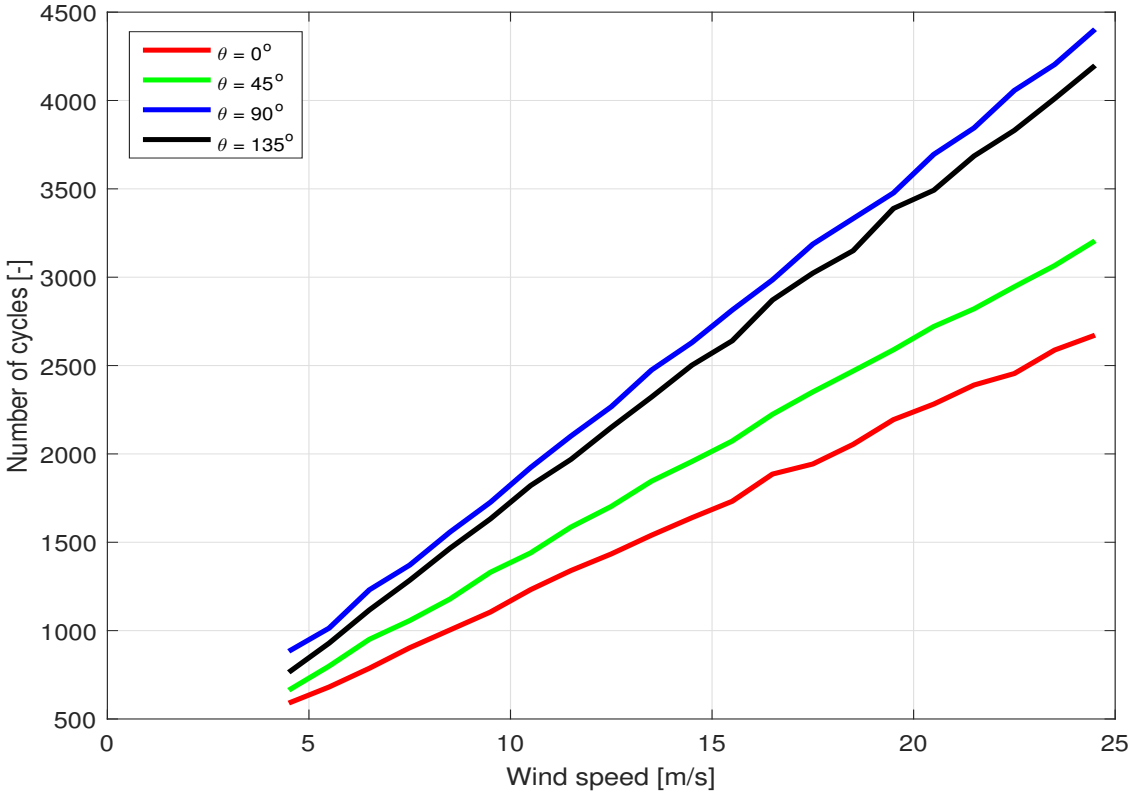

Figure 5.23: Variation of number of cycles of radial force with wind speed for different phase angles.

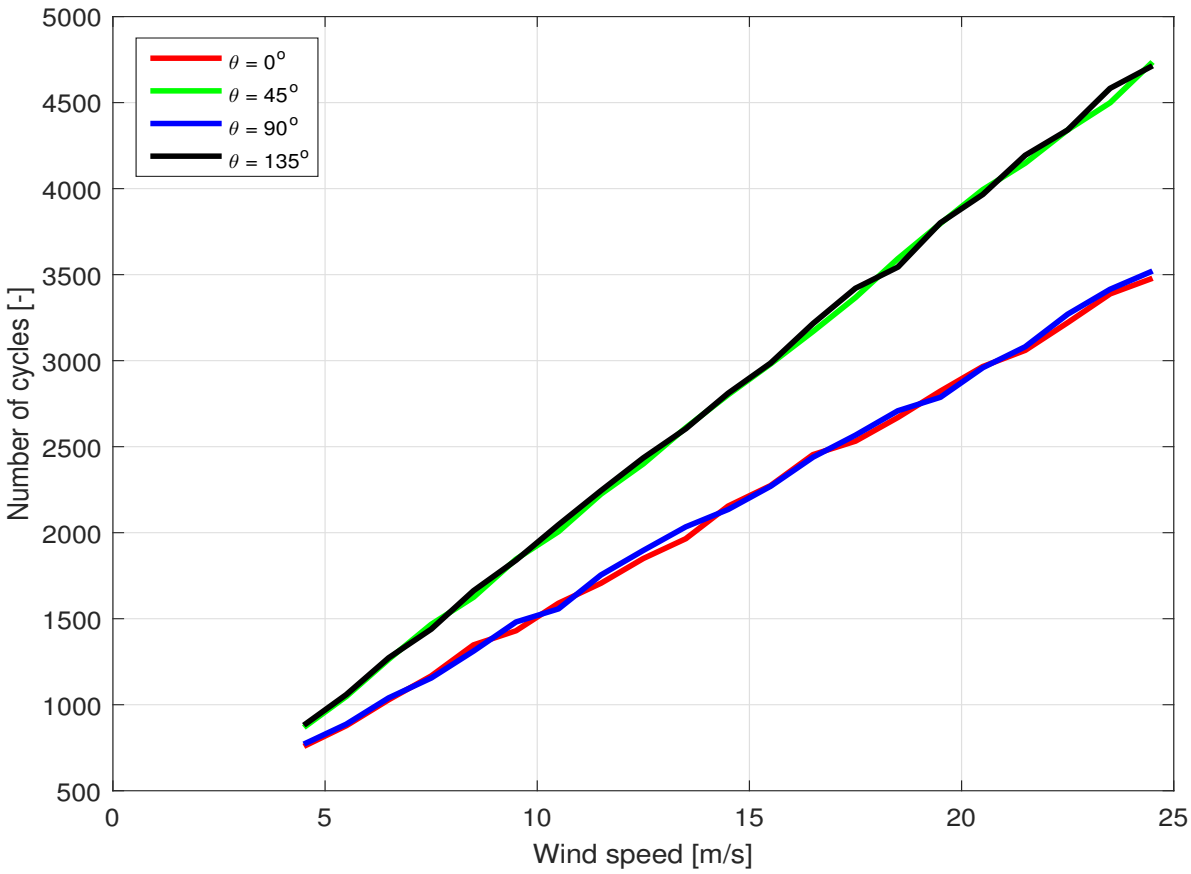

Figure 5.24: Variation of number of cycles of moment with wind speed for different phase angles.

The figures display the number of load cycles that occur in only one hour of the operation of the turbine. As mentioned earlier the number of load cycles in the complete lifetime of the turbine are likely to follow the same trend as the probability density function of the wind speed for the location of the turbine (see figure 3.3). Despite this, it is noteworthy that in one hour time simulations different loads vary with phase angle in no particular order.

5.5.2. VARIATION IN EQUIVALENT LOADS WITH WIND SPEED

The variation of equivalent tangential force, radial force, and the moment with wind speed for various phase angles can be seen in figures 5.25, 5.26, and 5.27 respectively. For the tangential force, the highest value of force was observed at the phase angle of 90^o. This was followed by the phase angles 45^o, 135^o, and 0^o respectively. A sudden decrease in the tangential force was observed around the rated wind when the phase angle was not zero. For 90^o angle, this change occurred at the wind speed of 11.5 m/s while for 45^o and 135^o angles this change was observed at wind speeds of 12.5 m/s and 13.5 m/s respectively.

For the radial force, the equivalent load followed the Gaussian distribution for non-zero phase angles. The peak of the distribution was at 12.5 m/s in all three cases. For 0^o phase angle the force kept increasing with the wind speed. This angle also had the highest value of the radial force followed by the phase angles of 135^o, 45^o, and 90^o.

In case of the moment, the loads for non-zero phase angle seem to follow the Gaussian distribution which is similar to the variation of radial forces. The peak of the variation also occurred at the wind speed of 12.5 m/s. However the peak values of the moments for non-zero phase angle were higher than the value of moment at 12.5 m/s wind speed for 0^o phase angle. Also, the variation of moment at 45^o and 135^o phase angles is almost the same.

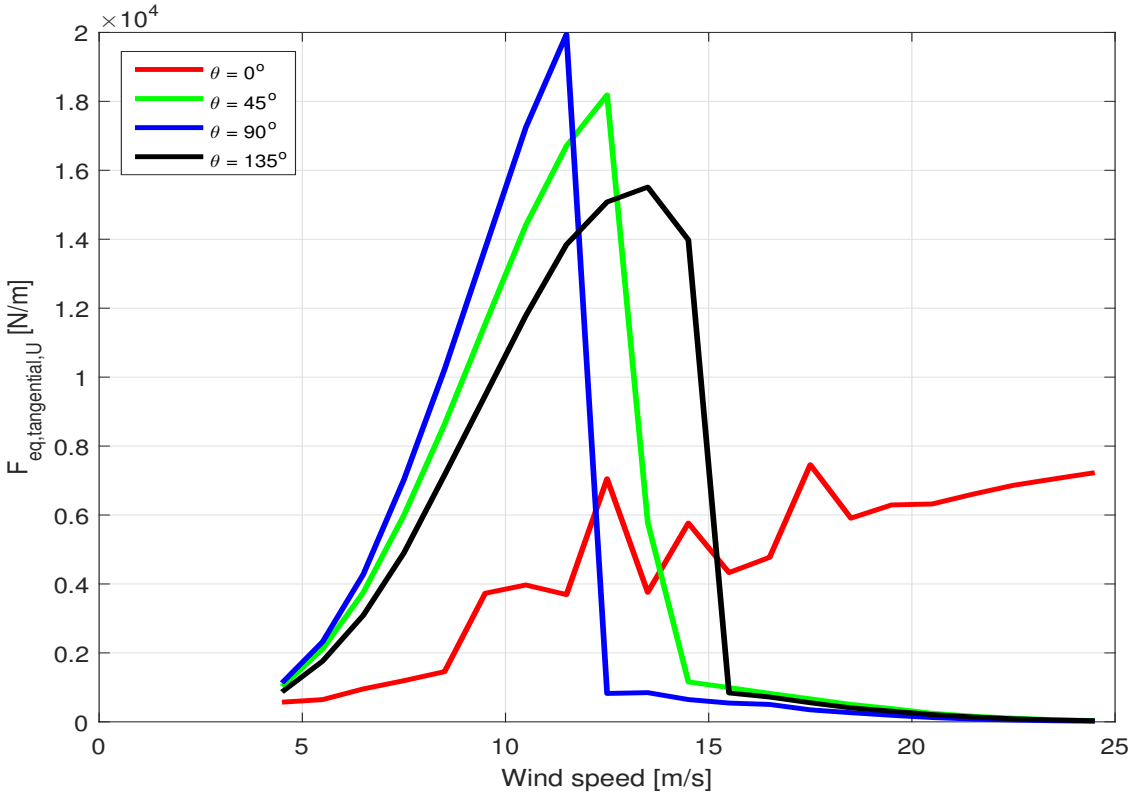

Figure 5.25: Variation of equivalent tangential force with wind speed for different phase angles.

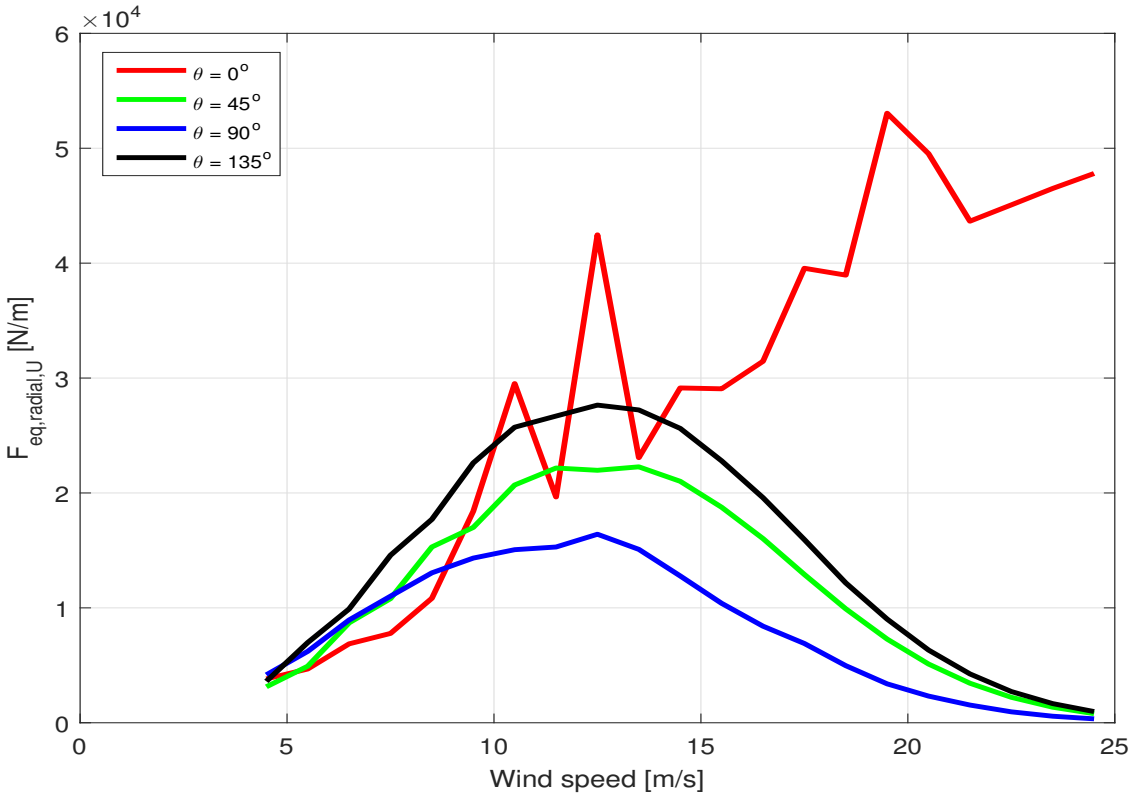

Figure 5.26: Variation of equivalent radial force with wind speed for different phase angles.

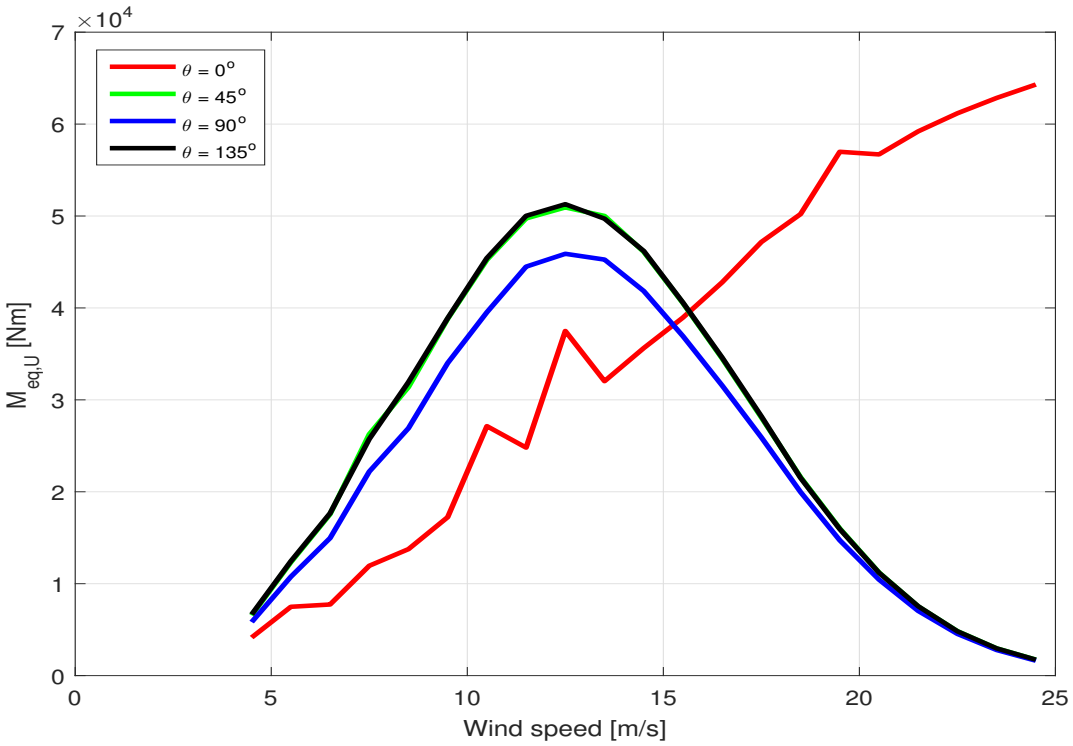

Figure 5.27: Variation of equivalent moment with wind speed for different phase angles.

5.5.3. VARIATION IN EQUIVALENT LOADS WITH PHASE ANGLE

Subsequently the equivalent loads due to all wind speeds were calculated using equation 4.10 for different phase angles. The change in equivalent tangential force, equivalent radial force and equivalent moment with phase angles can be seen in figures 5.28, 5.29, and 5.30 respectively. These changes were calculated using equation 4.12.

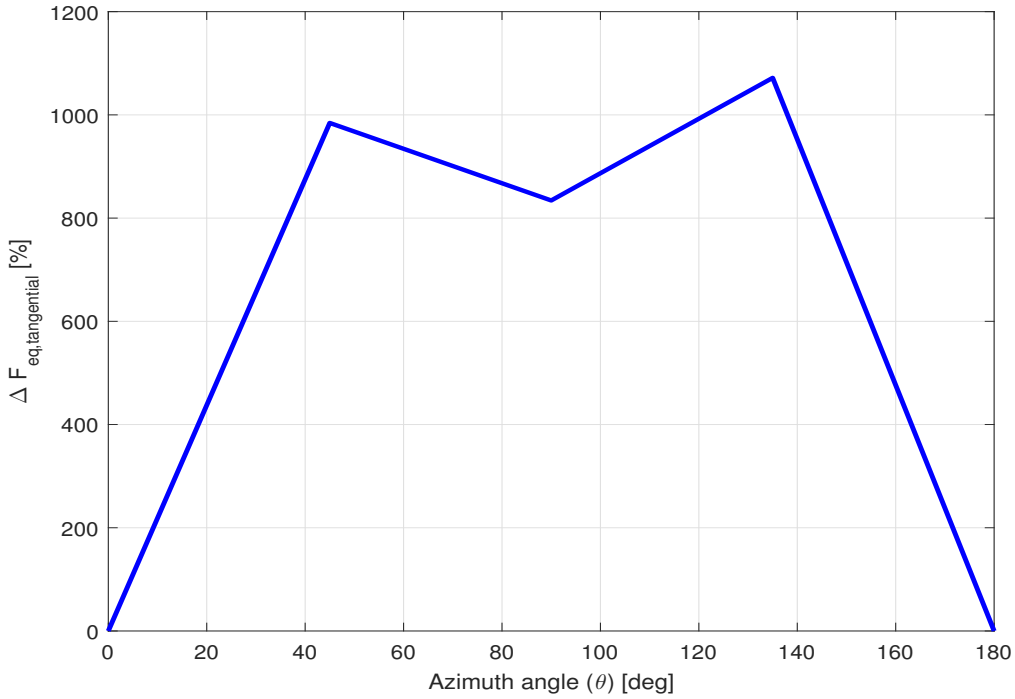

Figure 5.28: Variation equivalent tangential force with phase angle.

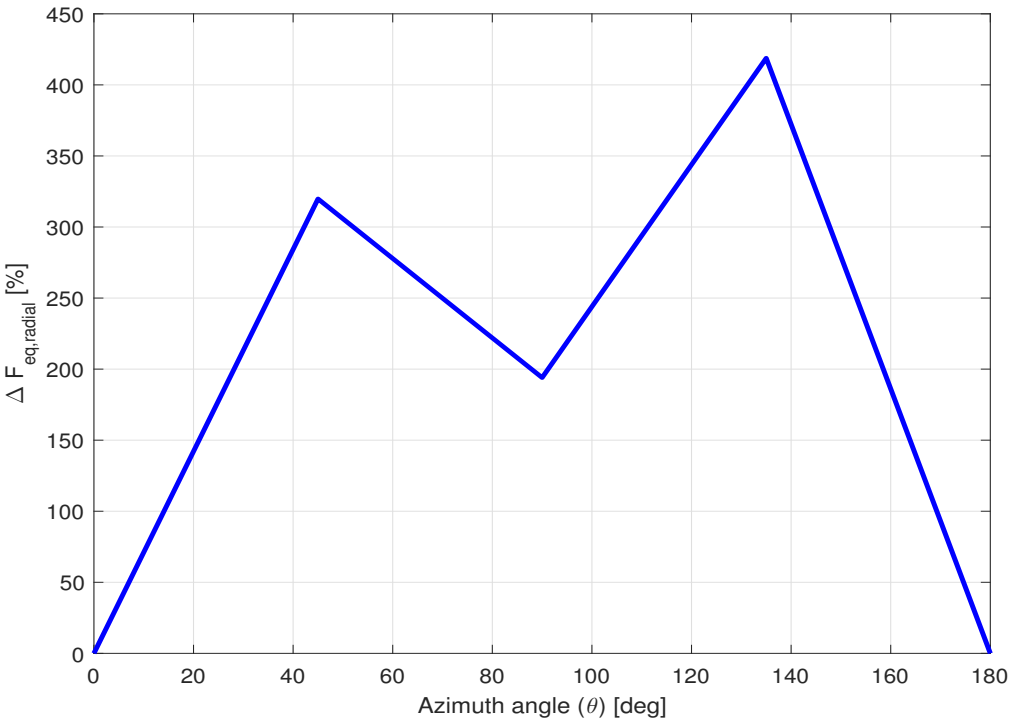

Figure 5.29: Variation equivalent radial force with phase angle.

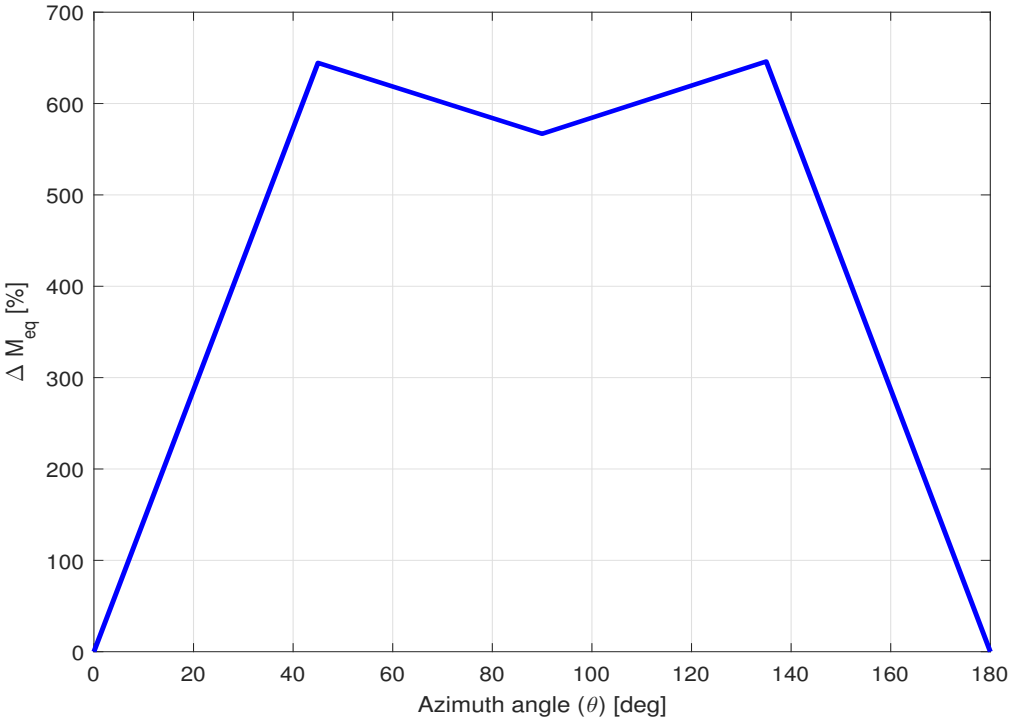

Figure 5.30: Variation equivalent moment with phase angle.

For all the three loads, the maximum change occurred at 135^o phase angle while the minimum change occurred at 90^o phase angle. The changes were quite high for all the non-zero phase angles. For the tangential force, the maximum change was around 1100%, while the minimum change was around 800%. For the radial force, the maximum change was around 425% while the minimum change was around 200%. For moment, the maximum change occurred at both 45^o and 135^o phase angles with a value of around 650%. The

minimum change in this case was around 580%.

The changes in the equivalent load values are alarmingly high and can cause serious damage to the turbine structures if the turbine operates at these angles for a long period of time. Conventionally, it has been said that there is no requirement of a yawing mechanism for VAWTs. But through the results of this study, it is clear that a yawing mechanism is required for VAWTs since the operation of the turbine at non-zero phase angles can lead to serious damage and reduce the lifetime of the turbine.

In actual offshore conditions, the measured average turbulence intensity is around 8% (Veldkamp, 2016). Therefore, at lower wind speeds, the turbulence intensity is far less than the values specified in the standard. Hence the results obtained in this study appear to be conservative and further investigations should be done to emulate the operation of the turbine under the influence of turbulent wind fields that resemble the turbulent wind occurring in the nature.

6

CONCLUSIONS

The ultimate aim of this study was to determine the response of a 2D VAWT to turbulence. For this purpose, the variation of loads on the turbine with constant wind and with turbulent wind were studied. A 5MW Darrieus VAWT model was selected for this study. This model was taken from the study conducted by Galinos (2015) since the model has been modified to reduce the large edgewise deflections at the equator of the turbine. For the completion of this study a broad range of aspects of load calculations and analysis was covered.

Firstly, some tools were developed to extract two dimensional turbulent wind fields from the three dimensional turbulent wind fields generated using the simulation tool TURBSIM. The turbulence model used in this study was the Normal Turbulence Model (NTM) which has been specified in the standard 'IEC 61400-1'. The two dimensional wind fields were again verified since they were extracted from a three dimensional wind field and it had to be made sure that they follow the same statistical models which are used to define the three dimensional models. All these processes were done in the program MATLAB.

After the generation of the required models, the simulations were performed on the 2D VAWT in the aeroelastic code U2DiVA. First the simulations were done using the constant wind and then the NTM. The time series of tangential and radial forces about the quarter chord points of the airfoils of the turbine were calculated from the time series of the streamwise and cross-streamwise forces that were received as output from U2DiVA. The time series of moment about the quarter chord point was also received from U2DiVA.

Next a post processor was developed in MATLAB to find the equivalent loads. For the calculation of the equivalent loads, rainflow counting of the time series had to be done in order to find the relevant load ranges. For this purpose, a rainflow counting program was developed in MATLAB using the algorithm specified in Downing and Socie (1982). The developed rainflow program and the post processor were verified against the post processing module of the commercial aeroelastic code 'GH-Bladed'.

To calculate the equivalent loads, first the equivalent loads at each wind speed were calculated using equation 4.9. After this, the total equivalent loads were calculated using equation 4.10 for different values of inverse slope (m) of the S-N curve of the material. Various peaks were observed at various wind speeds and it is recommended that a suitable control scheme to change the rotational velocity of the rotor should be used to avoid these peaks. Next, the changes in total equivalent loads under turbulent wind for different values of inverse slope were found out. It was found that the changes in total equivalent loads were less than 0.2% thus proving that the effect of turbulence on the fatigue life of VAWTs is quite small. It was also found out that the inverse slope value at which the change in equivalent loads is smallest is around 3. The material with this value of inverse slope is welded steel which due to its heaviness cannot be used for the manufacturing of wind turbine blades. The next material that could be used for this purpose is aluminium but past experiences with aluminium have shown that it is not reliable for such purposes (Sutherland *et al.*, 2012). Since the change in equivalent loads is low, the value of inverse slope chosen for the rest of this study was 10. This value is common for composites which are used to manufacture wind turbine blades since they can be tailored according to the loads and have high stiffness and strength (Sutherland, 1999).

Next the effect of phase angle on the loads was studied. For this purpose, the simulations were done with turbine in phase with the incoming wind. Four phase angles were used for this purpose. These angles were 0^o, 45^o, 90^o and 135^o. First the equivalent loads at each wind speed were calculated for each of these phase angles. For the radial force and the moment, the variation seemed to follow Gaussian distribution for phase angles of 45^o, 90^o and 135^o. After this the total equivalent loads were found out for each of these phase angles

and the changes in these loads were found out with respect to equivalent loads at 0^o phase angle. These changes were quite high and henceforth require a lot of attention. This also proves that operation of a VAWT in phase with the incoming wind is detrimental for the fatigue life of the VAWT and hence the possibility of a yawing mechanism for VAWTs cannot be neglected.

7

RECOMMENDATIONS FOR FURTHER RESEARCH

Aerodynamics of VAWTs have been a subject of research since the second half of last century and still continue to be a field with huge potential for research. This study has been an attempt to exploit this potential and based on the conclusions of this study further research can be done on the aerodynamics of VAWTs. The following points should be considered for this purpose:

1. The simulations in this study have been carried out using turbulent wind fields generated using only six different seeds. Although this is the minimum number of seeds recommended in the standard, a thorough understanding of response of VAWTs to turbulence is only possible when simulations are done using more number of turbulent wind fields generated using different seeds. The recommended number of seeds for this purpose is at least 100.

2. The forces and the moment were recorded at steps of 10^o of rotation of the turbine in this study. For a better understanding of the effect of turbulence on VAWTs, the step size should be reduced. A recommended value for this purpose is 2.5^o.

3. As mentioned earlier, the measured average turbulence intensity in offshore conditions is around 8%. Hence to obtain more realistic results, simulations should be done for this turbulence intensity at various wind speeds.

4. More simulations should be done using two dimensional models at various heights of the turbine so that the behaviour of the complete turbine under the influence of turbulence can be understood.

5. Some more phase angles can be used to study the effect of turbulence on the VAWTs when they are at phase with the incoming wind. This would further help in discovering the effect of phase angle on the fatigue life of the turbines.

6. More investigations should be done regarding the need for a yawing mechanism for VAWTs since in real time operation, the VAWTs are highly likely to be in phase with the incoming wind which may be detrimental for the fatigue life of the turbine.

7. The turbulence should be applied on the wake of turbine as well in order to understand the behaviour of the wake under the influence of turbulent wind.

8. For development of VAWT wind farms, multiple VAWT configurations should be simulated and the turbulence should be applied on the wake of VAWTs in these simulations. This should be done in order to understand the behaviour of wake in multiple VAWT configurations and the effect of wake of one turbine over the other.

A

LOAD SPECTRA FOR SOME WIND SPEEDS

The load spectra (for 20 years) for the wind speeds of 4.5 m/s, 8.5 m/s, 13.5 m/s, 18.5 m/s and 23.5 m/s can be seen in the following figures. It can be observed from the figures the number of cycles under the influence of turbulent wind field is quite high when compared to the number of cycles under the influence of constant wind. This difference is also seen to be increasing with increasing wind speed.

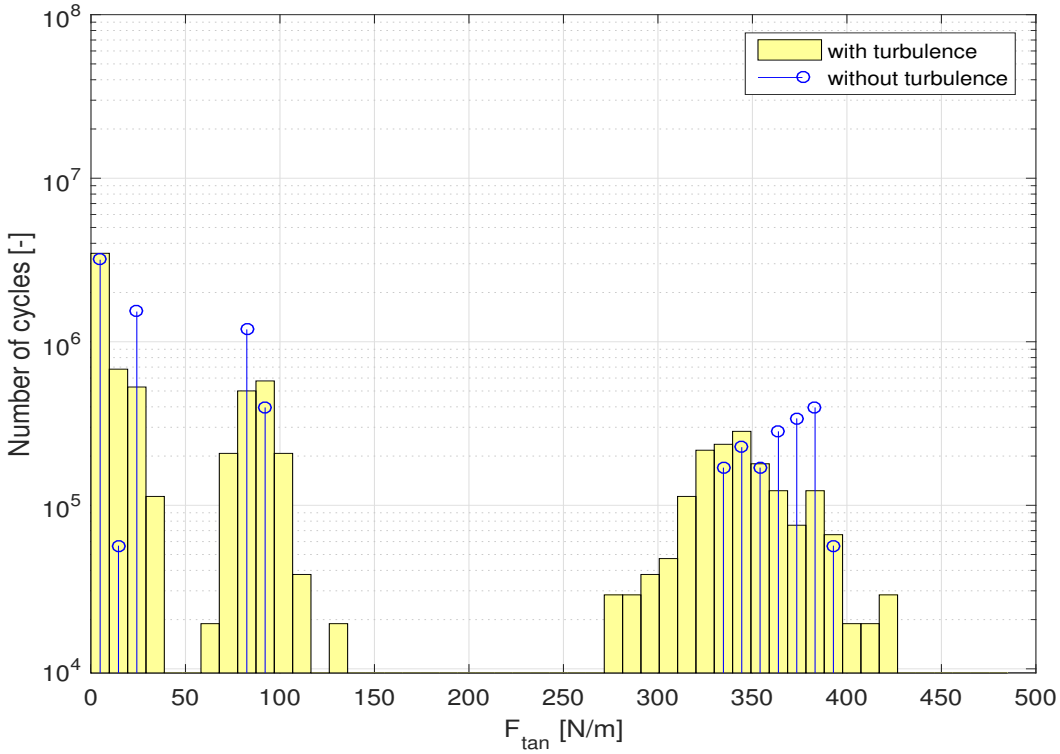

Figure A.1: Number of cycles of tangential force at wind speed of 4.5 m/s

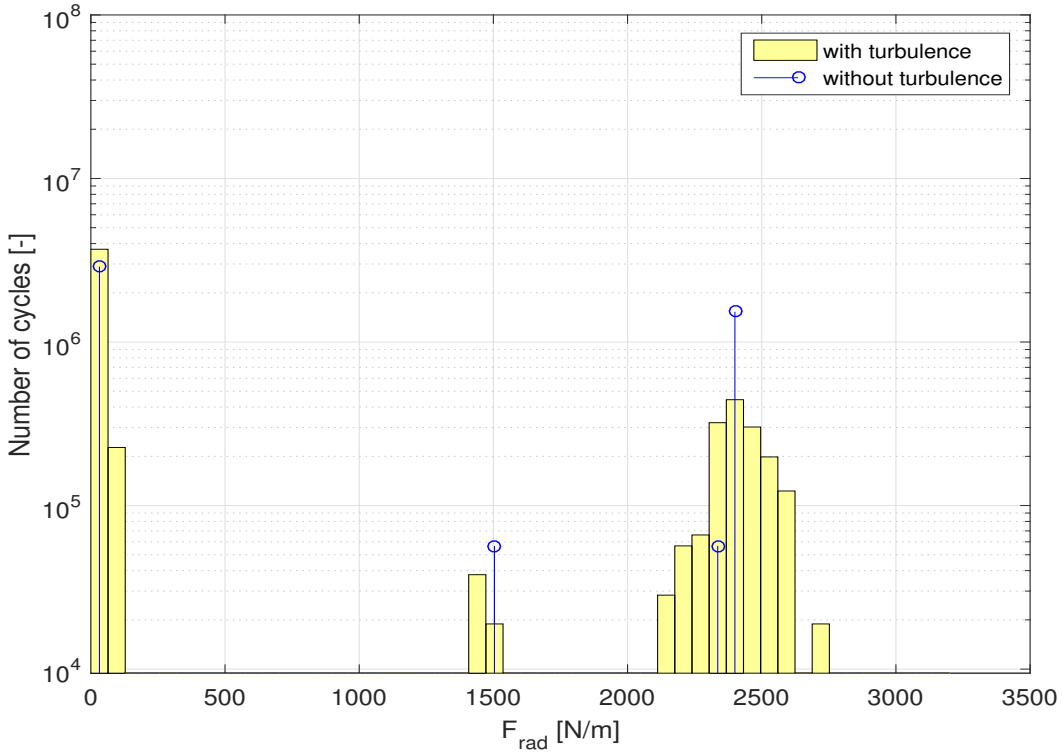

Figure A.2: Number of cycles of radial force at wind speed of 4.5 m/s

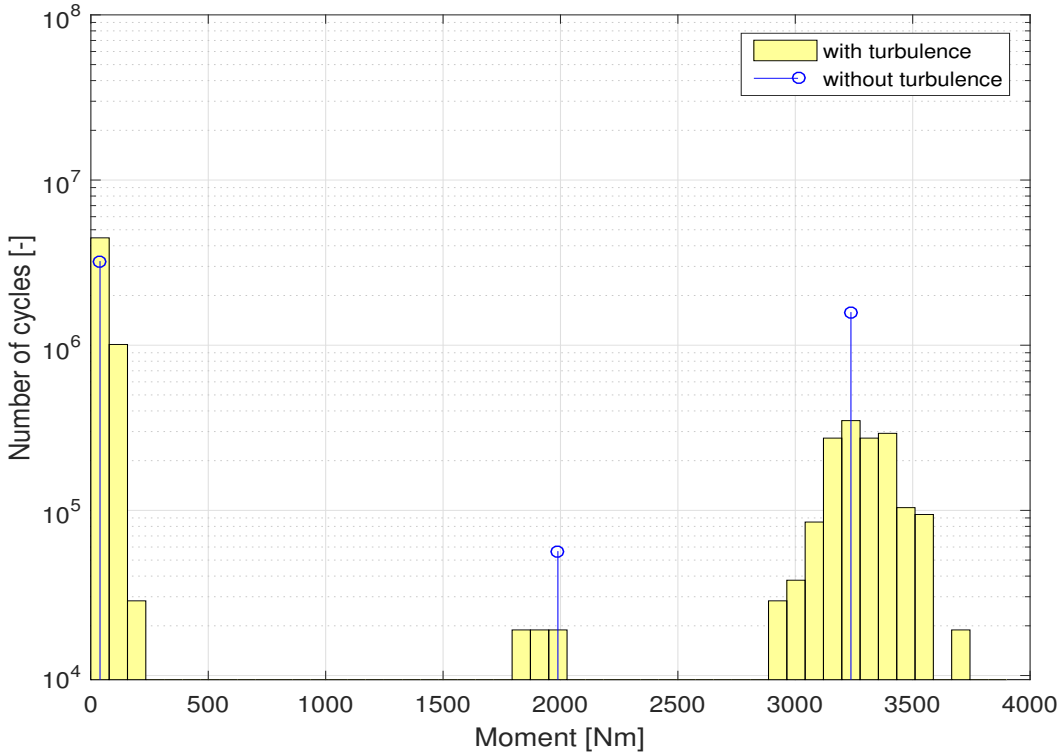

Figure A.3: Number of cycles of moment at wind speed of 4.5 m/s

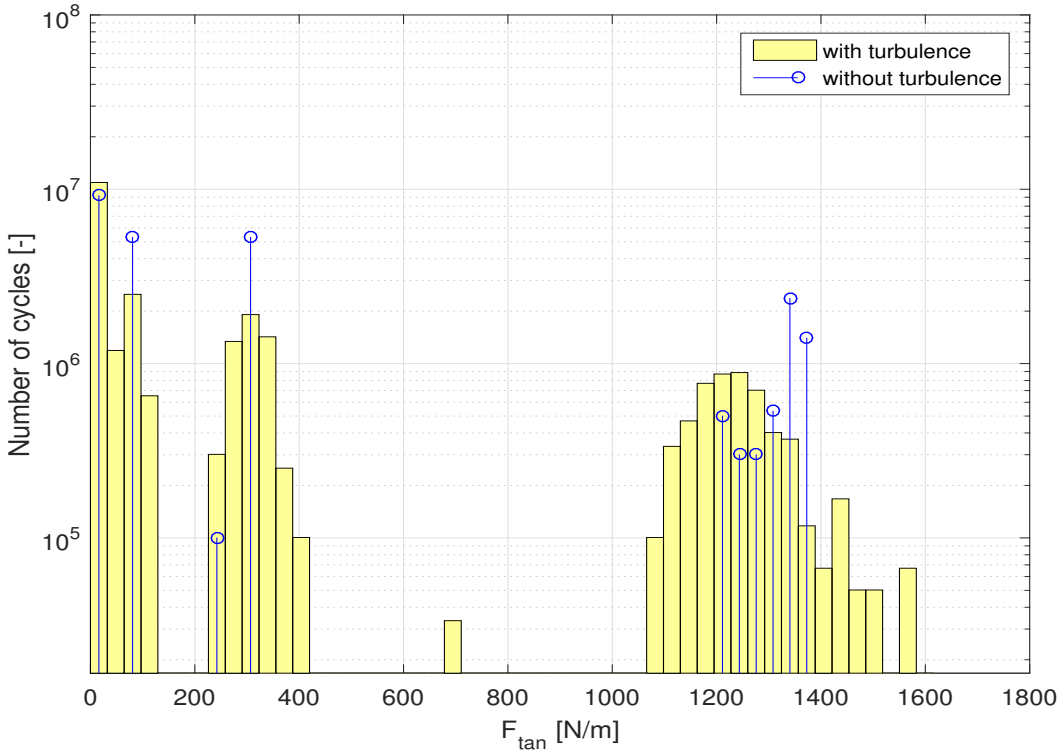

Figure A.4: Number of cycles of tangential force at wind speed of 8.5 m/s

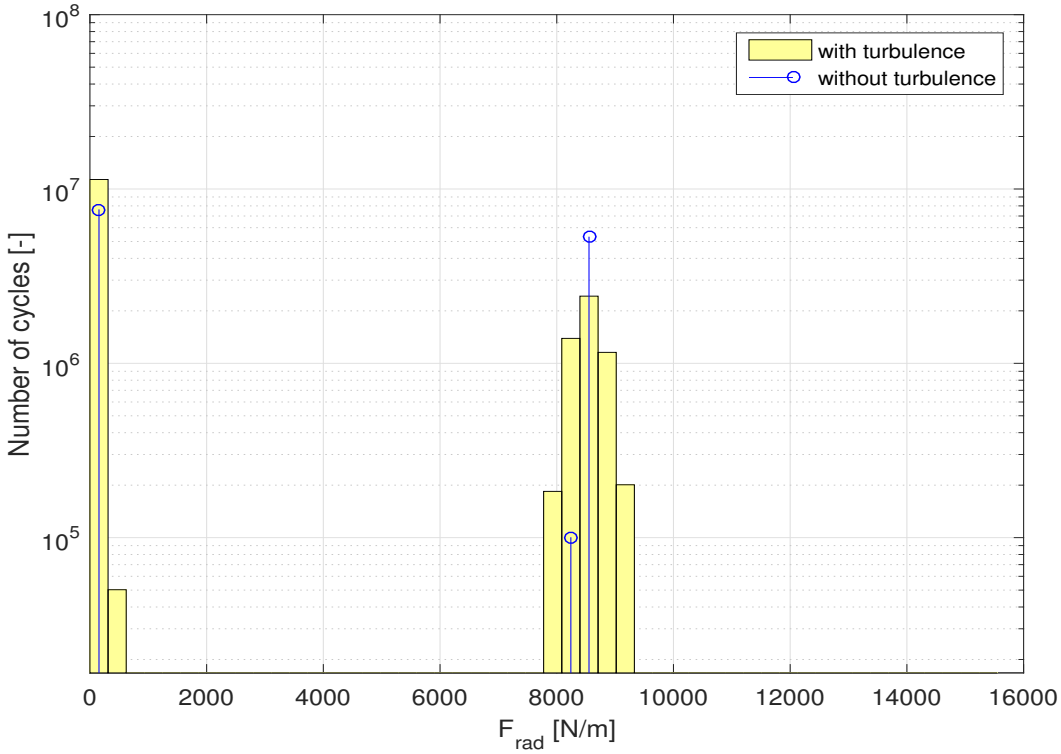

Figure A.5: Number of cycles of radial force at wind speed of 8.5 m/s

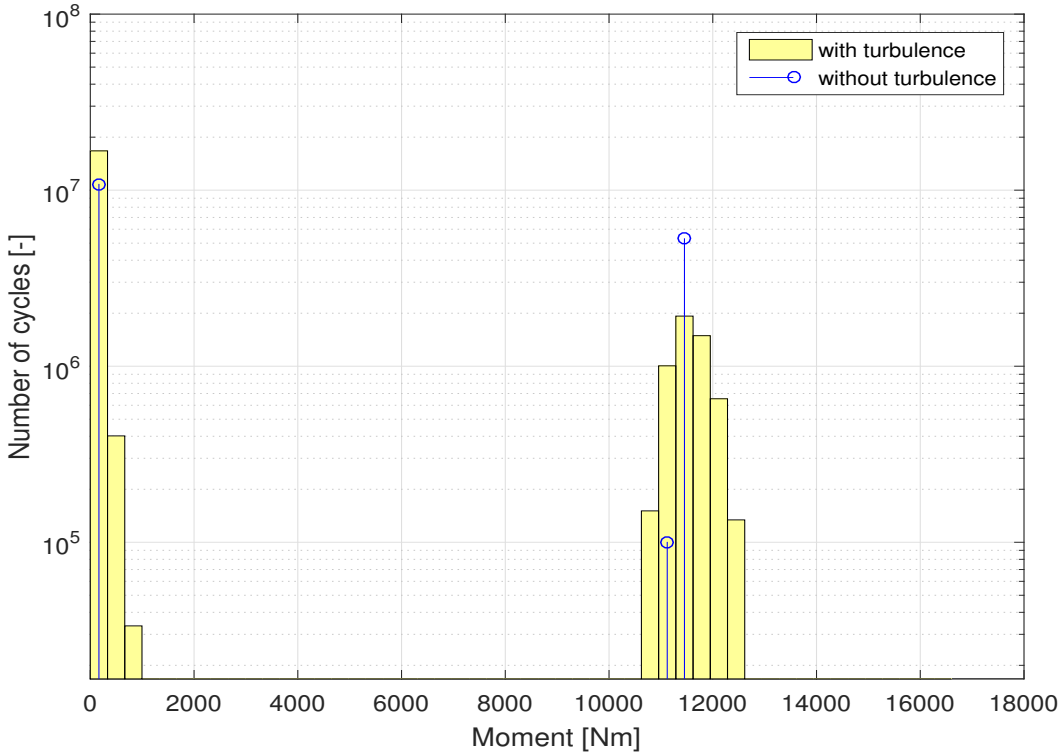

Figure A.6: Number of cycles of moment at wind speed of 8.5 m/s

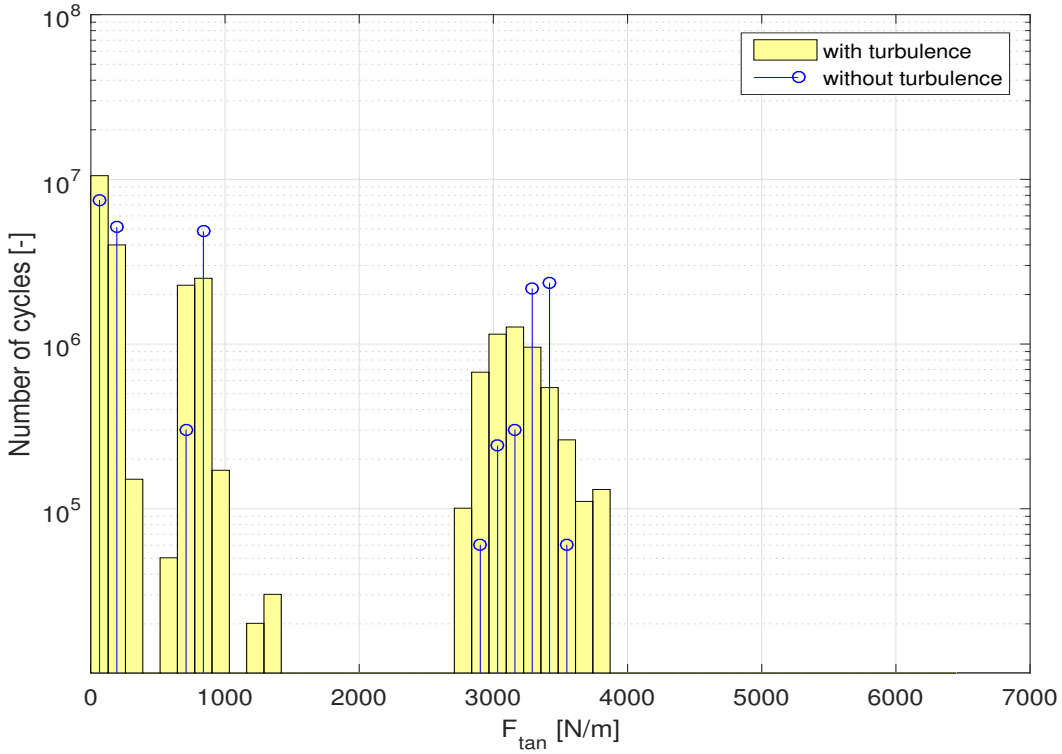

Figure A.7: Number of cycles of tangential force at wind speed of 13.5 m/s

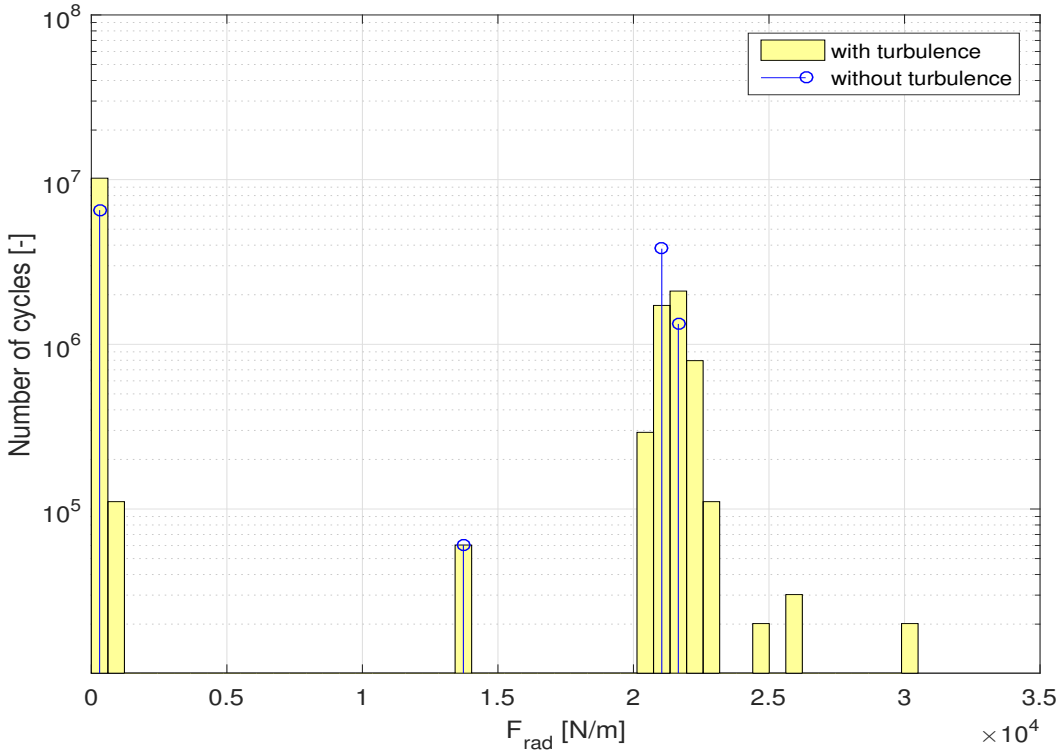

Figure A.8: Number of cycles of radial force at wind speed of 13.5 m/s

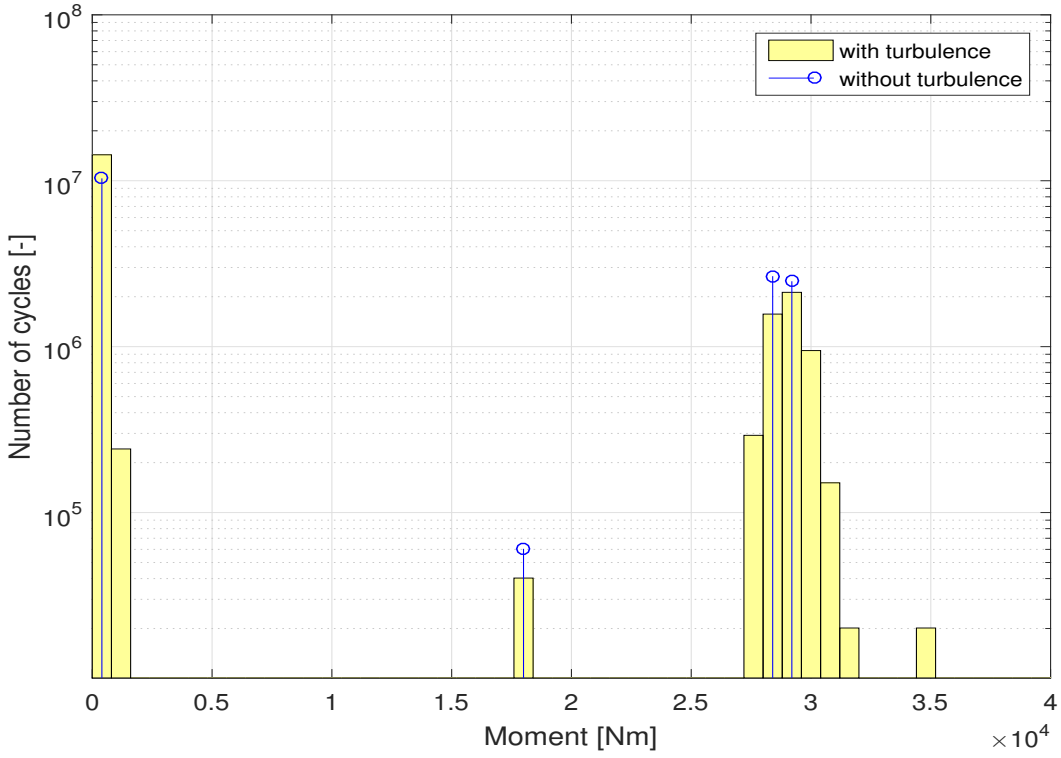

Figure A.9: Number of cycles of moment at wind speed of 13.5 m/s

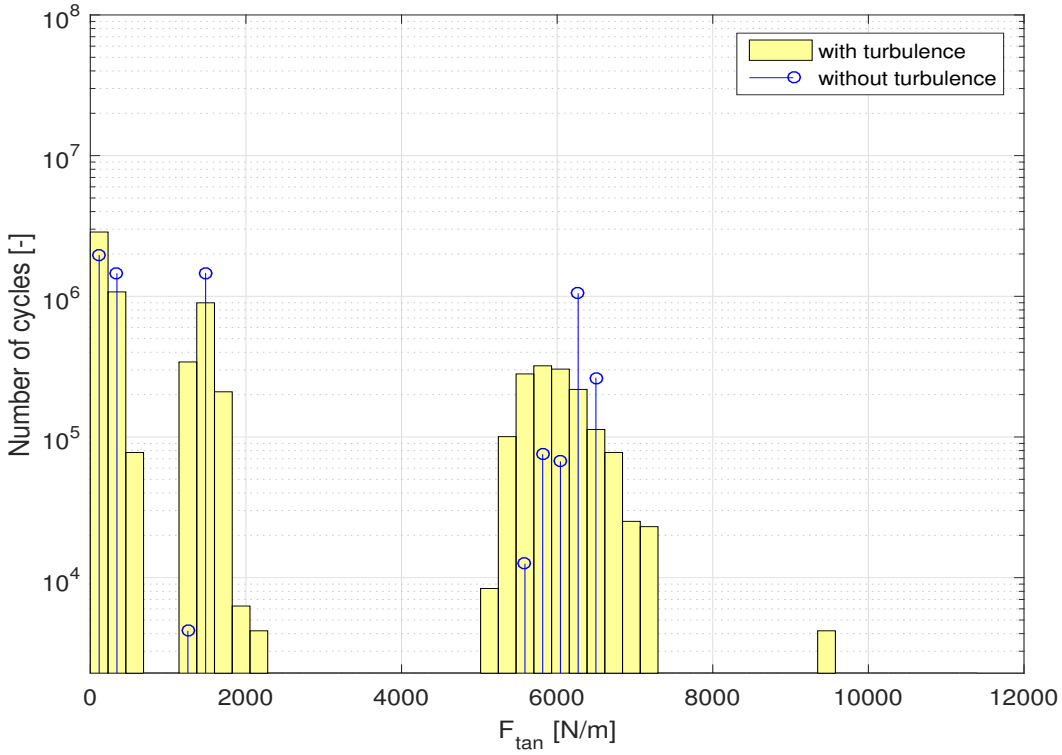

Figure A.10: Number of cycles of tangential force at wind speed of 18.5 m/s

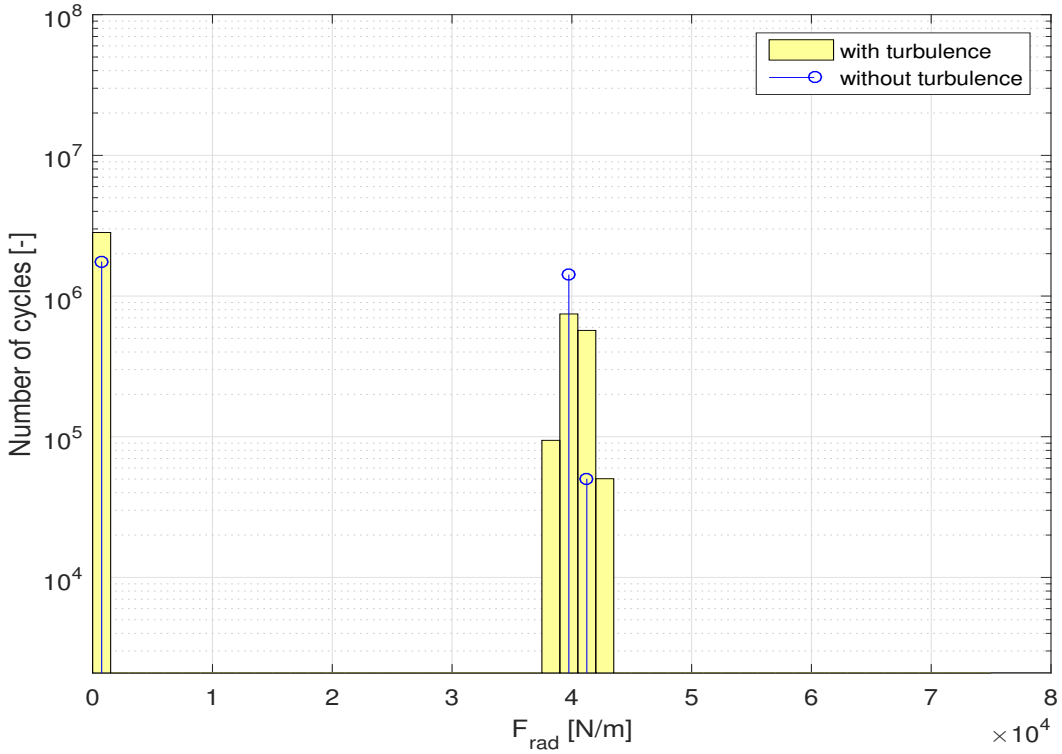

Figure A.11: Number of cycles of radial force at wind speed of 18.5 m/s

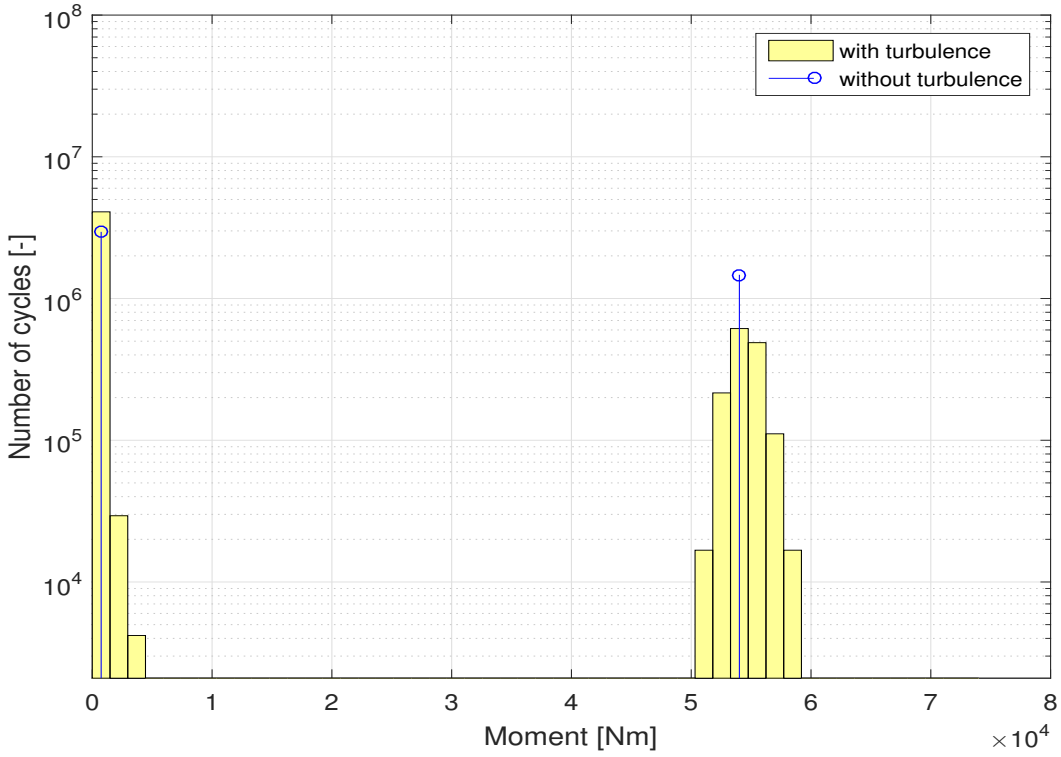

Figure A.12: Number of cycles of moment at wind speed of 18.5 m/s

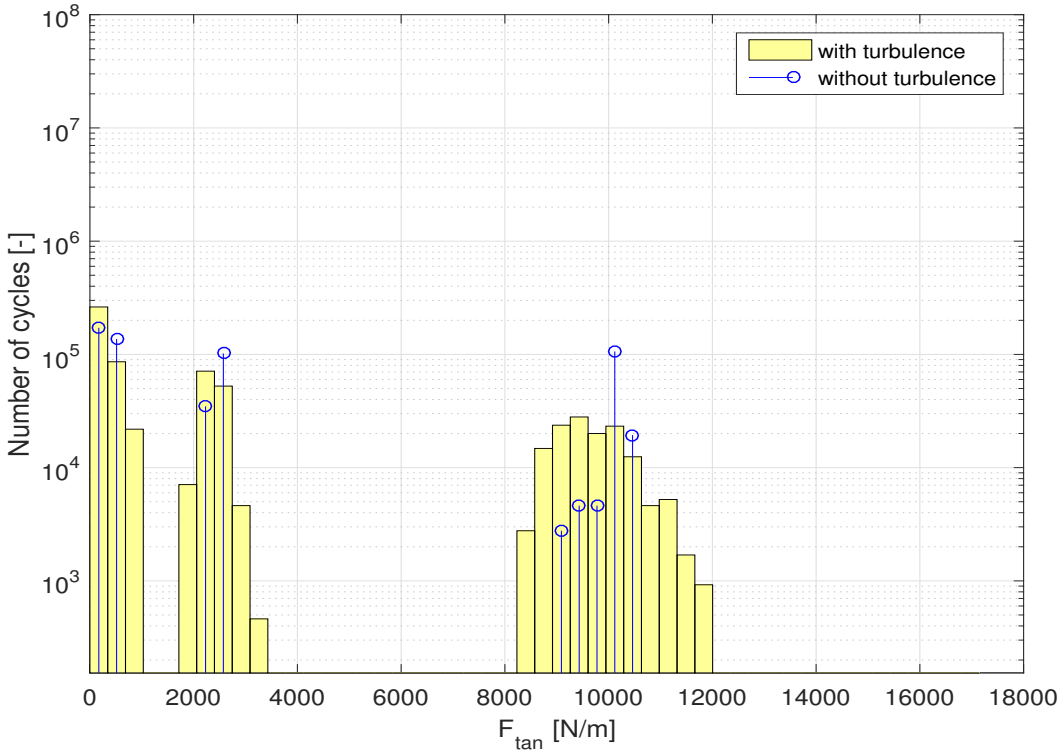

Figure A.13: Number of cycles of tangential force at wind speed of 23.5 m/s

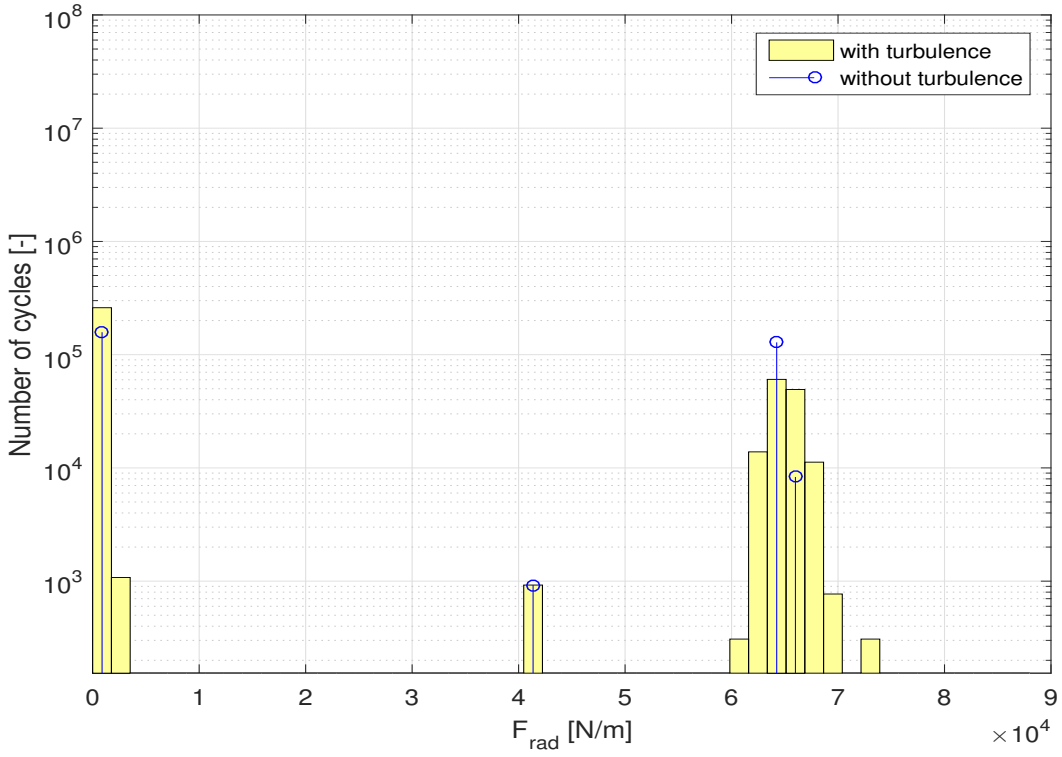

Figure A.14: Number of cycles of radial force at wind speed of 23.5 m/s

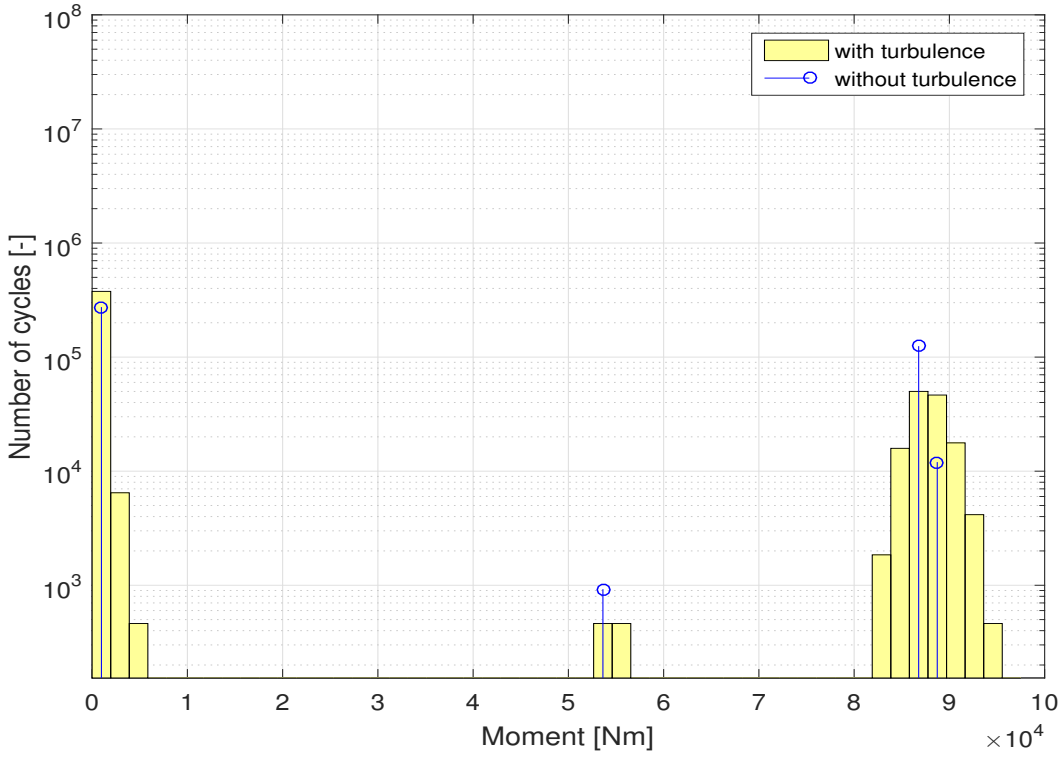

Figure A.15: Number of cycles of moment at wind speed of 23.5 m/s

The Root Mean Square (RMS) values for the time series of wind speed and loads at the rated wind speed

(13.5 m/s) were also calculated. The RMS values were calculated as follows:

$$RMS = \sqrt{\frac{1}{N}\sum_{i=1}^{N} x_i^2} \tag{A.1}$$

In the above equation N is the number of time steps in the time series and for wind speed, x is defined as:

$$x_i = u(i) - u_{rated} \tag{A.2}$$

Whereas for the loads, x is defined as follows:

$$x_i = F(i)_t - F(i)_{wt} \tag{A.3}$$

In the above equation $F(i)_t$ denotes load at time step 'i' under the influence of turbulence whereas $F(i)_t$ denotes load at the same time step under the influence of constant wind. Following were the RMS values obtained for the rated wind speed:

Table A.1: RMS values of wind speed and loads at the rated wind speed

Parameter	**RMS value**
Wind Speed	1.77 m/s
Tangential Force	120.4 N/m
Radial Force	356.47 N/m
Moment	416.45 N/m

B

COVARIANCE OF WIND SPEED AT THREE POINTS

The covariance of time series of wind velocity components at the three points discussed in chapter 4 was also found out. The covariance matrices for various wind speeds are as follows: For horizontal component of wind velocity at point 1 and point 2 at wind speed of 4.5 m/s:

$$\begin{bmatrix} 0.99 & 0.73 \\ 0.73 & 0.97 \end{bmatrix}$$

For horizontal component of wind velocity at point 1 and point 3 at wind speed of 4.5 m/s:

$$\begin{bmatrix} 0.99 & 0.19 \\ 0.19 & 0.75 \end{bmatrix}$$

For horizontal component of wind velocity at point 1 and point 2 at wind speed of 13.5 m/s:

$$\begin{bmatrix} 3.37 & 2.47 \\ 2.47 & 3.14 \end{bmatrix}$$

For horizontal component of wind velocity at point 1 and point 3 at wind speed of 13.5 m/s:

$$\begin{bmatrix} 3.37 & 0.71 \\ 0.71 & 2.84 \end{bmatrix}$$

For horizontal component of wind velocity at point 1 and point 2 at wind speed of 24.5 m/s:

$$\begin{bmatrix} 7.85 & 6 \\ 6 & 7.89 \end{bmatrix}$$

For horizontal component of wind velocity at point 1 and point 3 at wind speed of 24.5 m/s:

$$\begin{bmatrix} 7.85 & 1.74 \\ 1.74 & 8.09 \end{bmatrix}$$

For lateral component of wind velocity at point 1 and point 2 at wind speed of 4.5 m/s:

$$\begin{bmatrix} 0.38 & 0.27 \\ 0.27 & 0.52 \end{bmatrix}$$

For lateral component of wind velocity at point 1 and point 3 at wind speed of 4.5 m/s:

$$\begin{bmatrix} 0.38 & 0.04 \\ 0.04 & 0.58 \end{bmatrix}$$

For lateral component of wind velocity at point 1 and point 2 at wind speed of 13.5 m/s:

$$\begin{bmatrix} 2.48 & 2.08 \\ 2.08 & 2.69 \end{bmatrix}$$

For lateral component of wind velocity at point 1 and point 3 at wind speed of 13.5 m/s:

$$\begin{bmatrix} 2.48 & 0.84 \\ 0.84 & 2.75 \end{bmatrix}$$

For lateral component of wind velocity at point 1 and point 2 at wind speed of 24.5 m/s:

$$\begin{bmatrix} 5.45 & 4.33 \\ 4.33 & 5.58 \end{bmatrix}$$

For lateral component of wind velocity at point 1 and point 3 at wind speed of 24.5 m/s:

$$\begin{bmatrix} 5.45 & 1.99 \\ 1.99 & 7.12 \end{bmatrix}$$

From the above matrices, it can be observed that the values of covariance matrix for points 1 and 2 are higher than the corresponding values for points 1 and 19. This means that the time series at points 1 and 2 are more similar to each other when compared to the time series at points 1 and 19. This supports the

BIBLIOGRAPHY

J. F. Manwell, J. G. McGowan, and A. L. Rogers, *Wind Energy Explained* (John Wiley and Sons Ltd., 2009).

TelnosNet web development, *Gedser wind turbine,* http://telosnet.com/wind/20th.html (2015), [Accessed: 15-March-2016].

H. J. Sutherland, T. D. Ashwill, and D. E. Berg, *A retrospective of VAWT technology*, Tech. Rep. (HJS consulting and Wind Energy Technologies Department, Sandia National Laboratories, 2012).

Netzero guide, *Savonius wind turbine,* http://netzeroguide.com/savonius-wind-turbine.html (2013), [Accessed: 18-May-2016].

Makcan Resources Corporation, *Darrieus vawt image source,* http://makcan.ca/solutions/energy-solutions/renewable-energy/wind-power/ (2015), [Accessed: 20-May-2016].

W. Tjiu, T. Marnoto, S. Mat, M. H. Ruslan, and K. Sopian, *Darrieus vertical axis wind turbine for power generation I: Assessment of Darrieus VAWT configurations,* Renewable Energy **75**, 50 (2015a).

X. Jin, G. Zhao, K. Gao, and W. Ju, *Darrieus vertical axis wind turbine: Basic research methods,* Renewable and Sustainable Energy Reviews **42**, 212 (2015).

M. Islam, D. S. K. Ting, and A. Fartaj, *Aerodynamic models for darrieus-type straight-bladed vertical axis wind turbines,* Renewable and Sustainable Energy Reviews **12**, 1087 (2008).

R. Lanzafame, S. Mauro, and M. Messina, *2D CFD modeling of H-Darrieus wind turbines using a transition turbulence model,* Energy Procedia **45**, 131 (2014).

C. Li, S. Zhu, Y. Xu, and Y. Xiao, *2.5D large eddy simulation of vertical axis wind turbine in consideration of high angle of attack flow,* Renewable Energy **51**, 317 (2013).

R. Howell, N. Qin, J. Edwards, and N. Durrani, *Wind tunnel and numerical study of a small vertical axis wind turbine,* Renewable Energy **35(2)**, 412 (2010).

Q. Li, T. Maeda, Y. Kamada, J. Murata, K. Furukawa, and M. Yamamoto, *Effect of number of blades on aerodynamic forces on a straight-bladed vertical axis wind turbine,* Energy **90**, 784 (2015).

M. Ahmadi-Baloutaki, R. Carriveau, and D. S. K. Ting, *Performance of a vertical axis wind turbine in grid generated turbulence,* Sustainable Energy Technologies and Assessments **11**, 178 (2015).

N. Fujisawa and M. Takeuchi, *Flow visualization and piv measurement of flow field around a darrieus rotor in dynamic stall,* Journal of Visualization **1(4)**, 379 (1999).

C. S. Ferreira, G. van Kuik, G. van Bussel, and F. Scarano, *Visualization by piv of dynamic stall on a vertical axis wind turbine,* Experiments in Fluids **46(1)**, 97 (2009).

G. Tescione, D. Ragni, C. He, C. J. Simão Ferreira, and G. J. W. van Bussel, *Near wake flow analysis of a vertical axis wind turbine by stereoscopic particle image velocimetry,* Renewable Energy **70**, 47 (2014).

Y. Li, K. Tagawa, and W. Liu, *Performance effects of attachment on blade on a straight-bladed vertical axis wind turbine,* Current Applied Physics **10**, S335 (2010).

J. D. Anderson,Jr., *Fundamentals of Aerodynamics - third edition*, McGraw-Hill Series in Aeronautical and Aerospace Engineering (McGraw-Hill Education, 2001).

J. Katz and A. Plotkin, *Low-Speed Aerodynamics - second edition*, Cambridge Aerospace Series (Book 13) (Cambridge University Press, 2000).

K. O. Merz, *A method for analysis of vawt aerodynamic loads under turbulent wind and platform motion,* Energy Procedia **24**, 44 (2012).

P. Gipe, *Èole darrieus vawt,* http://www.wind-works.org/cms/index.php?id=506 (2016), [Accessed: 5-October-2016].

T. Nakamura, K. Mizumukai, H. Akimoto, Y. Hara, and T. Kawamura, *Floating axis wind and water turbine for high utilization of sea surface area: Design of sub-megawatt prototype turbine,* in *Proceedings of the ASME 2013 32nd International Conference on Ocean, Offshore and Arctic Engineering (OMAE2013), June 9-14, 2013, Nantes, France* (2013).

M. Cahay, E. Luquiau, C. Smadja, and F. Silvert, *Use of a vertical wind turbine in an offshore floating wind farm,* in *Proceedings of the 2011 Offshore Technology Conference (OTC2011), May 2-5, 2011, Houston, Texas, USA* (2011).

W. Tjiu, T. Marnoto, S. Mat, M. H. Ruslan, and K. Sopian, *Darrieus vertical axis wind turbine for power generation II: Challenges in HAWT and the opportunity of multi-megawatt Darrieus VAWT development,* Renewable Energy **75**, 560 (2015b).

J. O. Dabiri, *Potential order-of-magnitude enhancement of wind farm power density via counter-rotating vertical-axis wind turbine arrays,* Journal of renewable and sustainable energy **3**, 043104 (2011).

DeepWind, *The deepwind project,* http://www.deepwind.eu/the-deepwind-project (2014), [Accessed: 15-July-2016].

P. Carlone, I. Baran, J. H. Hattel, and G. S. Palazzo, *Computational approaches for modeling the multiphysics in pultrusion process,* Advances in Mechanical Engineering **5**, 301875 (2013).

S. Barth and P. J. Eecen, *Description of the relation of Wind, Wave and Current Characteristics at the Offshore Wind Farm Egmond aan Zee (OWEZ) Location in 2006*, Tech. Rep. (Energieonderzoek Centrum Nederland ECN, 2006).

B. J. Jonkman, *TurbSim User's Guide: Version 1.50*, Tech. Rep. (National Renewable Energy Laboratory NREL, 2009).

D. R. Verelst, H. Aagaard Madsen, K. A. Kragh, and F. Belloni, *Detailed Load Analysis of the baseline 5MW DeepWind Concept*, Tech. Rep. (DTU Wind Energy, 2014).

C. Galinos, *Study of Design Load Cases for Multi- Megawatt Onshore Vertical Axis Wind Turbines*, Master's thesis, Technical University of Denmark (DTU) (2015).

International Electrotechnical Commission, *IEC 61400-1 ed.3: Wind turbines - part 1: Design requirements,* (2005).

UNFCCC, *Report on the conference of the parties on its fifteenth session, held in copenhagen from 7 to 19 december 2009,* United Nations Framework Convention on Climate Change (UNFCCC) (2009).

T. Pulles, *Will the world meet the climate change challenge?* Carbon Management **6:1-2**, 1 (2015).

T. Burton, D. Sharpe, N. Jenkins, and E. Bossanyi, *Wind Energy Handbook* (John Wiley and Sons Ltd., 2001).

M. Zaaijer, *Lecture slides: Introduction to wind energy,* Delft University of Technology (2014).

EWEA, *Wind in power: 2015 European statistics*, Tech. Rep. (The European Wind Energy Association (EWEA), 2016).

D. W. Wekesa, C. Wang, Y. Wei, J. N. Kamau, and L. A. M. Danao, *A numerical analysis of unsteady inflow wind for site specific vertical axis wind turbine: A case study for marsabit and garissa in kenya,* Renewable Energy **76**, 648 (2015).

C. S. Ferreira, G. van Bussel, and G. van Kuik, *Wind Tunnel Hotwire Measurements, Flow Visualization and Thrust Measurement of a VAWT in skew,* Journal of Solar Energy Engineering **128**, 487 (2006).

N. Durrani, N. Qin, H. Hameed, and S. Khushnood, *2D numerical analysis of a VAWT wind farm for different configurations,* in 49th *AIAA Aerospace Sciences Meeting including the New Horizons Forum and Aerospace Exposition 4 - 7 January 2011, Orlando, Florida, USA* (2011).

K. Kacprzak, L. Grzegorz, and K. Sobczak, *Numerical investigation of conventional and modified savonius wind turbines,* Renewable Energy **60**, 578 (2013).

V. J. Modi and M. S. U. K. Fernando, *On the performance of the savonius wind turbine,* Journal of Solar Energy Engineering **111(1)**, 71 (1989).

S. C. McIntosh, H. Babinsky, and G. Bertényi, *Optimizing the energy output of vertical axis wind turbines for fluctuating wind conditions,* in 45th *AIAA Aerospace Sciences Meeting and Exhibit 8 - 11 January 2007, Reno, Nevada* (2007).

S. C. McIntosh, H. Babinsky, and G. Bertényi, *Unsteady power output of vertical axis wind turbines operating within a fluctuating free-stream,* in 46th *AIAA Aerospace Sciences Meeting and Exhibit 7 - 10 January 2008, Reno, Nevada* (2008).

L. M. Danao, O. Eboibi, and R. Howell, *An experimental investigation into the influence of unsteady wind on the performance of a vertical axis wind turbine,* Applied Energy **107**, 403 (2013).

M. J. Edwards, L. M. Danao, and R. J. Howell, *Novel experimental power curve determination and computational methods for the performance analysis of vertical axis wind turbines,* Journal of Solar Energy Engineering **134(3)**, 11 (2012).

J. B. Fanucci and R. E. Walter, *Innovative wind machines: the theoretical performance of a vertical axis wind turbine,* in *Proceedings of the vertical-axis wind turbine technology workshop, Sandia laboratories, SAND 76-5586, USA* (1976) pp. iii–61–95.

J. H. Strickland, B. T. Webster, and T. Nguyen, *A vortex model of the darrieus turbine: an analytical and experimental study,* Journal of Fluid Engineering **101**, 500 (1979).

T. Kawamura and Y. Sato, *Numerical simulation of the flow around a cross-flow wind turbine,* Research Institute of Mathematical Science, Kyoto University,Japan **1288(5)**, 44 (2002).

R. M. Cummings, J. R. Forsythe, S. A. Morton, and K. D. Squires, *Computational challenges in high angle of attack flow prediction,* Progress in Aerospace Sciences **39(5)**, 369 (2003).

H. Gao, H. Hui, and Z. J. Wang, *Computational study of unsteady flows around dragonfly and smooth airfoils at low reynolds numbers,* in 46th *AIAA Aerospace Sciences Meeting and Exhibit 7 - 10 January 2008, Reno, Nevada* (2008).

M. Islam, D. S. K. Ting, and A. Fartaj, *Large eddy simulation of wind loads on a long-span spatial lattice roof,* Wind and Structures **13(1)**, 57 (2010).

H. M. Mohamed, *Aero-acoustics noise evaluation of H-rotor darrieus wind turbines,* Energy **65**, 596 (2014).

C. S. Ferreira, G. van Bussel, and G. van Kuik, *2D CFD simulation of dynamic stall on a vertical axis wind turbine: Verification and validation with PIV measurements,* in 44th *AIAA Aerospace Sciences Meeting and Exhibit 8 - 11 January 2007, Reno, Nevada* (2007).

S. Wang, D. B. Ingham, L. Ma, M. Pourkashanian, and Z. Tao, *Numerical investigations on dynamic stall of low reynolds number flow around oscillating airfoils,* Computers and Fluids **29(9)**, 1529 (2010).

K. M. Almohammadi, D. B. Ingham, L. Ma, and M. Pourkashanian, *Computational fluid dynamics (CFD) mesh independency techniques for a straight blade vertical axis wind turbine,* Energy **58**, 483 (2013).

R. Nobile, M. Vahdati, J. F. Barlow, and A. Mewburn-Crook, *Unsteady flow simulation of a vertical axis augmented wind turbine: A two-dimensional study,* Journal of Wind Engineering and Industrial Aerodynamics **125**, 168 (2014).

J. McNaughton, F. Billard, and A. Revell, *Turbulence modelling of low reynolds number flow effects around a vertical axis turbine at a range of tip-speed ratios,* Journal of Fluids and Structures **47**, 124 (2014).

M. R. Castelli, A. Englaro, and E. Benini, *The Darrieus wind turbine: Proposal for a new performance prediction model based on CFD,* Energy **36(8)**, 4919 (2011).

M. R. Castelli, A. D. Monte, M. Quaresimin, and E. Benini, *Numerical evaluation of aerodynamic and inertial contributions to Darrieus wind turbine blade deformation,* Renewable Energy **51**, 101 (2013).

A. Rossetti and G. Pavesi, *Comparison of different numerical approaches to the study of the H-Darrieus turbines start-up,* Renewable Energy **50**, 7 (2013).

M. Burlando, A. Ricci, A. Freda, and M. P. Repetto, *Numerical and experimental methods to investigate the behaviour of vertical-axis wind turbines with stators,* Journal of Wind Engineering and Industrial Aerodynamics **144**, 125 (2015).

C. S. Ferreira, *The near wake of the VAWT 2D and 3D views of the VAWT aerodynamics*, Ph.D. thesis, Delft University of Technology (2009).

U. S. Paulsen, H. A. Madsen, K. A. Kragh, P. H. Nielsen, I. Baran, J. Hattel, E. Ritchie, K. Leban, H. Svendsen, and P. A. Berthelsen, *Deepwind-from idea to 5 mw concept,* Energy Procedia **53**, 23 (2014).

H. F. Veldkamp, *Standards and load calculations*, Tech. Rep. (Suzlon Energy Limited, 2016).

C. S. Ferreira, H. A. Madsen, M. Barone, B. Roscher, P. Deglaire, and I. Arduin, *Comparison of aerodynamic models for vertical axis wind turbines,* in *Journal of Physics: Conference Series*, Vol. 524 (2014).

B. J. Jonkman and N. Kelly, *Turbsim a stochastic, full-field, turbulence simulator primarialy for use with inflowwind/aerodyn-based simulation tools,* `https://nwtc.nrel.gov/TurbSim` (2016), [Accessed: 25-August-2016].

S. D. Downing and D. F. Socie, *Simple rainflow counting algorithms,* International Journal of Fatigue **4(1)**, 31 (1982).

Garrad Hassan and Partners Limited, *Bladed Theory Manual*, Tech. Rep. (DNV GL-Energy, 2014).

P. Brøndsted, H. Lilhot, and A. Lystrup, *Composite materials for wind turbine blades,* Annual Review of Materials Research **35**, 505 (2005).

H. J. Sutherland, *On the Fatigue Analysis of Wind Turbines*, Tech. Rep. (Sandia National Laboratories, 1999).

H. F. Veldkamp, *Chances in Wind Energy: A Probabilistic Approach to Wind Turbine Fatigue Design*, Ph.D. thesis, Delft University of Technology (2006).

P. T. Philippidis, A. V. Passipoularidis, T. T. Assimakopoulou, and A. E. Antoniou, *Fatigue Tests in the Fiber Direction of UD OB Standard Specimen*, Tech. Rep. (Optimat Blades, 2006).